

Graham, Kristoffer (2009) *The synthesis and characterisation of polymetallic transition metal complexes towards single-molecule magnets*. PhD thesis.

<http://theses.gla.ac.uk/1351/>

Copyright and moral rights for this thesis are retained by the author

A copy can be downloaded for personal non-commercial research or study, without prior permission or charge

This thesis cannot be reproduced or quoted extensively from without first obtaining permission in writing from the Author

The content must not be changed in any way or sold commercially in any format or medium without the formal permission of the Author

When referring to this work, full bibliographic details including the author, title, awarding institution and date of the thesis must be given

**The Synthesis and
Characterisation of Polymetallic
Transition Metal Complexes
towards Single-Molecule Magnets**

by

Kristoffer Graham

Submitted to the University of Glasgow

for the degree of Doctor of Philosophy

in the faculty of science

Abstract

The synthesis and characterisation of sixteen new complexes are reported. The use of the ligand edte ($((\text{HOCH}_2\text{CH}_2)_2\text{NCH}_2\text{CH}_2\text{N}(\text{CH}_2\text{CH}_2\text{OH})_2)$), H_4L^1) has resulted in five new iron complexes. Two Fe_6 complexes and an Fe_3 complex display non-zero ground states of $S = 5$ and $S = 3$ respectively. An Fe_{12} complex which displays a unique cluster topology and an Fe_2 dimer are also reported, both with a ground state $S = 0$.

A further six new iron clusters are reported using bicine ($((\text{HOCH}_2\text{CH}_2)_2\text{N}(\text{CH}_2\text{COOH}))$), H_3L^2). Two homeo-structural Fe_6 complexes display spin ground states of $S = 5$ and $S = 4$, whereas a mixed-valence Fe_6 cluster has a ground state of $S = 3$ and a large magnetic anisotropy. Further measurements are needed below 1.8 K to confirm any SMM behaviour. In addition an Fe_{12} cluster with a unique core topology possesses a spin ground state of $S = 0$. Two remaining Fe_6 clusters are still to be magnetically characterised.

The final three iron complexes are reported using the ligand tricine ($((\text{HOCH}_2)_3\text{CNHCH}_2\text{COOH})$), H_4L^3). Fe_9 possesses a ground state $S = 11/2$. Magnetic characterisation of Fe_7 and Fe_{12} complexes are still needed to determine the spin ground state of these clusters.

Two new Cr(III) clusters are reported using bis-tris ($((\text{HOCH}_2)_3\text{CN}(\text{CH}_2\text{CH}_2\text{OH})_2)$), H_4L^4), the first a simple monomer and the second a Cr_4 tetramer characterised with a spin ground state $S = 0$.

Abstract	
Acknowledgements	
Author's Declaration	1
Definitions	2
1. Introduction	4
1.1 Molecular Magnetism	4
1.2 Diamagnetism	4
1.3 Paramagnetism, Van Vleck, Curie and Weiss	5
1.4 Exchange Pathways in Polymetallic Complexes	6
1.5 Single Molecule Magnets	8
1.6 Ac Susceptibility	10
1.7 Quantum Tunnelling	11
1.8 Synthetic Routes to SMMs Rational Design/Serendipitous Assembly	14
1.9 Solvothermal Synthesis	16
1.10 Microwave Synthesis	17
1.11 Applications of SMMs	18
1.12 Ligands	19
1.13 Previous uses of Ligands	19
1.14 Experimental Techniques	21
1.14.1 Infrared Spectroscopy	21
1.14.2 Single Crystal X-ray diffraction	23
1.14.3 Superconducting Quantum Interference Device (SQUID) Magnetometer	24
1.15 References	27
2.0 Synthesis of Iron complexes: edte	30
2.1 Synthesis of oxo-centred Starting materials	32
2.1.1 Synthesis of $[\text{Fe}_3\text{O}(\text{piv})_6(\text{H}_2\text{O})_3][\text{piv}][\text{Hpiv}] \cdot \text{EtOH} \cdot 2\text{H}_2\text{O}$	32
2.1.2 Synthesis of $[\text{Fe}_3\text{O}(\text{OAc})_6(\text{H}_2\text{O})_3][\text{Cl}] \cdot \text{H}_2\text{O}$	32
2.1.3 Synthesis of $[\text{Fe}_2^{\text{III}}\text{Fe}^{\text{II}}\text{O}(\text{OAc})_6(\text{H}_2\text{O})_3]$	33
2.1.4 Synthesis of $[\text{Fe}_3\text{O}(\text{OAc})_6(\text{H}_2\text{O})_3]\text{NO}_3$	33
2.1.5 Synthesis of $[\text{Fe}_3\text{O}(\text{phbenz})_6(\text{MeOH})_3](\text{NO}_3) \cdot 3\text{MeOH}$	33
2.1.6 Synthesis of $[\text{Fe}_2^{\text{III}}\text{Fe}^{\text{II}}\text{O}(\text{OBz})_6(\text{H}_2\text{O})_2(\text{MeCN})]$	34

2.2	Synthesis of complexes containing edte	34
2.2.1	Synthesis of $[\text{Fe}_{12}\text{O}_4(\text{OH})_2(\text{L}^1)_4(\text{OAc})_8][\text{Cl}]_2 \cdot 2\text{H}_2\text{O}$ (1 ·2H ₂ O)	34
2.2.2	Synthesis of $[\text{Fe}_6\text{O}_2(\text{HL}^1)_2(\text{phbenz})_8] \cdot \text{MeCN}$ (2 ·MeCN)	34
2.2.3	Synthesis of $[\text{Fe}_6\text{O}_2(\text{HL}^1)_2(\text{piv})_8] \cdot \text{MeCN}$ (3 ·MeCN)	35
2.2.4	Synthesis of $[\text{Fe}^{\text{III}}\text{Fe}^{\text{II}}_2(\text{OBz})_2(\text{H}_2\text{L}^1)_2][\text{OBz}] \cdot \text{MeCN}$ (4 ·MeCN)	35
2.2.5	Synthesis of $[\text{Fe}_2(\text{H}_2\text{L}^1)_2]$ (5)	35
2.3	Complexes containing edte	36
2.3.1	Discussion of the Crystal Structure of (1 ·2H ₂ O)	36
2.3.1.1	Magnetic Susceptibility measurements for 1 ·2H ₂ O	41
2.3.2	Discussion of the Crystal Structure of (2 ·MeCN)	42
2.3.2.1	Magnetic Susceptibility measurements for 2 ·MeCN	47
2.3.3	Discussion of the Crystal Structure of (3 ·MeCN)	48
2.3.3.1	Magnetic Susceptibility measurements for 3 ·MeCN	51
2.3.4	Discussion of the Crystal Structure of (4 ·MeCN)	54
2.3.4.1	Magnetic Susceptibility Measurements of 4 ·MeCN	58
2.3.5	Discussion of the Crystal Structure of (5 ·MeCN)	60
2.3.5.1	Magnetic Susceptibility Measurements of 5 ·MeCN	64
2.4	Conclusions	65
2.5	Future work	66
2.6	References	67
3.0	Synthesis of iron complexes: Bicine	70
3.1	Synthesis of complexes containing Bicine	71
3.1.1	Synthesis of $[\text{Et}_2\text{NH}_2]_2[\text{Fe}_6\text{O}_2(\text{OH})_2(\text{L}^2)_2(\text{piv})_8] \cdot 2\text{MeCN}$ (6 ·2MeCN)	71
3.1.2	Synthesis of $[\text{Fe}_6\text{O}_2(\text{OMe})_2(\text{L}^2)_2(\text{phbenz})_4(\text{MeOH})_6][\text{NO}_3]_2 \cdot \text{MeOH}$ (7 ·MeOH)	71
3.1.3	Synthesis of $[\text{Et}_2\text{NH}_2]_2[\text{Fe}_6\text{O}_2(\text{OH})_2(\text{L}^2)_2(\text{OAc})_8]$ (8)	71
3.1.4	Synthesis of $[\text{Fe}_{12}\text{O}_4(\text{L}^2)_4(\text{H}_1\text{L}^2)_4(\text{piv})_8] \cdot 5\text{MeCN}$ (9 ·5MeCN)	72
3.1.5	Synthesis of $[\text{Fe}_2^{\text{III}}\text{Fe}_4^{\text{II}}\text{O}_2(\text{benz})_{10}(\text{MeCN})_4]$ (10)	72

3.1.6	Synthesis of $[\text{Et}_2\text{NH}_2][\text{Et}_2\text{NH}][\text{Fe}_6\text{O}_2(\text{OAc})_{15}(\text{HOAc})_2] \cdot 2\text{MeCN}$ (11 ·2MeCN)	72
3.2	Complexes containing Bicine	73
3.2.1	Discussion of the Crystal Structure of (6 ·2MeCN)	73
3.2.1.1	Magnetic Susceptibility measurements for 6 ·2MeCN	76
3.2.2	Discussion of the Crystal Structure of (7 ·MeOH)	79
3.2.2.1	Magnetic Susceptibility measurements for 7 ·MeOH	82
3.2.3	Discussion of the Crystal Structure of (8)	85
3.2.4	Discussion of the Crystal Structure of (9 ·5MeCN)	88
3.2.4.1	Magnetic Susceptibility Measurements for 9 ·5MeCN	92
3.2.5	Discussion of the Crystal Structure of (10)	93
3.2.5.1	Magnetic Susceptibility Measurements for (10)	98
3.2.6	Discussion of the Crystal Structure of (11)	102
3.3	Conclusions	106
3.4	Future work	106
3.5	References	108
4.0	Synthesis of iron complexes: Tricine	109
4.1	Synthesis of complexes containing Tricine	111
4.1.1	Synthesis of $\text{DEAH}[\text{Fe}_9\text{O}_4(\text{OH})_2(\text{HL}^3)_2(\text{phbenz})_{12}] \cdot 5\text{MeCN} \cdot \text{H}_2\text{O}$ (12 ·5MeCN·H ₂ O)	111
4.1.2	Synthesis of $\text{Na}_3[\text{Fe}_7\text{O}_4(\text{OH})(\text{H}_3\text{L}^3)_2(\text{phbenz})_{11}] \cdot 4\text{H}_2\text{O}$ (13 ·4H ₂ O)	111
4.1.3	Synthesis of $\text{Na}[\text{Fe}_{11}\text{O}_6(\text{OH})_6(\text{phbenz})_{15}(\text{OMe})]$ (14)	112
4.2	Complexes containing Tricine	112
4.2.1	Discussion of the Crystal Structure of (12 ·5MeCN·H ₂ O)	112
4.2.1.1	Magnetic Susceptibility measurements for 12 ·5MeCN·H ₂ O	118
4.2.2	Discussion of the Crystal Structure of (13 ·4H ₂ O)	121
4.2.3	Discussion of the Crystal Structure of (14)	128

Kristoffer Graham	Contents	2009
4.3	Conclusions	133
4.4	Future work	134
4.5	References	135
5.0	Synthesis of Chromium Complexes: Bis-Tris	136
5.1	Synthesis of complexes containing Bis-Tris	137
5.1.1	Synthesis of $[\text{Cr}(\text{H}_3\text{L}^4)\text{Cl}]$ (15)	137
5.1.2	Synthesis of $[\text{Cr}_4(\text{H}_2\text{L}^4)_4]\cdot\text{MeOH}$ (16 ·MeOH)	138
5.2	Complexes containing Bis-Tris	138
5.2.1	Discussion of the Crystal Structure of (15)	138
5.2.2	Discussion of the Crystal Structure of (16 ·MeOH)	140
5.2.2.1	Magnetic Susceptibility measurements for (16 ·MeOH)	144
5.3	Conclusions	146
5.4	Future work	146
5.5	References	148
6.0	Conclusions	149
6.1	The EDTE ligand	149
6.2	The Bicine ligand	150
6.3	The Tricine ligand	152
6.4	The Bis-Tris ligand	153

Acknowledgements

I would like to take the opportunity to thank my supervisor Mark Murrie. Not only for giving me the opportunity to be part of his research group but for his guidance and support throughout my PhD which has made this experience rewarding and enjoyable. I would also like to thank my second supervisor Dan Price, for giving me constructive feedback on my research.

To Alan Ferguson, who's guidance in the lab and input into my research helped me greatly (together with xFm radio which played good music), thank you.

Thank you to my project student Amiera Darwish, your hard work played an important part in this thesis and your fun personality together with your singing made the lab an enjoyable place to work.

I would also like to thank the other members of the Murrie group Kyle, Pascal and Marta who have been with me throughout my PhD sharing in my experiences.

I would like to thank past PhD students, such as Gemma Parker, Dave Eustace, David McKay and Katrina Davidson who have provided great entertainment throughout my time here.

The department's technical staff is thanked for their excellent service.

Thank you to Simon Parsons, Marc Schmidtman and the late Andy Parkin for their help with crystallography problems encountered in this thesis and Javier Sanchez-Benitez for his magnetic measurements when our SQUID was down.

I would like to thank my own personal friends John Sturdy and Kevan Todd for their banter and wacky antics which have kept me going throughout my university career. Finally to Stephanie Thom who has kept me focused over the past few months and supported me when times were tough, thanks cheeky.

Author's Declaration

The work contained in this thesis, submitted for the degree of doctor of philosophy, is my own original work, except where due reference is made to others. No material within has been previously submitted for a degree at this or any other university.

Definitions

SMM	=	Single molecule magnet
OAc	=	Acetate
Piv	=	Pivalate
Phbenz	=	2-Phenoxybenzoic acid
OBz	=	Benzoate
Tacn	=	1, 4, 7-triazacyclononane
Sao	=	Salicylaldehyde
PhCH ₂ OH	=	Benzyl alcohol
^t BuCH ₂ COOH	=	tert-Butylacetic acid
Tris	=	2-amino-2-(hydroxymethyl)propane-1,3-diol
Bis-Tris	=	2-[bis(2-hydroxyethyl)amino]-2 (hydroxymethyl)propane-1,3-diol
EDTE	=	N, N, N',N'-Tetrakis(2hydroxyethyl) Ethylenediamine
EDTA	=	Ethylenedinitrilotetraacetic acid
Bicine	=	N,N-bis(2-hydroxyethyl)glycine, di(hydroxyethyl) glycine
Bic	=	Bicine
Tricine	=	N-(2-hydroxy-1,1bis(hydroxymethyl)ethyl) glycine
SQUID	=	Superconducting Quantum Interference Device
BVS	=	Bond Valence Sum
HF-EPR	=	High Frequency Electron Paramagnetic Resonance
Magnevist	=	Gadopentetic acid
Thme	=	tris(hydroxymethyl)ethane
Dmp	=	dipivaloylmethane
Bta	=	benzotriazole
Methedi	=	N-(1-Hydroxymethylethyl)iminodiacetic acid

For Mum, Dad and Josh

Thank you.

1.0 Introduction

1.1 Molecular magnetism

The magnetisation M , of a sample placed in a homogeneous magnetic field H , is related through equation 1.1 where χ is the magnetic susceptibility.¹ When the field is weak enough, χ is independent of H which leads to equation 1.2.

$$\chi = dM/dH \quad (1.1)$$

$$\chi = M/H \quad (1.2)$$

Magnetic susceptibility is composed of two contributions; diamagnetic and paramagnetic susceptibility (equation 1.3).¹

$$\chi = \chi^D + \chi^P \quad (1.3)$$

Where χ^D and χ^P are the diamagnetic and paramagnetic susceptibilities respectively. The diamagnetic contribution (χ^D) of a sample can be roughly estimated (equation 1.4), where k is a factor varying between 0.4 and 0.5 and Mw is the molecular weight.¹

$$\chi^D = kMw \times 10^{-6} \text{ cm}^3 \text{ mol}^{-1} \quad (1.4)$$

1.2 Diamagnetism

Diamagnetism arises from the interaction of paired electrons with a magnetic field.² All materials possess diamagnetic character, even when it is masked by paramagnetism.¹ A diamagnetic sample placed in a magnetic field will align itself against the applied field meaning magnetic susceptibility will be negative.³

1.3 Paramagnetism, Van Vleck, Curie and Weiss

Paramagnetism is the result of interactions of orbital and/or spin angular momentum of unpaired electrons with the applied field.² In molecular magnetism one of the fundamental equations (1.5), can be used to deduce molar magnetic susceptibility.

$$M = \frac{N \sum_n \frac{-dE_n}{dH} \exp(-E_n/kT)}{\exp(-E_n/kT)} \quad (1.5)$$

Where N is Avogadro's number, T is absolute temperature, k is the Boltzman constant. Although this equation relies on no approximations, it is often difficult to apply.

Van Vleck derived an equation to calculate magnetic susceptibilities of paramagnetic systems based on a few approximations.¹ Through expanding the energies of states and assuming that both H is not too large and T too small, he derived the Van Vleck formula (equation 1.6).

$$\chi = \frac{N \sum_n [(E_n^{(1)})^2 / kT - 2E_n^{(2)}] \exp(-E_n^{(0)} / kT)}{\sum_n \exp(-E_n^{(0)} / kT)} \quad (1.6)$$

This equation can be simplified further to give equation 1.7 known as the Curie law.

$$\chi = \frac{Ng^2 \mu_B^2}{3kT} S(S+1) \quad \text{or} \quad \chi = \frac{C}{T} \quad (1.7)$$

Curie law

Where N is Avogadro's number, β is the bohr magneton, g is a constant and S is the spin ground state. The Curie law holds true for normal paramagnets and the sample shows a horizontal straight line in a plot of χT vs T.

However, it was found that not all paramagnets obey the Curie law. It was shown that some material's susceptibilities could be fitted to equation 1.8 known as the Curie-Weiss law (equation 1.8).

$$\chi = \frac{C}{T - \theta} \quad (1.8)$$

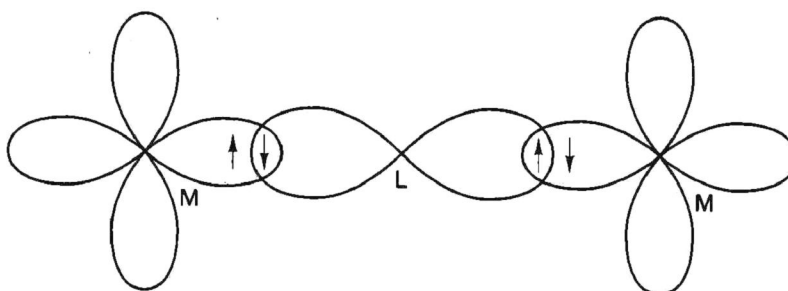
Curie-Weiss law

Where θ is the Weiss constant. This constant is positive for ferromagnetically ordered material and negative for antiferromagnetically ordered materials.

1.4 Exchange pathways in polymetallic complexes

Direct exchange involves direct overlap of orbitals containing unpaired electrons,² resulting in an interaction without the need for an intermediate diamagnetic bridging ion. This type of interaction was first observed by Figgis and Martin⁴ for a sample of $[\text{Cu}_2(\text{OAc})_4(\text{H}_2\text{O})_2]$ where one unpaired electron in each of the $d_{x^2-y^2}$ orbital of the Cu(II) centre interact.

Superexchange is an exchange interaction between neighbouring metal centres which proceeds through a diamagnetic ion. This type of exchange depends upon the degree of orbital overlap therefore the M-L-M (where M is the metal and L is the ligand) bond angle is very important. For linear interactions, the electrons align antiparallel resulting in an antiferromagnetic interaction. Interactions where the angle is close to 90° , results in unpaired electrons aligning parallel promoting ferromagnetic coupling between the two metal centres (figure 1.1).



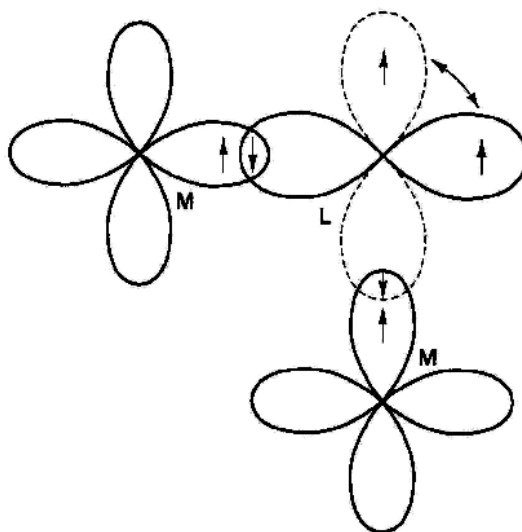


Figure 1.1: Illustration of antiferromagnetic exchange (top) and ferromagnetic exchange (bottom) between two metal centres⁵

Superexchange can also proceed between two different metal centres. The exchange is stabilised by unpaired electrons in the orthogonal orbitals, which tend to align with parallel spins (figure 1.2).

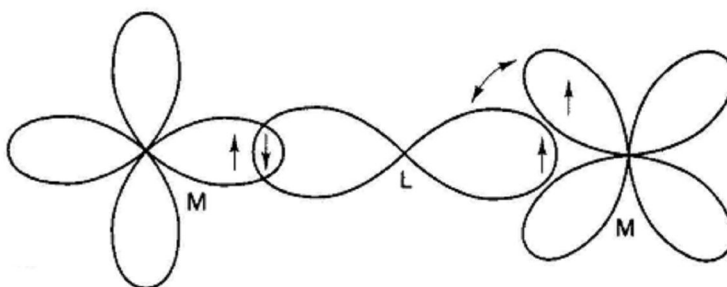


Figure 1.2: Illustration of ferromagnetic exchange between two different metal centres⁵

This spin-spin interaction can be represented by the spin Hamiltonian given in equation 1.9 where J_{ij} is the exchange integral.

$$\hat{H} = -2\sum J_{ij}\hat{S}_i\cdot\hat{S}_j \quad (1.9)$$

For binuclear complexes the Hamiltonian is given as equation 1.10.

$$\hat{H} = -2J\hat{S}_1 \cdot \hat{S}_2 \quad (1.10)$$

For antiferromagnetic interactions, J will be negative; a ferromagnetic interaction will give a positive J .

1.5 Single Molecule Magnets

A single molecule magnet, SMM, displays superparamagnetic-like properties below a certain temperature known as its blocking temperature.⁶ These properties are solely molecular as SMMs are surrounded by an organic shell, and are not due to the long range ordering associated with bulk magnets. $[\text{Mn}_{12}\text{O}_{12}(\text{CH}_3\text{O}_2)_{16}(\text{H}_2\text{O})_4] \cdot 2\text{CH}_3\text{O}_2\text{H} \cdot 4\text{H}_2\text{O}$, $(\text{Mn}_{12}\text{OAc})^7$ was the first complex to display single SMM behaviour.⁸ One of the features of Mn_{12}OAc is its slow relaxation of magnetisation, which has attracted major interest.⁹ This gives rise to hysteresis loops more commonly observed in bulk magnets. Slow relaxation of magnetisation is a result of a negative axial zero-field splitting, D , which leads to the splitting of the spin ground state (S) (figure 1.3).¹⁰

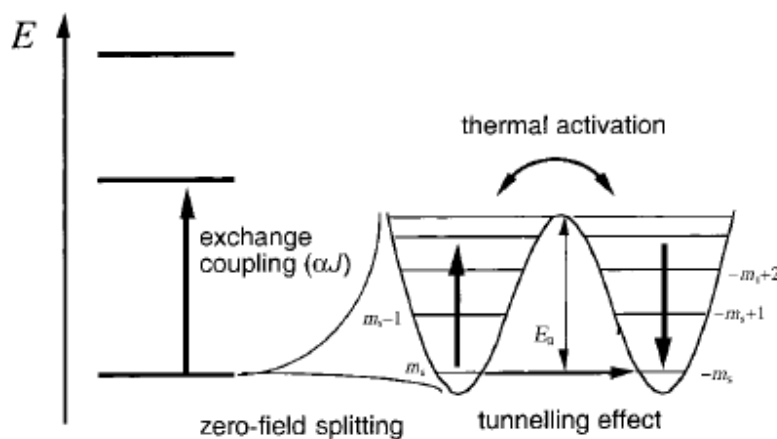


Figure 1.3: Representation of zero-field splitting within the ground state leading to an energy barrier E_a ¹⁰

The energy barrier associated with reorientation of the spin is given by equation 1.11 for an integer spin and 1.12 for a non-integer spin.

$$E_a = S^2 |D| \quad (1.11)$$

$$E_a = (S^2 - \frac{1}{4}) |D| \quad (1.12)$$

The larger the value of S , together with a large negative zero-field splitting parameter, the larger the barrier of reorientation. For Mn_{12}OAc an $S = 10$ ground state and a negative D value results in splitting of the ground state into 21 m_s levels with an energy barrier of 60 K. The large energy barrier allows the molecule to be magnetised in one direction in the presence of a magnetic field. When the field is applied in one direction, the magnetisation of the sample will reach its maximum meaning only the $m_s = -10$ will be populated. Once the field is removed, the sample slowly returns to its equilibrium of zero, dependant upon the size of the energy barrier and whether the sample is below its blocking temperature. Above the blocking temperature the relaxation of magnetisation is 50% $m_s +10$ and 50% $m_s -10$, below the blocking temperature the magnetisation is blocked in $m_s = -10$. Below the blocking temperature, the field can then be applied in the opposite direction allowing the sample to be either spin up or spin down in the zero field depending on the sign of the applied field. This can lead to sweep dependent hysteresis loops in magnetisation versus field studies shown for $[\text{Mn}_{12}\text{O}_{12}(\text{O}_2\text{CCH}_2\text{Br})_{16}(\text{H}_2\text{O})_4]$ in figure 1.4.¹¹

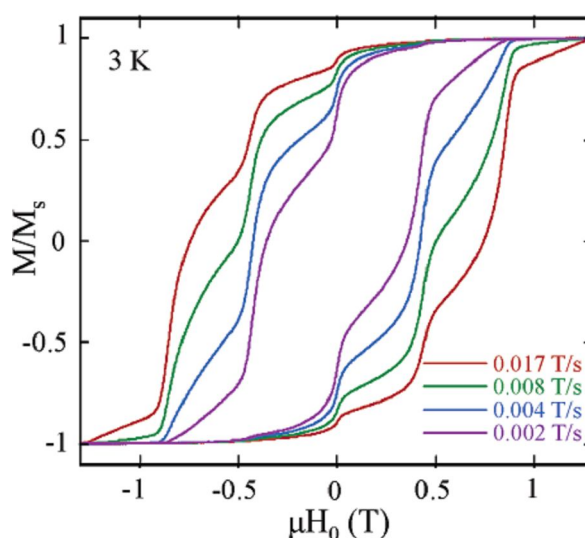


Figure 1.4: $[\text{Mn}_{12}\text{O}_{12}(\text{O}_2\text{CCH}_2\text{Br})_{16}(\text{H}_2\text{O})_4]$ sweep dependent hysteresis loops¹¹

1.6 Ac Susceptibility

Ac susceptibility measurements can provide further evidence of slow magnetic relaxation. By applying an oscillating magnetic field, it is possible to measure the dynamic susceptibility. At high frequency, the magnetization of the sample may not be able to follow the immediate changes caused by the oscillating field, which leads to a non-zero response in χ'' . The dynamic susceptibility is composed of two quantities: χ' , the magnetic susceptibility and φ , the phase shift.¹² From this the dynamic susceptibility $\chi(\omega)$ can be thought of as a complex quantity (equation 1.13),

$$\chi(\omega) = \chi'(\omega) - i\chi''(\omega) \quad (1.13)$$

where $\omega = 2\pi\nu$ is the angular frequency, $\chi' = \chi \cos \varphi$ and $\chi'' = \chi \sin \varphi$ are the real and imaginary components which are both frequency dependent. At low frequency χ' will follow the low field static susceptibility, however if slow magnetic relaxation is present an increase in χ'' should be observed over all frequencies. This increase can be seen as distinct peaks in SMMs, which occurs due to the relaxation rate becoming comparable with the frequency producing a maximum in χ'' . At this maximum $\omega = \tau^{-1}$, this allows us to calculate the relaxation time. For SMMs the relaxation time follows an Arrhenius law of thermal activation over the energy barrier given as equation 1.14.

$$\tau = \tau_0 e^{E_a / kT} \quad (1.14)$$

By measuring different frequencies and noting the temperature of the maximum in χ'' , the E_a barrier can be calculated. An example of an Arrhenius plot of τ vs. $1/T$ for $[\text{Mn}_{12}\text{O}_{12}(\text{O}_2\text{CCH}_2\text{Br})_{16}(\text{H}_2\text{O})_4] \cdot 4\text{CH}_2\text{Cl}_2$ is given below (figure 1.5), the Arrhenius equation can then be fitted to find values for E_a and τ_0 (where τ_0 is the attempted frequency).

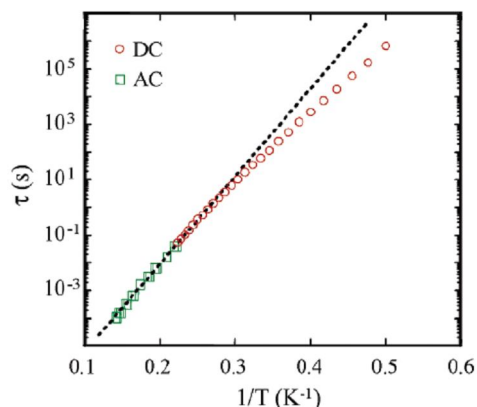


Figure 1.5: Plot of relaxation time (τ) vs. $1/T$ for $[\text{Mn}_{12}\text{O}_{12}(\text{O}_2\text{CCH}_2\text{Br})_{16}(\text{H}_2\text{O})_4] \cdot 4\text{CH}_2\text{Cl}_2$ using AC and DC magnetization data¹¹

1.7 Quantum Tunnelling

Quantum tunnelling of magnetization, (QTM) is another phenomenon associated with SMMs. The origin of QTM is still a matter of active research. This process of tunnelling occurs between two levels that have the same energy if some admixing of the two states occur,⁶ which in turn increases the relaxation rate. An example of QTM is shown in figure 1.6.

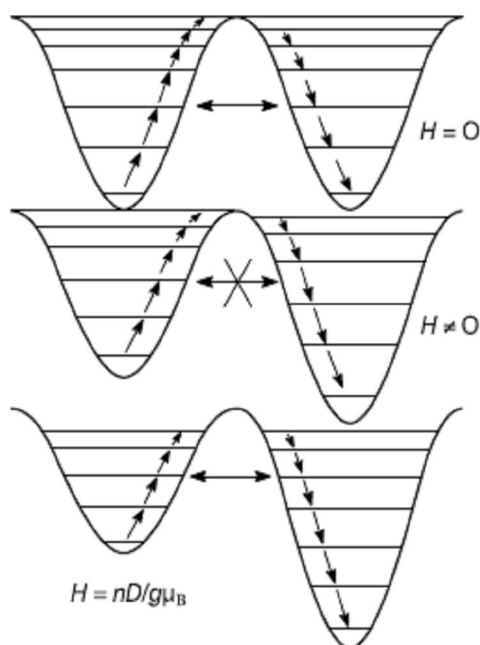


Figure 1.6: The potential energy diagram of an SMM showing changes as the field is swept from $H_z = 0$ to $H_z = nD/g\mu_B$ ⁶

QTM is said to occur due to dipolar interactions,¹³ nuclear spins¹⁴ and phonon assisted tunnelling.¹⁵ The original SMM, Mn₁₂OAc and its derivatives¹⁶ have become the most studied SMMs in a bid to understand this phenomenon. In SMMs which have S₄ symmetry the zero field Hamiltonian can be expressed as equation 1.15.

$$\mathbf{H} = \underset{(1)}{D} \mathbf{S}_z^2 + \underset{(2)}{g_{z\mu B}} \mathbf{H}_z \mathbf{S}_z + \underset{(3)}{E} (\mathbf{S}_x^2 - \mathbf{S}_y^2) + \underset{(4)}{B/2} (\mathbf{S}_+^4 + \mathbf{S}_-^4) \quad (1.15)^{17}$$

Terms (1) and (2) are the uniaxial anisotropy and the Zeeman interaction of the magnetic field along the z axis. The second order E term, (3) allows the transition between states when the eigenvalues of S_z differ by a value of multiples of two and (4) is the symmetry allowed term for fourth order symmetry which permits tunnelling every fourth step.¹⁷

For tetragonal symmetry, the second order E term should vanish, meaning QTM should only come from the fourth order term; however it was shown experimentally that all transitions between states occur.¹⁷ These transitions disobey the rules for tetragonal symmetry making it necessary to include a higher order term which arises from crystals having lower symmetry groups. Detailed X-ray analysis^{17,18} showed that not all Mn₁₂OAc molecules display S₄ symmetry due to disorder of the acetic acid molecules over two sites around the two fold axis. Also, evidence of dislocations in the crystal which lead to disorder of the crystal structure has been presented,¹⁹ however extensive work has been done to support the findings of Cornia *et al.*²⁰ High-field EPR has been used to determine values of the second order E term.²⁰ Synthesis of Mn₁₂ derivatives with pure S₄ symmetry have been studied by Barra *et al.*,¹⁶ indicating the presence of sixth order terms of magnetic anisotropy. The fourth order transverse anisotropy is directly connected to the tilting of the single-ion easy axis.¹⁶ and the sixth order term shows more complex behaviour.¹⁶ The work goes on to describe how subtle alterations in tilting the angle produce a significant increase in the tunnel splitting making it possible to predict based on design the magnetic anisotropy of SMMs to higher orders.¹⁶

The complex $[\text{Fe}_8\text{O}_2(\text{OH})_{12}(\text{tacn})_6]\text{Br}_8$,²¹ (where tacn is 1,4,7-triazacyclononane), (Fe_8) was the first iron-based complex to show SMM behaviour and is the second most studied SMM (figure 1.7).²²

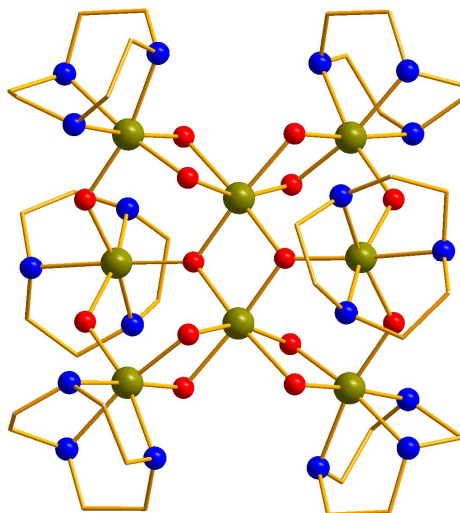


Figure 1.7: Structure of the cation $[\text{Fe}_8\text{O}_2(\text{OH})_{12}(\text{tacn})_6]^{8+}$. Ball and stick representation with Fe(III), Gold, C, Brown, N, Blue; O, Red; H and Br atoms are omitted for clarity.

Just like Mn_{12}OAc , Fe_8 has an $S = 10$ ground state, confirmed by high field magnetization measurements²³ and a D parameter of -0.19 cm^{-1} , the m_s levels are largely split in zero field.²⁴ The low lying m_s levels resemble that of Mn_{12}OAc while approaching the top of the barrier labelling of the m_s states is no longer appropriate due to strong admixing from a large transverse anisotropy, $E = 0.046 \text{ K}$. Hence, it is not possible to calculate an energy barrier (equation 1.11) between the lowest and highest energy levels. Fe_8 also shows steps in hysteresis loops,²⁵ which are attributed to thermally activated tunnelling. The hysteresis of Fe_8 shows a strong dependence on sweep rate of the field. The lower the sweep rate, the smaller the fraction of molecules that can relax by quantum tunnelling at the lower fields. Steps at higher fields increase in height as the sweep rate increases. For Fe_8 , the hysteresis becomes temperature independent below 350mK making it more suitable to explore the effects related to the quantum tunnelling process.

The interesting properties found for Fe_8 prompted further investigation into polynuclear iron(III) clusters displaying SMM behaviour. $[\text{Fe}_4(\text{OMe})_6(\text{dpm})_6]$, (Fe_4)

provided insights into the ZFS in Iron(III) complexes.²⁶ The small number of Fe(III) ions made it possible for detailed calculations to be performed on the energy and spin levels. The single ion and spin-spin contributions to the total D parameter of the cluster were established. This has helped to rationalise the enhanced anisotropy of the analogous complex $[\text{Fe}_4(\text{thme})_2\text{dpm}]_6$.²⁷ These breakthroughs have promoted further interest in the synthesis of polynuclear iron complexes that function as SMMs.²⁸ Further examples of iron(III) SMMs will be discussed/highlighted in later chapters.

1.8 Synthetic Routes to SMMs Rational / Serendipitous

The synthesis of SMMs via rational design is difficult. Rational design involves the synthesis of ligands, that can be reacted to control and produce predicted structural motifs. Examples where this has been successful are provided by Thompson *et al.*²⁹ The use of rigid ligands based on a diazine backbone stabilized the chelating metal ions to produce a nonanuclear Mn_9 grid. Another example includes the use of hexacyanometalates precursors with rigid ligands. Marvaud *et al.*,¹⁰ showed how this approach produced a series of predictable structures, highlighting how they could control the spin ground state of clusters, using the CN^- bridging ligands which ensure strong magnetic interaction between the metal centres to produce clusters with ground states up to $S = 27/2$. Another example of the use of CN^- bridging ligands is $[\text{Mn}^{\text{II}}\{\text{Mn}^{\text{II}}_8(\text{MeOH})_3\}_8(\mu\text{-CN})_{30}\{\text{Mo}^{\text{V}}(\text{CN})_3\}_6] \cdot 5\text{MeOH} \cdot 2\text{H}_2\text{O}$, (Mn_9Mo_6) with $S = 39/2$.³⁰ However none of the above have shown SMM behaviour.

There are examples of SMMs produced via rational design by Glaser *et al.*³¹ The design of a complex ligand to promote ferromagnetic exchange, led to a Mn_6Cr complex with $S = 21/2$ which displayed hysteresis below 1.5K. Also Kim *et al.*,³² report the use of CN^- bridging for the complex $[(\text{Tp})_8\text{Fe}_4\text{Ni}_4(\text{CN})_{12}]$ which displays SMM behaviour.

Another area of rational design involves the substitution of ligands of known complexes. The previously mentioned $[\text{Fe}_4(\text{OMe})_6(\text{dpm})_6]$,²⁸ being a prime example, using site specific ligand substitution of the six methoxide bridges, results in much

larger anisotropy and a higher barrier to reorientation.³³ In 2007 Milios *et al*³⁴ reported the structural distortion of a previously studied complex $[\text{Mn}_6\text{O}_2(\text{sao})_6(\text{O}_2\text{CPh})_2(\text{EtOH})_4]$, ($\text{saoH}_2 = 2\text{-hydroxybenzaldehyde oxime}$). Changing the saoH_2 ligand for 2-hydroxyphenylpropanone oxime (Et-saoH_2) and benzoate for 3, 5-dimethylbenzoate resulted in the complex $[\text{Mn}_6\text{O}_2(\text{Etsao})_6(\text{O}_2\text{CPh}(\text{Me})_2)_2(\text{EtOH})_6]$ which holds the record for the largest effective energy barrier seen for an SMM to date.³⁴ A series of Mn_{12}OAc derivatives have also been prepared^{11,35} via ligand exchange of the original preformed cluster. The introduction of bulkier carboxylate groups such as PhCO_2H and $^t\text{BuCH}_2\text{CO}_2\text{H}$ has allowed larger separation of clusters minimising interactions between clusters. Also these modified clusters have eliminated the problem of disordered solvent and Jahn-Teller isomers, seen in Mn_{12}OAc improving the quality of the magnetic data. This has resulted in greater understanding the properties of the Mn_{12}OAc core and the subsequent effects of ligand substitution on the magnetic properties.²⁸

Rational design has provided valuable knowledge and understanding of current SMMs. It has produced a new SMM with the highest effective energy barrier and currently the best example of an SMM, making the approach of tailoring known complexes more appealing than serendipitous self assembly which is more widely used.

Serendipitous self assembly is a more favoured synthetic route for chemists. It is more unpredictable, being influenced by the choice of the ligand employed. Generally, polydentate ligands are used due to their multiple coordination sites along with metal salts where the metal centres are capable of different coordination geometries. Reactions can also be in the presence of base to control the deprotonation of the ligand. One of the most common ligand types used are carboxylate ligands which through deprotonation can bind to either one metal centre or act as a bridge between more than one centre shown (figure 1.8).

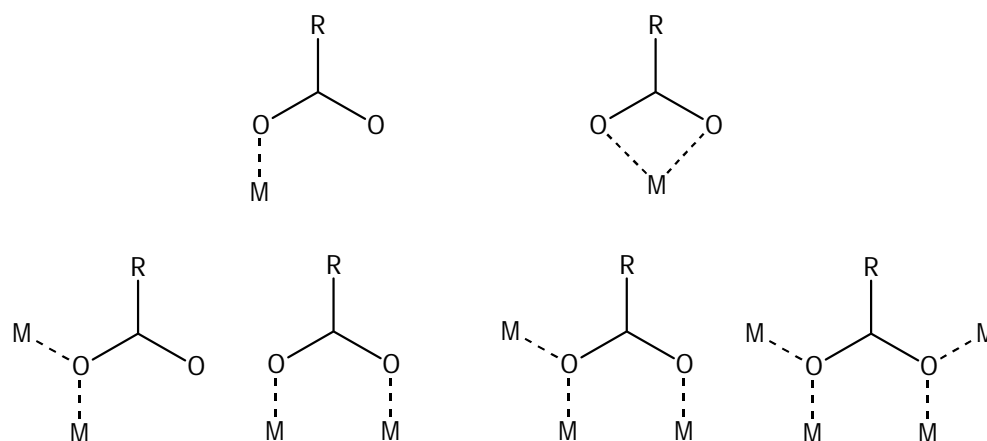


Figure 1.8: Coordination and bridging modes of the carboxylate ligand³⁶

Carboxylates are widely used because their R groups can be easily varied to alter structural properties like solubility and steric hindrance amongst others. These ligands are generally found in structures as a 1,3 bridging ligand in the presence of another co-ligand, which is a successful technique in the synthesis of large poly-metallic complexes. Carboxylates can also be incorporated into pre-formed building blocks or oxo-centred triangles and reacted with other polydentate ligands which usually results in disruption of the building block core to produce larger clusters of transition metal complexes. This technique has been used to great effect with some exceptionally large clusters being formed such as $[\text{Mn}_{84}\text{O}_{72}(\text{OAc})_{78}(\text{OMe})_{24}(\text{OH})_6(\text{MeOH})_{12}(\text{H}_2\text{O})_{42}]$.³⁷ The use of these pre-formed building blocks will be discussed further in other chapters.

1.9 Solvothermal Synthesis

Most clusters are synthesised through the methods described above, at ambient temperature and under atmospheric pressure in low boiling point solvents. Solvothermal techniques involve heating a reaction mixture in a sealed vessel, allowing the reaction to proceed at high temperature and pressure. The advantages include the possibility of insoluble or unreactive reagents at room temperature to become more reactive, due to the different solubility properties of superheated solvents. Also this technique is thought to enhance crystal growth due to the

reduced viscosity of the solvent at high temperature.³⁸ The products formed by the solvothermal approach tend to lead to the thermodynamic and not the kinetic products formed at room temperature.

The solvothermal synthesis of polymetallic species stems from work by Zubieta and co-workers on the synthesis of high valent polyoxovanadates and molybdates.³⁹ Laye and co-workers superheated solutions of the trimetallic complex $[\text{Cr}_3\text{O}(\text{O}_2\text{CMe})_6(\text{H}_2\text{O})_3]\text{Cl}$ in MeOH and EtOH solutions yielding $[\text{Cr}_{10}(\text{OR})_{20}(\text{O}_2\text{CMe})_{10}]$ (where R is Me or Et) to overcome the kinetic inertness of Cr(III) ions. Also, this same process was employed in the synthesis of $[\text{Fe}_{14}(\text{bta})_6\text{O}_6(\text{OMe})_{18}\text{Cl}_6]$, $(\text{Fe}_{14}\text{bta})^{40}$ from a superheated reaction of $[\text{Fe}_3\text{O}(\text{O}_2\text{CMe})_6(\text{H}_2\text{O})_3]\text{Cl}$ in MeOH with benzotriazole (btaH). At room temperature no clean product could be obtained however solvothermally the product was obtained in good yield. This was extended further when the analogous complex $[\text{Cr}_{14}\text{O}_6(\text{bta})_6(\text{OMe})_{18}\text{Cl}_6]$, (Cr_{14}) , was obtained solvothermally from CrCl_3 . Cr_{14} possesses an $S = 0$ ground state unlike the $S = 25$ ground state seen for Fe_{14}bta .⁴¹ The above examples illustrate some advantages of solvothermal over conventional synthesis of polymetallic clusters with interesting magnetic properties.

1.10 Microwave Heating

This technique has been employed in various chemical syntheses such as analytical chemistry and liquid-phase organic synthesis,⁴² however it is now being explored in the synthesis of SMMs. In 2006, the first new manganese complex $[\text{Mn}^{\text{III}}_6\text{O}_2(\text{sao})_6(\text{O}_2\text{CH})_2(\text{CH}_3\text{OH})_4]$, synthesised by microwave heating, was reported by Brechin *et al.*⁴³ The complex had been prepared both in a microwave reactor and at room temperature, however the microwave technique provided an increased yield of 80% for five minutes irradiation and one day crystallisation versus 30% for a one hour reaction and five days crystallisation at room temperature. Further examples of different metal centres include $[\text{Fe}_8\text{O}_4(\text{sao})_8(\text{py})_4]$, which could be obtained through microwave synthesis and solvothermal synthesis in lower yields.⁴⁴ There are also some examples of trimetallic cobalt and nickel complexes produced using this technique.⁴⁵ The use of microwave irradiation is relatively new and has shown its

potential to synthesis new polymetallic complexes and should become a more recognised route to SMMs in the future.

1.11 Applications of SMMs

The magnetic properties displayed by SMMs has sparked research into possible applications such as high density data storage, quantum computing,⁴⁶ magnetic resonance imaging,⁴⁷ magnetic refrigeration⁴⁸ and spintronics.⁴⁹ The possible attachment of $Mn_{12}OAc$ onto surfaces Au(111) and Si(100) surfaces has been extensively investigated. This has been achieved by simple exchange of the acetate ligands in $Mn_{12}OAc$ for thiol containing acetates and attachment due to strong Au-S bond formation.⁵⁰ Another technique involved anchoring the Mn_{12} clusters onto a functionalised silicon surface via long chain carboxylates.⁵¹ However both these techniques resulted in disordered layer of Mn_{12} molecules. A successful approach for producing an ordered layer of Mn_{12} was reported in 2005 involving Mn_{12} clusters and 4-(methylthio)benzoate ligands.⁵² The substitution of thioether groups for acetate in $Mn_{12}OAc$, and the immersion of Au(111) substrates in a THF solution of the Mn_{12} complex, results in complete surface coverage after 24 hours. Other approaches include the substitution of betaine (${}^+N(CH_3)_3CO_2^-$) into Mn_{12} molecules. This has resulted in Mn_{12} molecules being assembled onto a Au(111) surfaces using a self assembled mono layer of SO_3^- groups.⁵³

Langmuir Blodgett films of $Mn_{12}OAc$ derivatives have been synthesised and their magnetic properties measured.⁵⁴ Magnetic measurements of Mn_{12} films on Au(111) substrates have been performed.⁵⁵ More investigation is needed into these techniques and if the blocking temperature of SMMs can be raised, the potential of high density data storage could be achieved. MRI contrast agents are another area where SMM application is being investigated, in particular for Fe_8 .⁵⁶ Investigations are still on-going to determine if Fe_8 is more efficient in MRI than magnevist.⁴⁷ Magnetic refrigeration using SMMs has also been explored. Both $Mn_{12}OAc$ and Fe_8 have been studied, however neither are suitable for low temperature refrigeration due to their anisotropy and quantum effects. An excellent candidate is the ferromagnetic Mn_{10} complex which, in the early stages, has shown great potential as

a possible refrigerant.⁴⁸ Another lead candidate is the previously mentioned Fe_{14}bta complex reported show a magnetocaloric response around liquid helium temperature.⁴⁰ Finally the area of spintronics relatively new area,⁴⁹ which aims at the manipulation of spins and charges in electronic devices containing one or more molecules. SMMs are particularly attractive due to their molecular size and bulk magnetic properties resulting in slow magnetisation relaxation at low temperatures. Mn_{12} is currently investigated due to its ligand exchange chemistry and its well understood magnetic properties.

1.12 Ligands

The use of flexible organic ligands has produced some of the best SMMs to date. The research presented in this thesis focuses on a series of structurally related ligands following the success of the ligand 2-[bis(2-hydroxyethyl)amino]-2-(hydroxymethyl)propane-1,3-diol, (Bis-tris, $\text{C}_8\text{H}_{19}\text{NO}_5$).⁵⁷ A search of the Cambridge structural database highlighted a few potential candidates, N, N,N',N'-Tetrakis(2-hydroxyethyl)ethylenediamine, (EDTE, $\text{C}_{10}\text{H}_{24}\text{N}_2\text{O}_4$), N,N-bis(2-hydroxyethyl)glycine, (Bicine, $\text{C}_6\text{H}_{13}\text{NO}_4$) and N-(2-hydroxy-1,1-bis(hydroxymethyl)ethyl)glycine, (Tricine, $\text{C}_6\text{H}_{13}\text{NO}_5$), (figure 1.9).

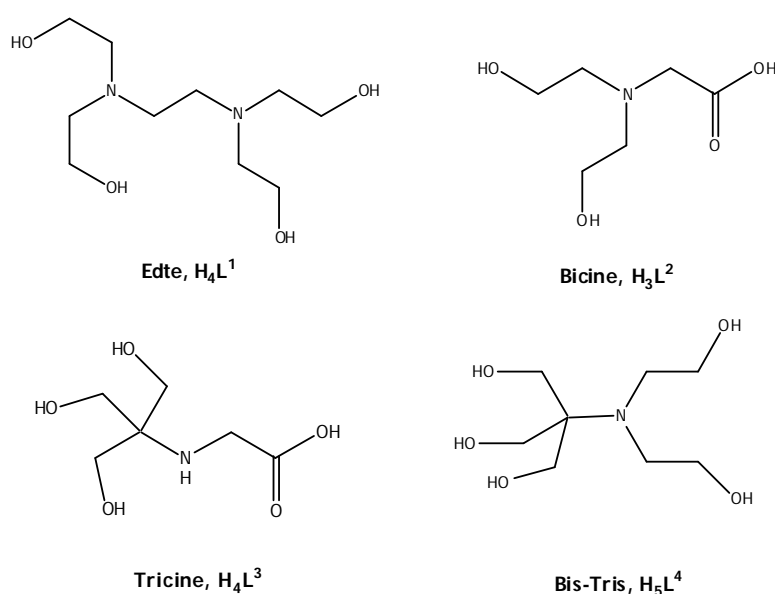


Figure 1.9: Ligands investigated

These ligands were chosen due to their flexibility and their multiple donor atoms providing many possible binding sites for transition metal ions leading to large polymetallic clusters. With the exception of bis-tris the coordination chemistry of the ligands listed above have been previously unexplored or only partially explored with first row transition metal ions. We planned to use these ligands to develop synthetic routes to new polymetallic clusters and SMMs.

1.13 Previous use of ligands

EDTE, (figure 1.9), has been used in the preparation of mononuclear Ba and Ca,⁵⁸ dinuclear Cu,⁵⁹ and V complexes.⁶⁰ Only the dinuclear V complex contains EDTE in the fully deprotonated form, where the two oxovanadium centers are coordinated to both the diethanolamine fragments of the edte ligand (figure 1.10). This multiple binding sites and flexibility of this ligand should produce larger clusters if the right conditions are found.

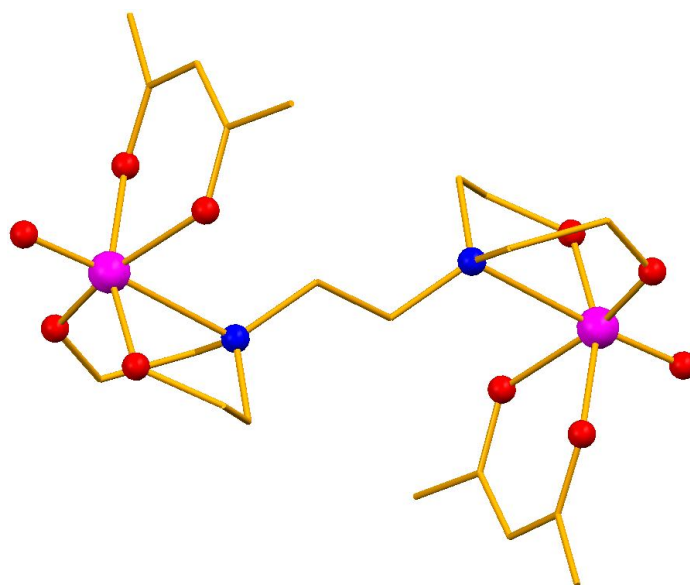


Figure 1.10: Structure depicting the binding mode of EDTE in the dinuclear vanadium complex $[\{VO(acac)\}_2(edte)]$. (Ball and stick representation with V(V), pink; C, brown; N, blue; O, red; H atoms are omitted for clarity).

Bicine, (figure 1.9), is a zwitterionic buffer commonly used in biochemistry and molecular biology. There has been only one polynuclear complex reported using bicine, an $[\text{Fe}_6\text{Bic}_6]$ wheel⁶¹ in which each ligand is tri-deprotonated, mononuclear Cu and lanthanide complexes,⁶² and a one dimensional Mn(II) chain,⁶³ (figure 1.11).

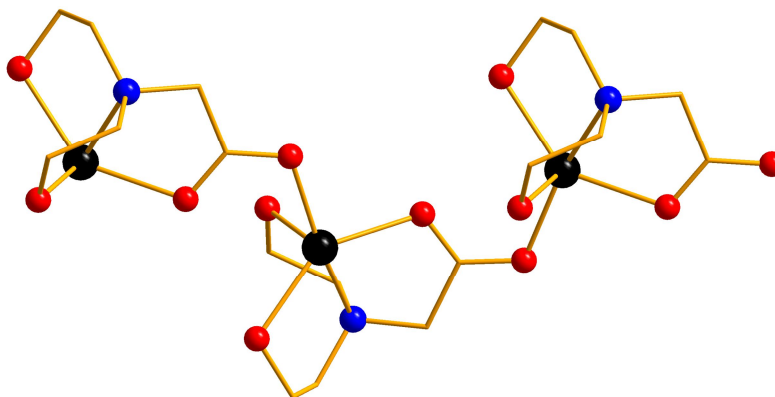


Figure 1.11: Structure depicting binding modes seen for bicine in 1-D Manganese chain. (Ball and stick representation with Mn(II), black; C, brown; N, blue; O, red; H atoms are omitted for clarity)

Tricine, (figure 1.9), is another zwitterionic buffer commonly used in electrophoresis. Only a few monomeric Cu, Ni and Zn complexes,⁶⁴ and a dimeric Sn complex are known.⁶⁵ It is interesting to note that only the COOH group and one CH_2OH arm are deprotonated in these complexes. We thought if more than two protons could be removed, it would be interesting to see the ligand's binding capabilities.

1.14 Experimental Techniques Used

1.14.1 Infrared spectroscopy

Infrared spectroscopy (IR) is a quick and relatively cheap spectroscopic technique which is useful in identifying certain functional groups. The absorption peaks correspond to the frequencies of vibrations between the bonds of the atoms present in organic materials.⁶⁶ These peaks form an IR spectrum which act as a fingerprint

specific to that compound. Therefore this technique is useful for our research. Although we cannot obtain a specific structure of any compound formed, we can learn valuable information about the functional groups present (if any) as well as use it for comparison purposes. This allows us to identify if any of our ligand is present in the sample or crystals, specific features being the C-N stretch at $\sim 1050\text{ cm}^{-1}$ and C-O stretch at $\sim 1400\text{ cm}^{-1}$ in our ligands. The IR spectrometer used was a Jasco FT-IR 4100 spectrometer, the diagram shown (figure 1.12).⁶⁶

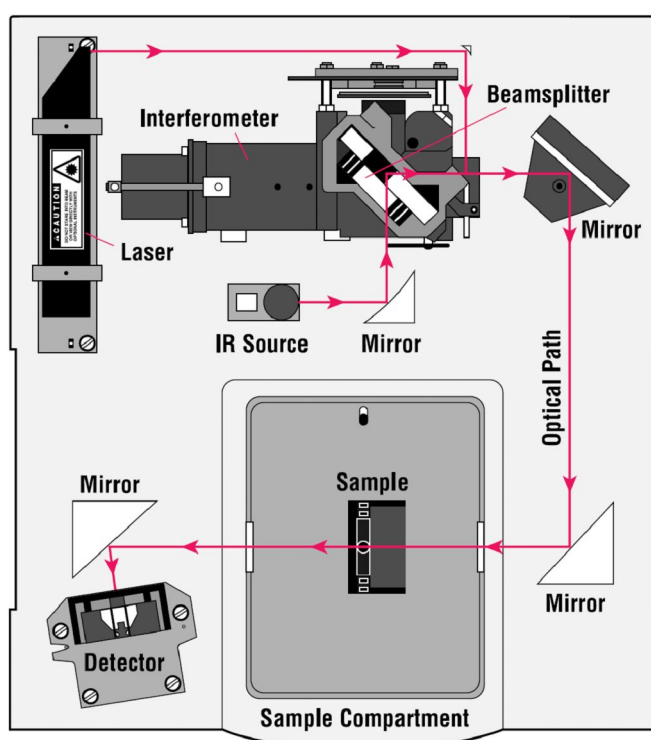


Figure 1.12: A simple diagram of in FT-IR spectrometer⁶⁶

The process involves an infrared beam being passed into the interferometer which uses a beamsplitter to divide the beam into two optical beams. One is reflected off a flat mirror which moves very short distances away from the splitter and the other is reflected off a fixed mirror. The two beams recombine at the beamsplitter and exit the interferometer as a signal, which is passed into the sample chamber via fixed and movable mirrors. The beam is passed through the sample and onto the detector where a final measurement is obtained before the signal is digitised and sent to the computer to produce an IR spectrum.

1.14.2 Single Crystal X-ray diffraction

X-ray diffraction is a powerful technique, which allows you to determine the position of the atoms within a crystal and determines whether magnetic characterisation of the structure obtained is necessary. The process of obtaining a final structure solution begins with the determination of a unit cell from initial matrix images. An X-ray source bombards the crystal producing scattered beams onto the detector, forming a diffraction pattern of reflections (figure 1.13).⁶⁷

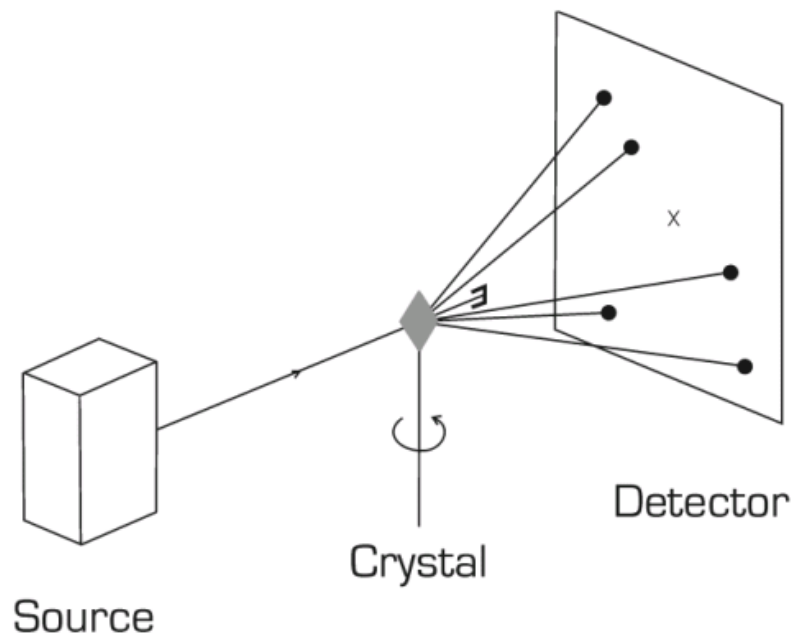


Figure 1.13: Schematic diagram of diffraction process

From this, the Bragg equation (equation 1.16) where λ is the wavelength of the incident x-rays used, d is the spacing of the planes between the atomic lattice and θ is the angle between the incident x-ray and the atomic lattice plane is used to determine the unit cell parameters.

$$n\lambda = 2d\sin\theta \quad (1.16)$$

The Bragg equation allows each reflection to be assigned a set of indices (hkl) which give the reflection a specific location in the diffraction pattern.⁶⁸ Once the

cell parameters have been found the correct bravais lattice can be assigned which allows the correct data collection strategy to be employed. Once the frames are collected, the individual reflections are processed to obtain accurate intensities for each reflection. This integration process includes the correction of absorption, polarization and Lorentz factors.⁶⁹ A hkl file is produced from this process from which the structure can be solved by either Patterson or Direct methods.

Direct methods solve by using electron densities and require some knowledge of chemical structures. This method is generally used for small light atom structures as the distribution of electron density needs to be evenly spread amongst atoms. In Patterson methods, peaks corresponding to vectors between pairs of atoms and vectors between pairs of heavy atoms give the largest peaks.⁷⁰ This allows you to locate a proportion of the total electron density of the structure. For this reason Patterson methods are preferred when solving inorganic structures. All the atoms are not always found any missing have to be located using difference Fourier maps. After this, the positions of the atoms have to be refined using the method of least squares. The least squares method finds the best agreement between calculated and observed diffraction patterns, minimising the sum of the squares of differences between the two, similar to fitting a straight line graph.⁷⁰ Each least squares refinement improves the structure and the process is repeated until the change of parameters are negligible. After this refinement the final difference map should have no more significant peaks and the residual factor, R-factor, which is a measure of agreement between observed and calculated reflections should be typically lower than 0.05. This process leads to a successful structural description of the crystal, however, synthesis of high quality crystals are needed for this technique which are not always possible to grow.

1.14.3 Superconducting Quantum Interference Device (SQUID) magnetometer

The magnetic properties of our new complexes formed are measured using the SQUID. It is a highly sensitive device, however it does not directly detect a magnetic field from the sample. When a measurement takes place, the sample is moved through super conducting detection coils and the magnetic moment of the sample induces an electric current (figure 1.14).⁷¹

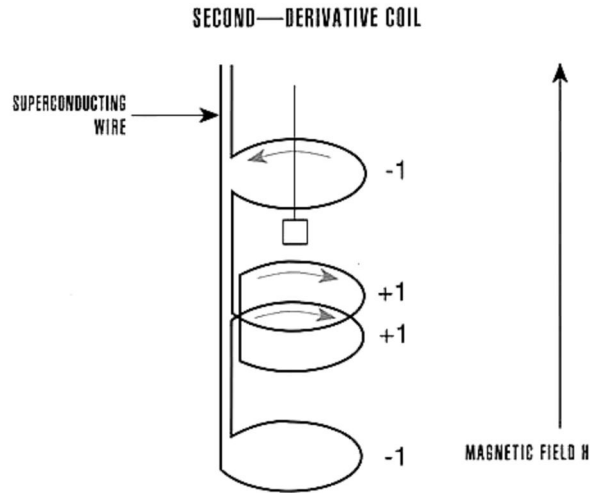


Figure 1.14: Schematic diagram of a super-conducting detection coil.⁷¹

A closed superconducting loop is formed between the detection coils, connecting wires and the SQUID input coil meaning that any change in current will cause a similar change in the SQUID output voltage which is proportional to the magnetic moment of the sample.⁷¹ As the sample is moved through the detection coils, the voltage is measured at certain positions and an output of the scan is produced (figure 1.15).

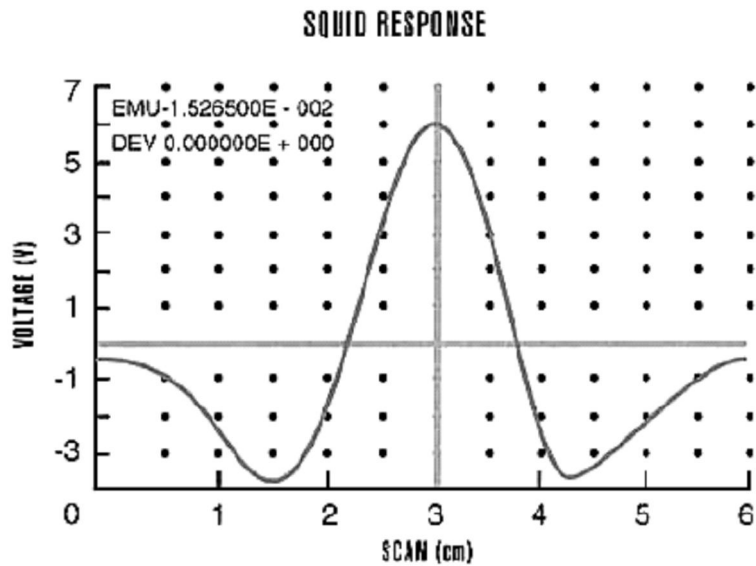


Figure 1.15: Output scan of the sample passed through the detector coil⁷¹

Our SQUID can measure a temperature range of 300 k - 1.8 K depending upon the measurement. For magnetisation versus field studies it can measure up to 5 tesla and up to 1500Hz for AC susceptibility measurements.

1.15 References

- ¹ O. Kahn; *Molecular Magnetism*, VCH publishers, **1942**.
- ² F. E. Mabbs, D.J. Machin; *Magnetism and Transition Metal Complexes*, Chapman and Hall, **1973**.
- ³ A. F. Orchard; *Magnetochemistry*, Oxford Chemistry Primer, **2003**.
- ⁴ B. N. Figgs, R. L. Martin; *J. Chem. Soc*, **1956**, 3837.
- ⁵ S. F. A. Kettle; *Physical Inorganic Chemistry: A Coordination Chemistry Approach*, Oxford University Press, **2000**.
- ⁶ G. Christou, D. Gatteschi, D. N. Hendrickson, R. Sessoli; *MRS Bulletin*, **2000**, 66.
- ⁷ T. Lis, *Acta. Cryst.*, **1980**, B36, 2042.
- ⁸ R. Sessoli, D. Gatteschi, A. Caneschi, M. A. Novak, *Nature*, **1993**, 365, 141.
- ⁹ M. A. Novak, R. Sessoli, A. Caneschi, D. Gatteschi; *J. Magn. Magn. Mater*, **1995**, 146, 211.
- ¹⁰ V. Marvaud, C. Decroix, A. Scniller, C. Guyard-Duhayon, J. Vaissermann, F. Gonnet, M. Verdaguer; *Chem. Eur. J.*, **2003**, 9, 1677.
- ¹¹ N. E. Chakov, S. C. Lee, A. G. Harter, P. L. Kuhns, A. P. Reyes, S. O. Hill, N. S. Dalal, W. Wernsdorfer, K. A. Abboud, G. Christou; *J. Am. Chem. Soc*, **2006**, 128, 6975.
- ¹² D. Martin; *introduction to AC Susceptibility*, Quantum Design.
- ¹³ J. Liu, B. Wu, L. Fu, R. B. Diener, Q. Niu; *Phys. Rev. B*, **2002**, 65, 224401.
- ¹⁴ N. V. Prokof'ev, P. C. E. Stamp; *Phys. Rev. Lett*, **1998**, 80, 5794; N. A. Sinitsyn, N. V. Prokof'ev; *Phys. Rev. Lett. B*, **2003**, 67, 134403.
- ¹⁵ I. Chiorescu, R. Giraud, A. G. M. Jansen, A. Caneschi, B. Barbara; *Phys. Rev. Lett*, **2000**, 85, 4807
- ¹⁶ A. Barra, A. Caneschi, A. Cornia, D. Gatteschi, L. Gornini, L. Heiniger, R. Sessoli, L. Sorace; *J. Am. Chem. Soc*, **2007**, 129, 35.
- ¹⁷ A. Cornia, R. Sessoli, L. Sorace, D. Gatteschi, A. L. Barra, C. Daugebonne; *Phys. Rev. Lett*, **2002**, 89, 257201.
- ¹⁸ A. Cornia, A. C. Fabretti, R. Sessoli, L. Sorace, D. Gatteschi, A. L. Barra, C. Daugebonne, T. Roisnel; *Acta. Crystallogr. Sec. C*, **2002**, 58, 391.
- ¹⁹ R. Amigó, E. del Barco, L. Casas, E. Molins, J. Tejada, I. B. Rutel, B. Mommouton, N. Dalal, J. Brookes; *Phys. Rev. B*, **2002**, 65, 172403.
- ²⁰ (a) S. Hill R. S. Edwards, S. I. Jones, N. S. Dalal, J. M. North; *Phys. Rev. Lett.* **2003**, 90, 217204;
(b) E. del Barco, A. D. Kent, E. M. Rumberger, D. N. Hendrickson, G. Christou; *Phys. Rev. Lett.* **2003**, 91, 047203.
- ²¹ K. Wieghardt, K. Pohl, I. Jibril, G. Huttner; *Angew. Chem. Int. Ed. Engl*, **1984**, 23, 77.
- ²² D. Gatteschi, R. Sessoli, J. Villain; *Molecular Nanomagnets*, 1st Ed., Oxford University Press, New York, **2006**.
- ²³ C. Delfs, D. Gatteschi, L. Pardei, R. Sessoli, K. Wieghardt, D. Hanke; *Inorg. Chem*, **1993**, 32, 3099.
- ²⁴ A. L. Barra, P. Debrunner, D. Gatteschi, C. E. Schulz, R. Sessoli; *Europhys. Lett*, **1996**, 35, 133; A. L. barra, D. Gatteschi, R. Sessoli; *Chem. Eur. J*, **2000**, 6, 1608.

- ²⁵ (a) A. Mulkin, B. Gorhunov, M. Dressel, C. Sangregorio, D. Gatteschi; *Phys. Rev. Lett*, **2001**, 63, 214411; (b) W. Wernsdorfer, T. Ohm, C. Paulsen, R. Sessoli, D. Mailly, C. Paulsen, *Phys. Rev. Lett*, **1999**, 82, 3903.
- ²⁶ A. L. Barra, A. Caneschi, A. Cornia, F. Fabrizi de Biani, D. Gatteschi, C. Sangregorio, R. Sessoli, L. Sorace; *J. Am. Chem. Soc*, **1999**, 121, 5302.
- ²⁷ A. Cornia, A. C. Fabretti, P. Garrisi, C. Mortalo, D. Bonacchi, D. Gatteschi, R. Sessoli, L. Sorace, W. Wernsdorfer, A. L. Barra; *Angew. Chem. Int. Ed*, **2004**, 43, 1136.
- ²⁸ G. Aromí, E. K. Brechin; *Struct. Bonding*, (Berlin, Ger.), **2006**, 122, 1.
- ²⁹ L. K. Thompson, O. Waldmann, Z. Xu; *Coord. Chem. Rev*, **2005**, 249, 2677.
- ³⁰ J. Larionova, M. Gross, M. Pilkington, H. Anders, H. Stoekli-Evans, H. U. Güdel, S. Decurtins; *Angew. Chem. Int. Ed*, **2000**, No 9, 1667.
- ³¹ T. Glaser, M. Heidemeier, T. Weyhermüller, R. D. Hoffman, H. Rupp, P. Muller; *Angew. Chem. Int. Ed*, **2006**, 45, 6033.
- ³² J. Kim, S. Han, J. M. Lim, K. Y. Choi, H. Nojiri, B. J. Suh; *Inorg. Chem. Acta*, **2007**, 360, 2647.
- ³³ A. Cornia, A. C. Fabretti, P. Garrisi, C. Mortalo, D. Bonacchi, R. Sessoli, L. Sorace, A. L. Barra, W. Wernsdorfer; *Journal Magn. Mater*, **2004**, 272-276, E749.
- ³⁴ C. J. Milios, A. Vinslava, W. Wernsdorfer, S. Moggach, S. Parsons, S. P. Perlepes, G. Christou, E. K. Brechin; *J. Am. Chem. Soc*, **2007**, 129, 2754.
- ³⁵ G. Christou; *Polyhedron*, **2005**, 24, 2065.
- ³⁶ D. Gatteschi, R. Sessoli, J. Villain; *Molecular nanomagnets*, Oxford University Press, **2006**.
- ³⁷ A. J. Tasiopoulos, A. Vinslava, W. Wernsdorfer, K. A. Abboud, G. Christou; *Angew. Chem. Int. Ed*, **2004**, 2117.
- ³⁸ R. H. Laye, E. J. L. McInnes; *Euro. J. Inorg. Chem*, **2004**, 2811.
- ³⁹ M. I. Khan, J. Zubieta; *Prog. Inorg. Chem*, **1995**, 43, 1.
- ⁴⁰ D. M. Low, L. F. Jones, A. Bell, E. K. Brechin, T. Mallah, E. Rivère, S. J. Teat, E. J. L. McInnes; *Angew. Chem. Int. Ed*, **2003**, 42, 3781.
- ⁴¹ R. Shaw, R. H. Laye, L. F. Jones, D. M. Low, C. Talbot-Eeclaers, Q. Wei, C. J. Milios, S. Teat, M. Helliwell, J. Rafferty, M. Evangelisti, M. Affront, D. Collinson, E. K. Brechin, E. J. L. McInnes; *Inorg. Chem*, **2007**, 46, 4968.
- ⁴² D. J. Price, M. Murrie; *Annu. Rep. Prog. Chem*, **2007**, Sec A, 103, 20.
- ⁴³ C. J. Milios, A. Vinslava, A. G. Whittaker, S. Parsons, W. Wernsdorfer, G. Christou, S. P. Perlepes, E. K. Brechin; *Inorg. Chem*, **2006**, 45, 5272.
- ⁴⁴ I. A. Gass, C. J. L. Milios, A. G. Whittaker, F. P. A. Fabiani, S. Parsons, M. Murrie, S. P. Perlepes, E. K. Brechin; *Inorg. Chem*, **2006**, 45, 5281.
- ⁴⁵ C. J. Milios, A. Presconone, J. Sanchez-Benitez, S. Parsons, M. Murrie, E. K. Brechin; *Inorg. Chem*, **2006**, 45, 7053.
- ⁴⁶ A. Ardavan, O. Rival, J. J. L. Morton, S. J. Blundell, A. M. Tyryshkin, G.A. Timco, R.E.P. Winpenny; *Phys. Rev. Lett*, **2007**, 98, 057201/1.

- ⁴⁷ B. Cage, S. E. Russek, R. Shoemaker, A. J. Barker, C. Stoldt, V. Ramachandaran, N. S. Dalal; *Polyhedron*, **2007**, 26, 2413.
- ⁴⁸ M. Manoli, R. D. L. Johnstone, S. Parsons, M. Murrie, M. Affronte, M. Evangelisti, E. K. Brechin; *Angew. Chem. Int. Ed.*, 2007, 46, 4456.
- ⁴⁹ L. Bogani, W. Wernsdorfer; *Nature. Mat.* **2008**, 7, 179.
- ⁵⁰ A. Cornia, A. C. Fabretti, M. Pacchioni, L. Zobbi, D. Bonacchi, A. Caneschi, D. Gatteschi, R. Biagi, U. Del Pennino, V. De Renzi, L. Gurevich and H. S. J. Van der Zant; *Angew. Chem. Int. Ed.*, **2003**, 42, 1645.
- ⁵¹ G. G. Condorelli, A. Motta, I. L. Fragalà, F. Giannazzo, V. Raineri, A. Caneschi, D. Gatteschi; *Angew. Chem. Int. Ed.*, **2004**, 43, 4081.
- ⁵² L. Zobbi, M. Mannini, M. Pacchioni, G. Chastanet, D. Bonacchi, C. Zanardi, R. Biagi, U. Del Pennino, D. Gatteschi, A. Cornia, R. Sessoli; *Chem. Commun.*, **2005**, 1640.
- ⁵³ E. Coronado, A. Forment-Aliaga, F. M. Romero, V. Corradini, R. Biagi, V. De Renzi, A. Gambardella, U. del Pennino; *Inorg. Chem.*, **2005**, 44, 7693.
- ⁵⁴ (a) M. Clemente-León, H. Soyer, E. Coronado, C. Mingotaud, C. J. Gómez-García, P. Delhaès; *Angew. Chem. Int. Ed.*, **1998**, 37, 2842; (b) M. Clemente-León, E. Coronado, A. Soriano-Portillo, C. Mingotaud, J.M. Dominguez-Vera; *Adv. Coll. Inter. Sci.* **2005**, 116, 193.
- ⁵⁵ A. Naitabdi, J.-P. Bucher, P. Gerbier, P. Rabu, M. Drillon; *Adv. Mater.*, **2005**, 17, 1612.
- ⁵⁶ S. Isaacman, R. Kumar, E. del Barco, A. D. Kent, J. W. Canary, A. Jerschow; *Polyhedron*. **2005**, 24, 2691.
- ⁵⁷ A. W. Ferguson; Synthesis and Characterisation of Single Molecule Magnets, PhD Thesis, **2007**.
- ⁵⁸ G. Hundal, M. S. Hundal, S. Obrai, N.S. Poonia, S. Kumar; *Inorg. Chem.* **2002**, 41, 8, 2077.
- ⁵⁹ A. S. de Sousa, M. A. Fernandes; *Polyhedron*. **2002**, 21, 1883.
- ⁶⁰ W. Plass; *Euro. J. Inorg. Chem.* **1998**, 799.
- ⁶¹ M. M. Khalil, A. Abboud, G. Christou; *Dalton Trans.* **2003**, 4552.
- ⁶² (a) A. Messimeri, C. P. Raptopoulou, V. Nastopoulos, A. Terzis, S. P. Perlepes, C. Papadimitriou; *Inorg. Chim. Acta*, **2002**, 336, 8; (b) H. Yamaguchi, Y. Inomata, T. Takeuchi; *Inorg. Chim. Acta*, **1990**, 172, 105; (c) X.-F. He, L.-S. Long, X.-Y. Le, X.-M. Chen, L.-N. Ji and Z.-Y. Zhou, *Inorg. Chim. Acta*, **1999**, 285, 326; (d) H. Thakuria, G. Das, *Polyhedron* **2007**, 26, 149.
- ⁶³ Z. Sun, P. K. Gantzel, D. N. Hendrickson; *Polyhedron*, **1997**, 16, 3267.
- ⁶⁴ L. Menabue, M. Saladini; *J. Cryst. Spect. Res.* **1992**, 22, 6.
- ⁶⁵ Q-Y. Luo, X-R. Zeng, Y. Sui, X-F. Li; *Acta. Cryst.* **2005**, E61, m2604.
- ⁶⁶ Thermo Nicolet; Introduction to Fourier Transformation Infrared Spectroscopy.
- ⁶⁷ M. S. Weiss; *X-ray crystallography in 5401 seconds*, **2001**.
- ⁶⁸ C. F. Campana; *X-ray diffraction*, Bruker Axs, **2000**.
- ⁶⁹ W. Massa; *Crystal Structure determination*, Springer.
- ⁷⁰ W. Clegg; *Small-molecule single-crystal diffraction*, **2006**.
- ⁷¹ M. McElfresh; *Fundamentals of magnetism and magnetic measurements*, Quantum design, **1994**.

2.0 Synthesis of Iron complexes: EDTE

As mentioned previously, the discovery that the complex Fe_8^1 displayed SMM behaviour sparked wide research into the synthesis of these complexes using this ion. Iron(III) seems a very logical choice of ion to investigate. The characteristic of a large spin ground state for a SMM could be easily achieved by ferromagnetic coupling of two iron(III) ions (spin 5/2) to give an $S = 5$ ground state. However one major drawback of using iron (III) as the metal centre is that antiferromagnetic interactions tend to dominate between the iron centres, which reduces the overall spin of the cluster.^{2,3} Nevertheless some complexes do display large spin ground states through spin frustration effects,^{4,5} An example of this is the isomerism of two complexes $[\text{Fe}_6\text{O}_2(\text{OH})_2(\text{O}_2\text{CBu}^\dagger)_{10}(\text{hep})_2]$ and $[\text{Fe}_6\text{O}_2(\text{OH})_2(\text{O}_2\text{CPh})_{10}(\text{hep})_2]$, both $S = 5$, to $[\text{Fe}_6\text{O}_2(\text{OH})(\text{O}_2\text{CBu}^\dagger)_9(\text{hep})_4]$ and $[\text{Fe}_6\text{O}_2(\text{OH})(\text{O}_2\text{CPh})_9(\text{hep})_4]$, both $S = 0$ (where hepH is the ligand 2-(2-hydroxyethyl)pyridinate) reported in 2004 by Chistou *et al.*⁶ Both sets of complexes are composed of two triangular units which lead to spin frustration within the system and results in different ground state spins. The subtle change in bridging ligands between the two sets of complexes alters the position of the most 'frustrated' bonds (figure 2.1, 2.2) and leads to a change in spin ground state from 5 to 0.

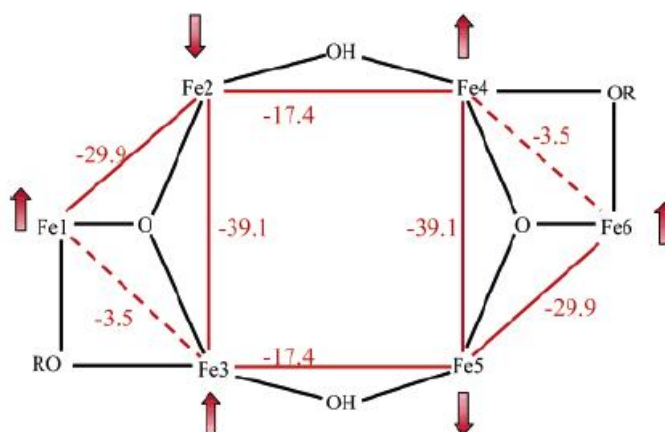


Figure 2.1: exchange interaction of two $S = 5$ complexes, dashed lines represent the most frustrated bonds. Numbers in red are exchange constants, Red arrows indicate spin of the ion

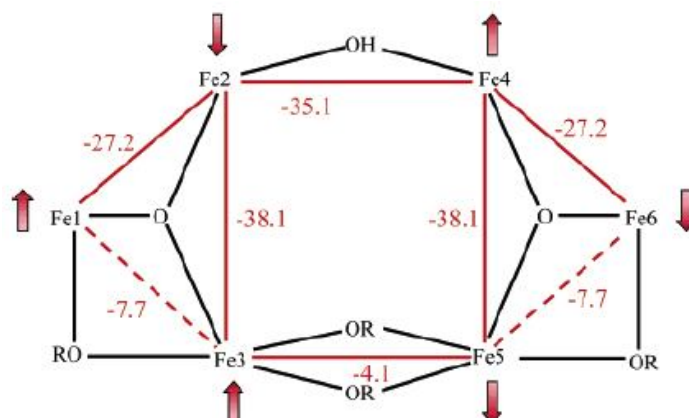


Figure 2.2: exchange interactions of two $S = 0$ complexes; dashed lines representing most frustrated bonds. Numbers in red are exchange constants, Red arrows indicate spin of the ion⁶

Non-frustrated systems also display non-zero ground states: one of the best being the aforementioned $[\text{Fe}_{14}(\text{bta})_6\text{O}_6(\text{OMe})_{18}\text{Cl}_6]$ ($S = 25$).⁷ Despite the problems associated with Fe(III) there have been many Fe SMMs synthesised ranging in nuclearity from four,⁸ eight,¹ a family of Fe_9 SMMs with mixed-valence Fe ions,⁹ eleven,¹⁰ to $[\text{Fe}_{19}(\text{metheidi})_{10}(\text{OH})_4\text{O}_6(\text{H}_2\text{O})_{12}][\text{NO}_3]$,¹¹ which retains the highest spin ground state for any iron SMM to date. The synthetic routes employed in the synthesis of these structures range from the reaction of simple iron salts with a variety of ligands, to the use of preformed iron complexes with polydentate ligands.^{12,13,14} We have chosen to explore the reaction of preformed oxo-centred triangles with flexible polydentate ligands. Figure 2.3 shows both a mixed valence iron triangle and an all Fe(III) triangle using acetate as a bridging ligand.

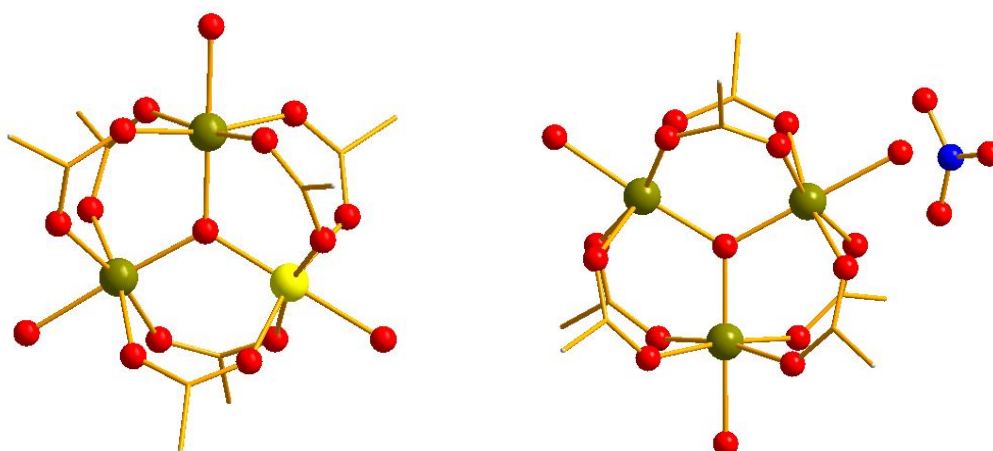


Figure 2.3: A mixed-valence iron triangle $[\text{Fe}_2^{\text{III}}\text{Fe}^{\text{II}}\text{O}(\text{OAc})_6(\text{H}_2\text{O})_3]$ and an all Fe(III) triangle $[\text{Fe}_3\text{O}(\text{OAc})_6(\text{H}_2\text{O})_3][\text{NO}_3]$. The Fe(III); Gold, Fe(II); Yellow; C; Brown, O; Red, N; Blue.

The beauty of these building blocks is that they can be mixed valence allowing for possible substitution of the Fe^{2+} ion for other M^{2+} ions and the carboxylate bridging ligands can be easily substituted making it possible to produce a range of different clusters. The triangles we focused on involved using pivalate, acetate, 2-phenoxybenzoate and benzoate as the carboxylate bridging ligands, which when combined in solution with our ligand of choice produced several new iron complexes. The synthesis, structure and magnetic characterisation of these complexes are reported below.

2.1 Synthesis of oxo-centred triangle starting materials

2.1.1. Synthesis of $[\text{Fe}_3\text{O}(\text{piv})_6(\text{H}_2\text{O})_3][\text{piv}][\text{Hpiv}] \cdot \text{EtOH} \cdot 2\text{H}_2\text{O}$

$\text{Fe}(\text{NO}_3)_3 \cdot 9\text{H}_2\text{O}$ (10 g, 24.8 mmol) was added to a stirred solution of pivalic acid, Hpiv (30 g, 294 mmol). The resultant solution was heated slowly to 160°C over three hours until the elimination of NO_2 was complete. The solution was then cooled to 70°C . EtOH (120 ml) then H_2O (30 ml) was added to the reaction mixture slowly with stirring. The final solution was left to stand overnight resulting in red / brown crystals of the target compound that were collected by filtration. Selected IR data: $\nu = 2959, 1585, 1483, 1380, 1362, 1227, 899, 787, 639 \text{ cm}^{-1}$. Crystals analyse as (%) calc. (found): C, 44.82 (44.72); H, 8.07 (7.81).

After ~1 week the product loses solvent to give $[\text{Fe}_3\text{O}(\text{piv})_6(\text{H}_2\text{O})_3][\text{piv}][\text{Hpiv}]$. Crystals analyse as (%) calc. (found): C, 45.13, (45.04); H, 7.57 (7.46).

2.1.2. Synthesis of $[\text{Fe}_3\text{O}(\text{OAc})_6(\text{H}_2\text{O})_3][\text{Cl}] \cdot \text{H}_2\text{O}$

$\text{FeCl}_3 \cdot 6\text{H}_2\text{O}$ (20 g, 74 mmol) was dissolved in H_2O (25 ml) and the resultant reaction mixture was stirred for 5 minutes. NaOAc (12 g, 146.3 mmol) was then added and the reaction mixture stirred for a further 5 minutes. The resultant solution was

filtered and the precipitate left to dry overnight, then was dissolved in MeCN (240 ml) and the reaction mixture left to stir until a copious amount of brown precipitate was observed (overnight). The final reaction mixture was filtered and the solvent reduced in *vacuo*, to give a brown precipitate. Selected IR data: $\nu = 3448$ (broad), 1577, 1409, 1346, 1028, 657 cm^{-1} . Analyses (%) calc. (found): C, 22.34 (22.12); H, 4.06 (4.03).

2.1.3 Synthesis of $[\text{Fe}_2^{\text{III}}\text{Fe}^{\text{II}}\text{O}(\text{OAc})_6(\text{H}_2\text{O})_3]$

$\text{FeCl}_2 \cdot 4\text{H}_2\text{O}$ (20 g, 100 mmol) and NaOAc (20 g, 243.8 mmol) were stirred into a solution of H_2O (100 ml) and acetic acid (60 ml). The resultant reaction mixture was refluxed for 2 hours between 70-80°C to give a brown precipitate. After this time, the reaction mixture was left to cool, stirring overnight. The final solution was filtered and the precipitate collected by filtration and washed with EtOH/ Et₂O. Selected IR data: $\nu = 3388$ (broad), 1577, 1407, 1345, 1034, 657, 615 cm^{-1} . Analyses (%) calc. (found): C, 23.63 (23.32); H, 4.30 (4.03).

2.1.4 Synthesis of $[\text{Fe}_3\text{O}(\text{OAc})_6(\text{H}_2\text{O})_3]\text{NO}_3$

$\text{Fe}(\text{NO}_3)_3 \cdot 9\text{H}_2\text{O}$ (20 g, 49.5 mmol) was dissolved in a minimum volume of H_2O . NaOAc (12 g, 146.3 mmol) was then added to this reaction mixture, slowly. The resultant solution was left to evaporate in a wide necked flask. After three days, the solution was filtered and the product obtained in the form of red / brown crystals. Selected IR data: $\nu = 3377$ (broad), 1581, 1519, 1412, 1348, 1030, 659 cm^{-1} . Analysis (%) calc. (found): C, 22.04 (19.89); H, 3.70 (3.55).

2.1.5 Synthesis of $[\text{Fe}_3\text{O}(\text{phbenz})_6(\text{MeOH})_3](\text{NO}_3) \cdot 3\text{MeOH}$

Phenoxybenzoic acid (1.284g, 5.99 mmol) was dissolved in MeOH (30ml). NaOMe (0.324g, 5.99 mmol) was then added to this reaction mixture. $\text{Fe}(\text{NO}_3)_3 \cdot 9\text{H}_2\text{O}$ (1.212g, 3 mmol) was dissolved in MeOH (30ml) and this solution was added dropwise to the first solution. The resultant reaction mixture was left to stir for 4 days, with slow evaporation of solvent, after which an orange precipitate had formed. The precipitate was collected by filtration. Selected IR data: $\nu = 3554$,

1588, 1479, 1397, 1219, 881, 749, 619 cm^{-1} . Precipitate analysis (%) calc. (found): C, 58.55 (58.45); H, 4.91 (4.54); N, 0.81 (1.08).

2.1.6 Synthesis of $[\text{Fe}^{\text{III}}\text{Fe}^{\text{II}}\text{O}(\text{OBz})_6(\text{H}_2\text{O})_2(\text{MeCN})]$

$\text{FeCl}_2 \cdot 4\text{H}_2\text{O}$ (3 g, 15 mmol) was dissolved in H_2O (50 ml). Sodium benzoate (7.5 g, 52 mmol) was dissolved in H_2O (100 ml) and slowly added to the $\text{FeCl}_2 \cdot 4\text{H}_2\text{O}$ solution. MeCN (25 ml) was then added to the resultant solution and the reaction mixture left to stir overnight. The reaction mixture was then filtered and the precipitate dried on a sinter to give the final product. Selected IR data: $\nu = 3376$ (broad), 1596, 1542, 1446, 1372, 1175, 1071, 1025, 839, 817, 717, 670 cm^{-1} . Precipitate analysis (%) calc. (found): C, 51.36 (51.01); H, 3.90 (3.50).

2.2 Synthesis of complexes containing edte H_4L^1

2.2.1 Synthesis of $[\text{Fe}_{12}\text{O}_4(\text{OH})_2(\text{L}^1)_4(\text{OAc})_8][\text{Cl}]_2 \cdot 2\text{H}_2\text{O}$ ($1 \cdot 2\text{H}_2\text{O}$)

To a stirred solution of $[\text{Fe}_3\text{O}(\text{OAc})_6(\text{H}_2\text{O})_3]\text{Cl}$ (0.5 g, 0.9 mmol) in MeCN (20 ml), H_4L^1 (0.11 g, 0.45 mmol) was added, followed by Et_2NH (0.1 g, 1.3 mmol). The solution was stirred overnight then filtered to give a dark red solution and a small amount of precipitate. Small portions of the solution were taken and layered with Et_2O by vapour diffusion. After 4 days well-defined dark orange blocks were observed in vapour diffusion experiments in approximately 12 % yield. Selected IR data: $\nu = 3364$, 2873, 1626, 1560, 1443, 1335, 1286, 1089, 1059, 903, 763 cm^{-1} . Air-dried crystals analyse as $1 \cdot 4\text{H}_2\text{O}$, analysis (%) calc. (found): C, 29.08 (28.80); H, 4.97 (5.40); N, 4.85 (4.93).

2.2.2 Synthesis of $[\text{Fe}_6\text{O}_2(\text{HL}^1)_2(\text{phbenz})_8] \cdot \text{MeCN}$ ($2 \cdot \text{MeCN}$)

To a stirred solution of $[\text{Fe}_3\text{O}(\text{phbenz})_6(\text{MeOH})_3](\text{NO}_3) \cdot 3\text{MeOH}$ (0.5 g, 0.3 mmol) in MeCN (20 ml), H_4L^1 (0.07 g, 0.3 mmol) was added. The solution was stirred overnight then filtered to give a dark red solution with no precipitate collected. Small portions of the solution were taken and layered with Et_2O by vapour diffusion. The remaining solution was stored in a sealed vial. After 1 month small brown

crystals were observed in the sealed vial in approximately 15 % yield. Selected IR data: $\nu = 1584, 1478, 1445, 1394, 1332, 1228, 1159, 1088, 878, 748, 691, 665 \text{ cm}^{-1}$. Air-dried crystals analyse as $2 \cdot \text{MeCN} \cdot 2\text{H}_2\text{O}$, analysis (%) calc. (found): C, 57.89 (57.84); H, 4.59 (4.45); N, 2.68 (2.95).

2.2.3 Synthesis of $[\text{Fe}_6\text{O}_2(\text{HL}^1)_2(\text{piv})_8] \cdot \text{MeCN}$ ($3 \cdot \text{MeCN}$)

To a stirred solution of $[\text{Fe}_3\text{O}(\text{piv})_6(\text{H}_2\text{O})_3][\text{piv}][\text{Hpiv}] \cdot \text{EtOH} \cdot 2\text{H}_2\text{O}$ (0.5 g, 0.44 mmol) in MeCN (20 ml), H_4L^1 (0.1 g, 0.44 mmol) was added. The solution was stirred overnight then filtered to give a dark red solution with a small amount of precipitate collected. Small portions of the solution were taken and layered with Et_2O by vapour diffusion. The remaining solution was stored in a sealed vial. After 3 weeks, small brown crystals were observed in the sealed vial in approximately 13% yield. Selected IR data: $\nu = 1578, 1480, 1420, 1342, 1224, 1072, 907, 785, 691, 603 \text{ cm}^{-1}$. Air-dried crystals analyse as $3 \cdot \text{MeCN} \cdot 3\text{H}_2\text{O}$, analysis (%) calc. (found): C, 43.26 (43.01); H, 7.03 (6.73); N, 4.73 (4.59).

2.2.4 Synthesis of $[\text{Fe}^{\text{III}}\text{Fe}^{\text{II}}_2(\text{OBz})_2(\text{H}_2\text{L}^1)_2][\text{OBz}] \cdot \text{MeCN}$ ($4 \cdot \text{MeCN}$)

To a stirred solution of $[\text{Fe}_2^{\text{III}}\text{Fe}^{\text{II}}\text{O}(\text{OBz})_6(\text{H}_2\text{O})_2(\text{MeCN})]$ 0.5 g, 0.5 mmol) in MeCN (20 ml), H_4L^1 (0.07 g, 1.5 mmol) was added followed by Et_2NH (0.11 g, 1.5 mmol). The solution was stirred overnight then filtered to give a dark red solution with no precipitate collected. Small portions of the solution were taken and layered with Et_2O by vapour diffusion. The remaining solution was stored in a sealed vial. After 1 month, small brown crystals were observed in the sealed vial in approximately 11% yield. Selected IR data: $\nu = 3124, 2848, 1654, 1445, 1377, 1339, 1301, 1069, 898, 718, 632 \text{ cm}^{-1}$. Air-dried crystals analyse as $4 \cdot \text{MeCN}$, analysis (%) calc. (found): C, 50.07 (50.21); H, 5.58 (5.95); N, 7.78 (7.42).

2.2.5 Synthesis of $[\text{Fe}_2(\text{H}_2\text{L}^1)_2]$ (5)

To a stirred solution of $[\text{Fe}_2^{\text{III}}\text{Fe}^{\text{II}}\text{O}(\text{OAc})_6(\text{H}_2\text{O})_3]$ 0.5 g, 0.8 mmol) in MeCN (20 ml), H_4L^1 (0.06 g, 2.4 mmol) was added followed by Et_2NH (0.31 g, 4.2 mmol). The solution was stirred overnight then filtered to give a dark red solution with a small amount of precipitate collected. Small portions of the solution were taken and

layered with Et₂O by vapour diffusion. The remaining solution was stored in a sealed vial. After 6 weeks, small yellow crystals were observed in the sealed vial in approximately 9% yield. Selected IR data: $\nu = 2851, 1654, 1446, 1378, 1339, 1301, 1277, 1070, 899, 866, 715, 633 \text{ cm}^{-1}$. Air-dried crystals analyse as **5**, analysis (%) calc. (found): C, 43.87 (43.83); H, 7.03 (6.95); N, 9.30 (9.50).

2.3 Complexes Containing EDTE (H₄L¹)

2.3.1 Discussion of crystal structure of [Fe₁₂O₄(OH)₂(L¹)₄(OAc)₈][Cl]₂·2H₂O (1·2H₂O)

Complex **1**·2H₂O contains a dodecanuclear Fe(III) complex and crystallises in the cubic space group $F-43c$ with the asymmetric unit containing one-quarter of the unit formula (figure 2.4 where the atom suffix a, b and c signify symmetry equivalents, s.e). The [Fe₁₂O₄(OH)₂(L¹)₄(OAc)₈]²⁺ core consists of two almost planar layers of six Fe(III) centres, between three almost planar layers of oxygen centres (figure 2.5).

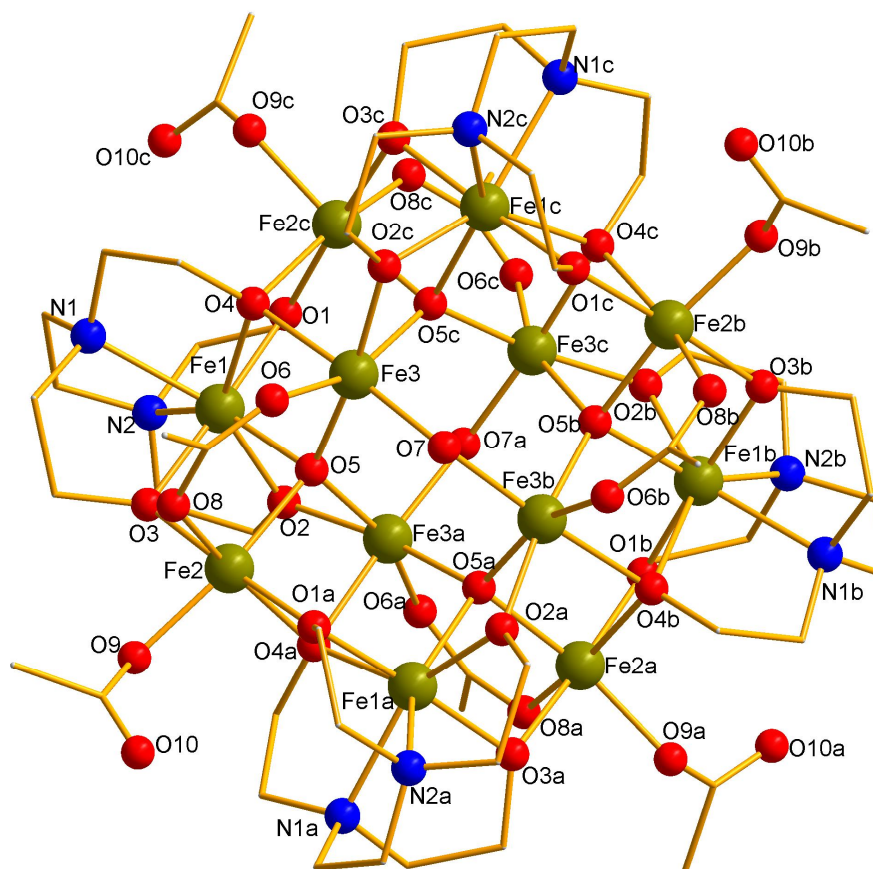


Figure 2.4: Structure of the cation of **1**. (ball and stick representation with Fe(III) gold; O, red; N, blue; C, brown; H atoms are omitted for clarity)[atom suffix a signifies the symmetry equivalent atom: $a = 1 - x, 1 - y, 1 - z$, b signifies the symmetry equivalent atom: $b = 1 - x, 1 - y, 1 - z$, c signifies the symmetry equivalent atom: $c = 1 - x, 1 - y, 1 - z$].

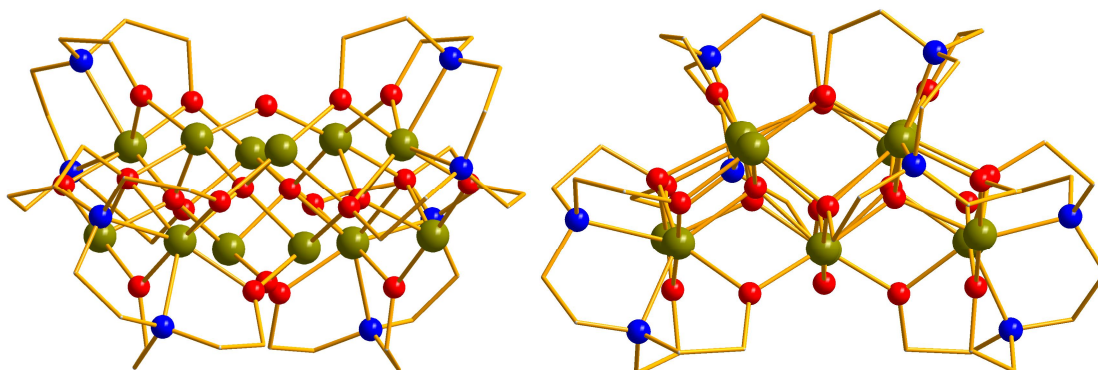


Figure 2.5: Side representations of the cation of **1** indicating the layering of Fe and O atoms.

All Fe centres are six-coordinate except for Fe1 (and s.e) which are seven-coordinate displaying a mono-capped trigonal prismatic geometry which is directed by the polydentate ligand geometry. This coordination number has been seen previously for similar Fe(III) complexes with the ligand EDTA.^{15,16} All twelve Fe centres are connected by four μ_4 -O²⁻ ions (O5 and symmetry equivalents), with two μ_2 -OH⁻ (O7 and O7a) bridging Fe3 to Fe3b and Fe3a to Fe3c respectively. Each ligand is hexadentate (figure 2.6) and tetra-deprotonated, capping four corners of the structure at Fe1 (and s.e). Three CH₂CH₂O⁻ arms are μ_2 -bridging Fe1-Fe2, Fe1-Fe2c and Fe1-Fe3a (through O3, O1 and O2 respectively) with the remaining arm is μ_3 -bridging Fe1, Fe2c and Fe3 through O4 (figure 2.6). The acetate ligands are present in two binding modes, four acetate ligands bind in the typical 1, 3 mode bridging the Fe2-Fe3 vectors. The other four acetate ligands are mono-dentate and complete the coordination sphere of Fe2 centres.

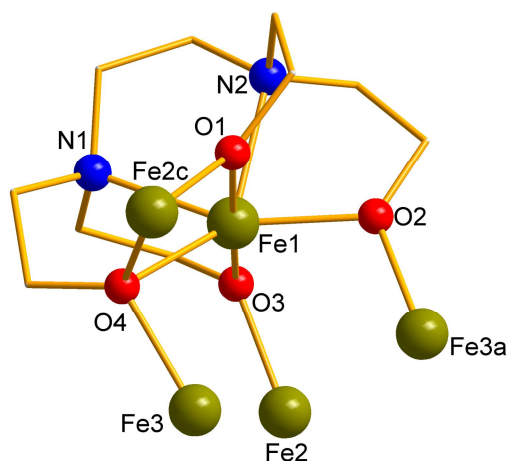


Figure 2.6: Ligand binding mode present in complex **1**

Complex **1**, is one of only a few dodecanuclear Fe(III) clusters known in the literature, which are mainly Fe(III) wheels or loop complexes.¹⁷ However other examples include a cluster composed of face-sharing defect cuboidal units¹⁸ or consisting of four edge sharing [Fe₃O]⁷⁺ units.¹⁹ At the time of synthesis, complex **1** was unique in Fe(III) chemistry, however Hendrickson *et al*²⁰ reported the synthesis of a related mixed valence manganese complex [Mn^{III}₈Mn^{II}₄O₄(OH)₂(L¹)₄Cl₆(H₂O)₂] in which the charge balance comes from an extra four Cl ions instead of the acetate

ligands present in our cluster. Recently Bagai *et al*²¹ published a similar Fe₁₂ complex, [Fe₁₂O₄(OH)₂(O₂CMe)₆(L¹)₄(H₂O)₂](ClO₄)₄ and other Fe(III) complexes using (H₄L¹) which will be discussed later. Interestingly Bagai's complex crystallises in the monoclinic space group *C2/c* and not the cubic space group *F-43c* as seen for our complex, resulting in different crystal packing (figure 2.7). The only differences being the anion employed (ClO₄ used instead of Cl) and starting from simple Fe(ClO₄)₃·6H₂O salt instead of our pre-formed triangle.

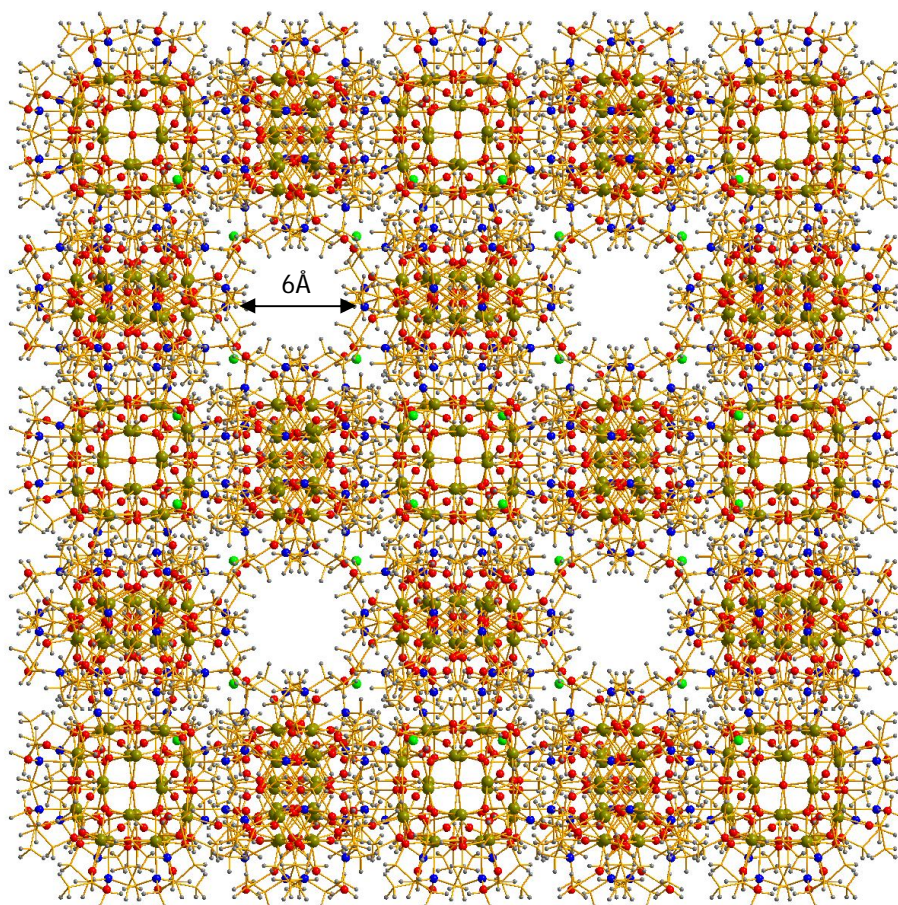


Figure 2.7: Crystal packing diagram of complex **1** (ball and stick representation with Fe(III) gold; O, red; N, blue; C, brown; H, Grey; Cl, Green. Double arrow indicates the size of the channels

The smaller Cl⁻ ions may allow a much closer packing between the clusters than the “bulky” perchlorate ion, which results in the formation of channels, approximately 6 Å in diameter within the crystal structure. If possible it would be interesting to

investigate the possibility of using complex **1** in gas absorption studies, examining whether these channels have the ability to uptake gas and hold it in the channels.

Table 2.1 Data for the crystal structure determination of **1**·2H₂O

Empirical formula	C ₆₀ H ₁₂₂ N ₁₀ O ₄₁ Fe ₁₂
fw(gmol ⁻¹)	2346.31
Spacegroup	<i>F</i> -43 <i>c</i>
<i>a</i> (Å)	39.1798(6)
<i>V</i> (Å ³)	60143.2(16)
<i>Z</i>	4
<i>T</i> (K)	100(2)
λ (Å)	0.71073
ρ_{calcd} (Mg/m ³)	1.499
μ (mm ⁻¹)	1.827
<i>R</i> ₁ (%)	5.75
<i>wR</i> ₂ (%)	15.91
Goodness of fit indicator	0.933

[†]Estimated standard deviations in the least significant figure are given in parentheses.

$$^a R_1 = \frac{\sum ||F_o| - |F_c||}{\sum |F_o|}$$

$$^b wR_2 = \left[\frac{\sum [w(F_o^2 - F_c^2)]}{\sum [w(F_o^2)]} \right]^{1/2}$$

where $w = 1/[\sigma^2(F_o^2) + (0.2P)^2]$ and $P = [F_o^2 + 2F_c^2]/3$

Table 2.2 Selected ligand bond distance for **1**·2H₂O

Bond	Distance (Å) [†]	Bond	Distance (Å) [†]
Fe1–N1	2.297(7)	Fe2–O3	1.991(5)
Fe1–N2	2.282(6)	Fe2–O4	2.108(5)
Fe1–O1	1.968(5)	Fe2c–O1	1.991(5)
Fe1–O2	2.231(5)	Fe3–O2	1.983(5)
Fe1–O3	1.986(5)	Fe3–O4	2.110(5)
Fe1–O4	2.231(5)		

[†] Estimated standard deviations in the least significant figure are given in parentheses.

Table 2.3 Selected bond angles for $1 \cdot 2\text{H}_2\text{O}$

Atoms	Angle ($^\circ$) [†]	Atoms	Angle ($^\circ$) [†]
Fe1—O1—Fe2c	112.73(2)	Fe1—O5—Fe2	98.00(2)
Fe1—O4—Fe2c	98.82(19)	Fe3—O7—Fe3b	135.00(3)
Fe1—O2—Fe3a	106.00(2)	Fe3—O5—Fe3a	125.66(2)
Fe1—O3—Fe2	105.30(2)	Fe1—O4—Fe3	97.12(19)
Fe1—O5—Fe3a	100.59(19)		

[†] Estimated standard deviations in the least significant figure are given in parentheses.

Table 2.4 Bond valence sums for the inorganic oxygen atoms in $1 \cdot 2\text{H}_2\text{O}$

Atom	BVS	Assignment*
O5	1.81	O ²⁻
O7	1.15	OH ⁻

* The oxygen atom is an O²⁻ if the BVS is ~2, an OH⁻ if the BVS is ~1, and an H₂O if the BVS is ~0.²²

2.3.1.1 Magnetic Susceptibility Measurements for $1 \cdot 2\text{H}_2\text{O}$

Magnetic susceptibility measurements were carried out on an air-dried sample. The χT value at 300K is 19.06 cm³ mol⁻¹ K, which is significantly lower than the expected value for twelve uncoupled Fe(III) ions of 52.5 cm³ mol⁻¹ K, indicating strong antiferromagnetic interactions within the cluster. The value of χT decreases sharply to a value of 0.35 cm³ mol⁻¹ K at 1.8 K, suggesting that the complex has a spin ground state of zero (figure 2.8). This is consistent with antiferromagnetic coupling, which is common in Fe(III) clusters.

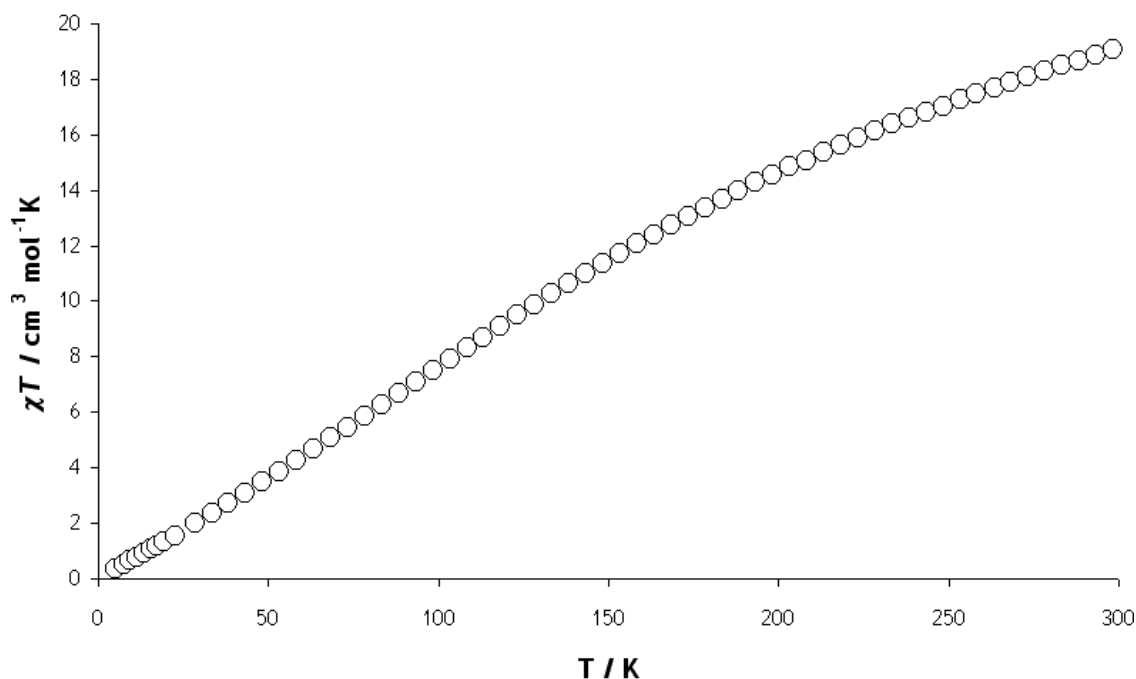


Figure 2.8: Temperature dependence of χT for **1** from 300-1.8 K measured in a field of 1 kOe

Bagai was able to synthesis a further two analogues of this complex, $[\text{Fe}_{12}\text{O}_4(\text{OH})_8(\text{L}^1)_4(\text{H}_2\text{O})_2](\text{ClO}_4)_4$ and $[\text{Fe}_{12}\text{O}_4(\text{OH})_8(\text{L}^1)_4(\text{H}_2\text{O})_2](\text{NO}_3)_4$ again using simple metal salts and altering the anion used resulting in the substitution of acetate groups or hydroxide ones. Although they were able to identify the core of the structure, both these complexes displayed disorder amongst the edte ligands resulting in poor refinement of the clusters. The magnetic data of all three complexes is consistent with our findings.

2.3.2 Discussion of crystal structure of $[\text{Fe}_6\text{O}_2(\text{HL}^1)_2(\text{Piv})_8] \cdot \text{MeCN}$ (**2**·MeCN)

Complex **2** is a hexanuclear Fe(III) complex and crystallises in the space group $P2_1/n$ (figure 2.9 where the atom suffix a signifies symmetry equivalents).

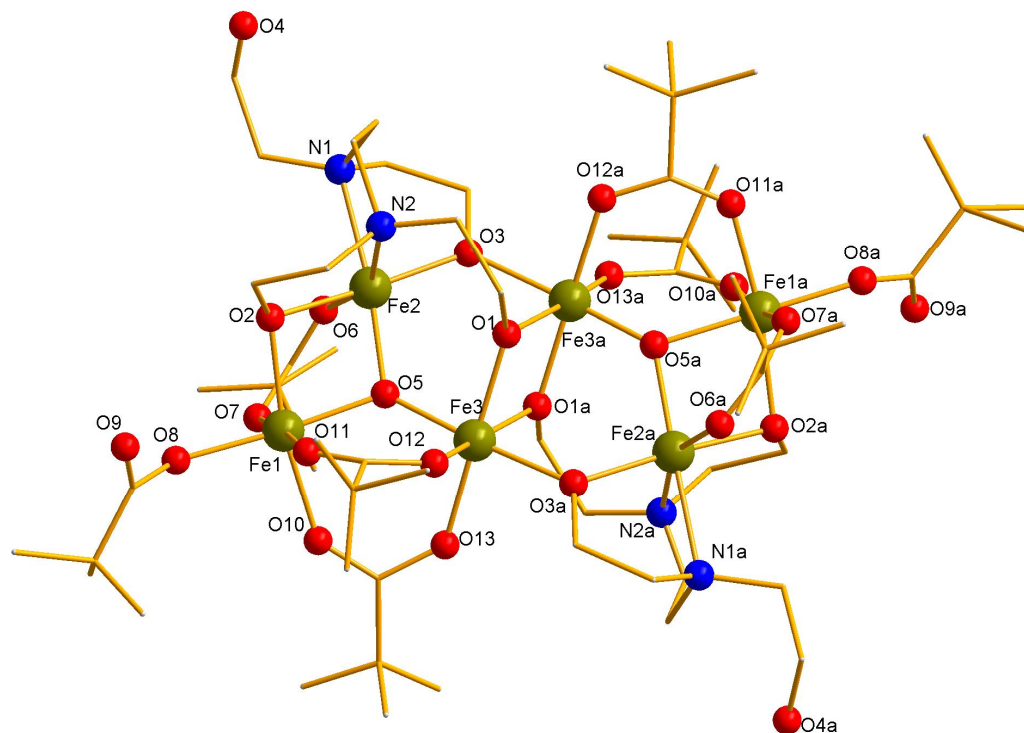


Figure 2.9: Structure of **2** (ball and stick representation with Fe(III) gold; O, red; N, blue; C, brown; H atoms are omitted for clarity)[atom suffix a signifies the symmetry equivalent atom: a = 1 _ x, 1 _ y, 1 _ z].

The structure core consists of two triangular $[\text{Fe}_3\text{O}]^{7+}$ units joined together by four O atoms from the $\text{CH}_2\text{CH}_2\text{O}^-$ arms of HL^1 , O1, O3 and s.e (figure 2.10).

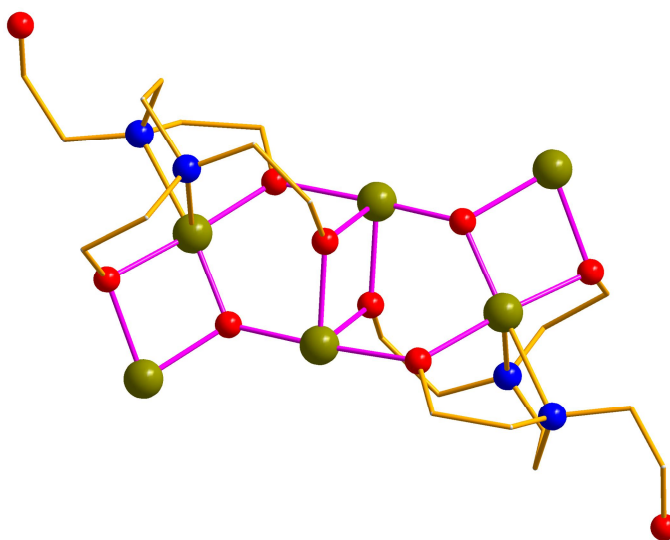


Figure 2.10: Core of complex **2** with carboxylate ligands removed

All Fe centres are six coordinate. Fe3 displays an octahedral geometry and is bound by three oxygen donor atoms from the ligand $\text{CH}_2\text{CH}_2\text{O}^-$ arms (O1a, O3a, O1), two oxygen donor atoms from pivalate ligands and a μ_3 -oxide (O5). Fe1 is bound by four oxygen donor atoms from pivalate ligands, one oxygen from a deprotonated ligand arm (O2) and also by μ_3 -oxide (O5). Fe2 displays a distorted octahedral geometry, bound by two oxygen atoms from $\text{CH}_2\text{CH}_2\text{O}^-$ arms (O3 and O2), one oxygen from a pivalate ligand and μ_3 -oxide (O5) completing the coordination sphere of Fe2. Six pivalate ligands display typical 1,3 bridging of Fe centres with the remaining two pivalate are monodentate. The ligand is present in one binding mode, μ_4 (figure 2.11). The final ligand alkoxide arm remains protonated and unbound, hydrogen bonding to a pivalate ligand (O9) on an adjacent Fe_6 molecule.

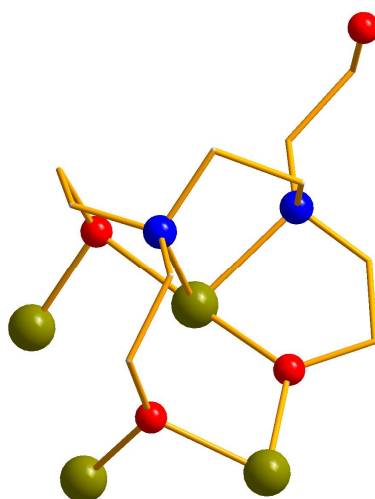


Figure 2.11: Binding mode of HL^1 present in **2**

There are many examples of Fe_6 clusters in literature showing a wide range of structural types. Some have planar arrays of Fe atoms,²³ twisted boat,²⁴ octahedral,²⁵ fused²⁶ or ladder butterfly units,²⁷ cyclic,²⁸ chain-like²⁹ and linked triangular units.³⁰ Of these, some clusters contain the same $[\text{Fe}_3\text{O}]^{7+}$ core found in our structure, however the bridging of the two triangular units comes from hydroxide and alkoxide ions, which makes complex **2** different from the previous examples. However during the course of this research this complex was published

by Bagai *et al*²¹ using a variation of our pre-formed pivalate triangle and using CHCl₃ as a solvent.

Table 2.5 Data for the crystal structure determination of **2**·MeCN

Empirical formula	C ₆₄ H ₁₂₆ N ₆ O ₂₉ Fe ₆
fw(gmol ⁻¹)	1778.82
Spacegroup	<i>P</i> 2 ₁ / <i>n</i>
<i>a</i> (Å)	16.008(2)
<i>b</i> (Å)	17.492(2)
<i>c</i> (Å)	30.083(4)
β(deg)	92.784(6)
<i>V</i> (Å ³)	8413.4(19)
<i>Z</i>	2
<i>T</i> (K)	100(2)
λ(Å)	0.71073
ρ _{calcd} (Mg/m ³)	1.354
μ(mm ⁻¹)	1.081
R ₁ (%)	12.80
wR ₂ (%)	32.19
Goodness of fit indicator	1.239

[†]Estimated standard deviations in the least significant figure are given in parentheses.

$${}^a R_1 = \frac{\sum ||F_o| - |F_c||}{\sum |F_o|}$$

$${}^b wR_2 = \left[\frac{\sum [w(F_o^2 - F_c^2)]}{\sum [w(F_o^2)]} \right]^{1/2}$$

$$\text{where } w = 1/[\sigma^2(F_o^2) + (0.2P)^2] \text{ and } P = [F_o^2 + 2F_c^2]/3$$

Table 2.6 Selected ligand bond distance for **2**·MeCN

Bond	Distance (Å) [†]	Bond	Distance (Å) [†]
Fe2–N1	2.220(3)	Fe3–O1	2.039(3)
Fe2–N2	2.271(4)	Fe2–O3	1.996(3)
Fe2–O2	2.049(3)	Fe1–O2	2.091(3)
Fe3–O5	1.847(3)	Fe3a–O1	2.043(3)
Fe2–O5	1.951(3)	Fe3a–O3	2.042(3)
Fe1–O5	1.943(3)		

[†] Estimated standard deviations in the least significant figure are given in parentheses.

Table 2.7 Selected bond angles for **2**·MeCN

Atoms	Angle (°) [†]	Atoms	Angle (°) [†]
Fe1–O5–Fe2	100.6(13)	Fe3–O2–Fe3a	100.7(12)
Fe1–O5–Fe3	126.9(15)	Fe2–O2–Fe1	92.78(11)
Fe2–O5–Fe3	124.8(16)	Fe2–O3–Fe3a	121.4(14)

[†] Estimated standard deviations in the least significant figure are given in parentheses.

Table 2.8 Bond valence sums for the inorganic oxygen atoms in **2**·MeCN

Atom	BVS	Assignment [*]
O5	1.89	O ²⁻

^{*} The oxygen atom is an O²⁻ if the BVS is ~2, an OH⁻ if the BVS is ~1, and an H₂O if the BVS is ~0.²²

2.3.2.1 Magnetic Susceptibility Measurements for 2·MeCN

Magnetic susceptibility measurements were carried out on an air-dried sample. For **2** the value of χT at 300K is $10.80 \text{ cm}^3 \text{ mol}^{-1} \text{ K}$, significantly lower than for six uncoupled Fe(III) ions ($26.25 \text{ cm}^3 \text{ mol}^{-1} \text{ K}$ for $g=2$), indicating strong antiferromagnetic interactions between the Fe(III) centres (figure 2.12).

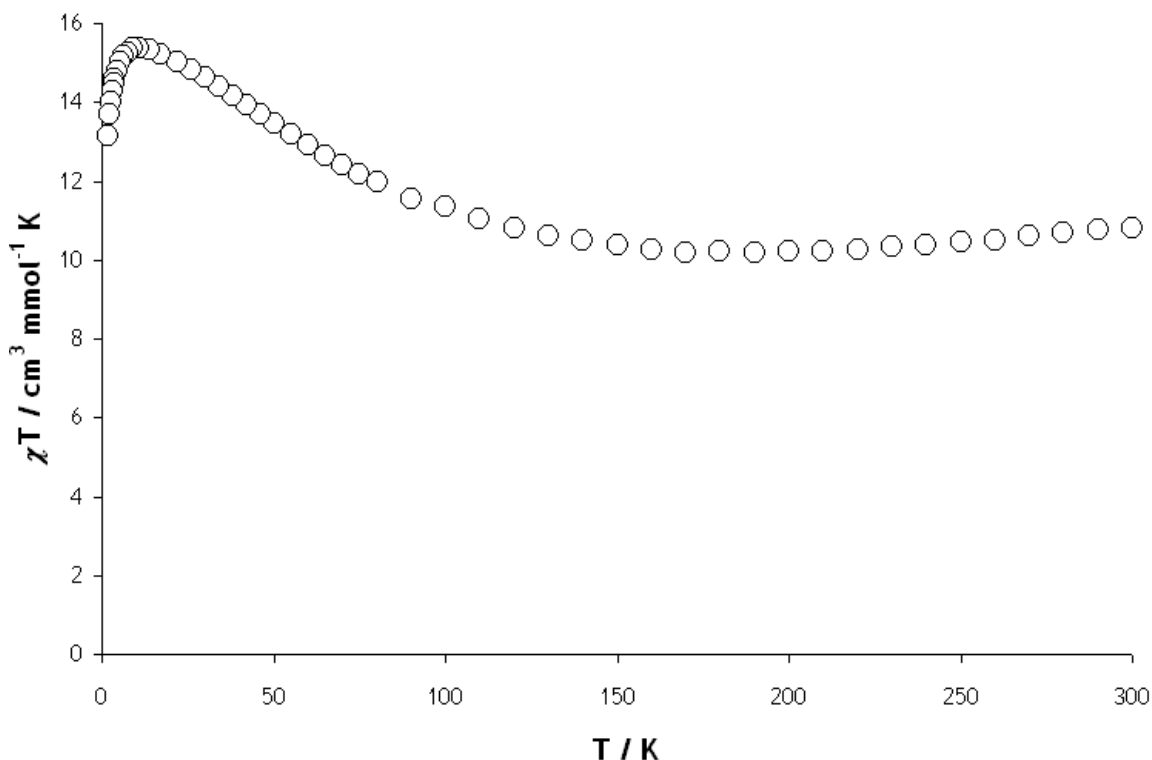


Figure 2.12: Temperature dependence of χT for **2** from 300-1.8 K measured in a field of 1 kOe

The value of χT increases steadily to a maximum of $15.35 \text{ cm}^3 \text{ mol}^{-1} \text{ K}$ at 9.0 K, then drops sharply to $13.12 \text{ cm}^3 \text{ mol}^{-1} \text{ K}$ at 1.8 K. This drop can be attributed to either zero-field splitting or intermolecular antiferromagnetic interactions. The magnetisation was measured as a function of applied field at 2 K, rising to a maximum value of $M/N\beta=10.24$ at 5 T (figure 2.13).

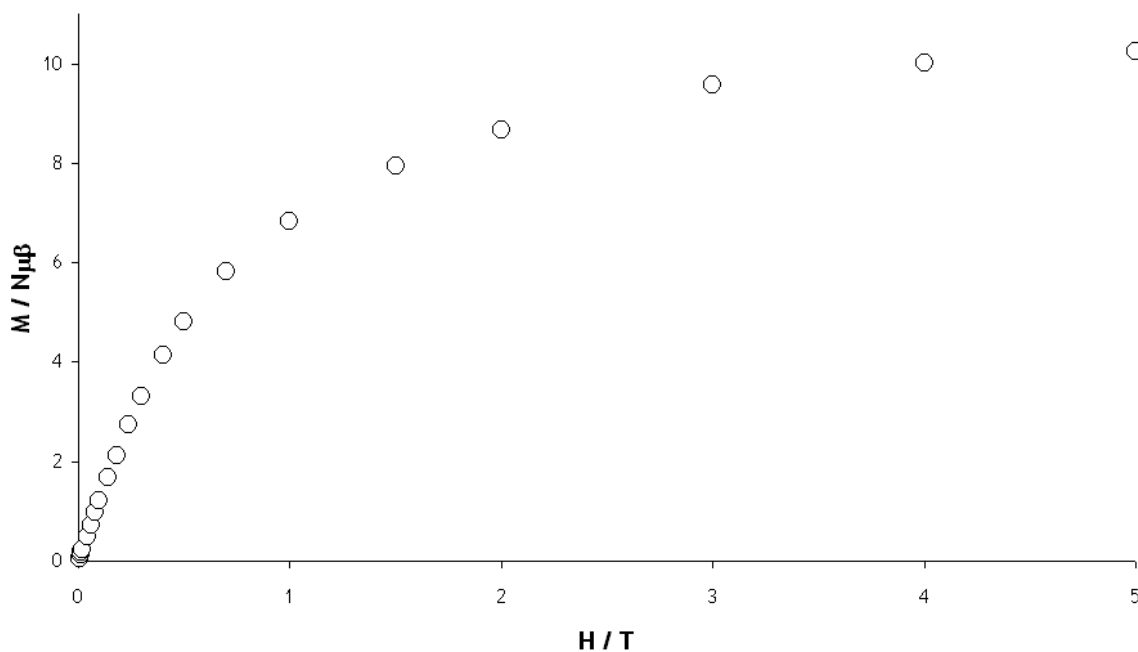


Figure 2.13: Magnetisation versus field at 2K for **2**.

Both the low temperature maximum in χT and the magnetization data are consistent with a spin ground state of $S = 5$ for **2**. However, further measurements including EPR are required to determine the magnitude and size of any anisotropy.

2.3.3 Discussion of crystal structure of $[\text{Fe}_6\text{O}_2(\text{HL}^1)_2(\text{Phbenz})_8]\cdot\text{MeCN}$ (**3**·MeCN)

A change of carboxylate in the triangle starting material results in the synthesis of complex **3**, a hexanuclear Fe(III) complex and crystallises in the space group $P\bar{1}$ (figure 2.14, where the atom suffix a signifies symmetry equivalent atoms).

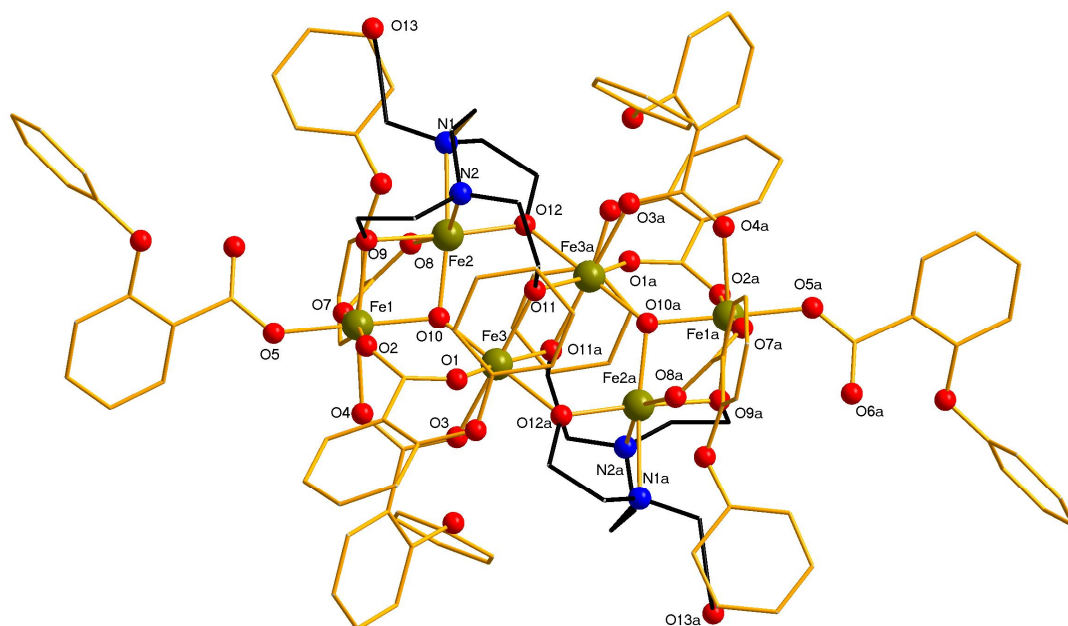


Figure 2.14: Structure of **3** (ball and stick representation with Fe(III) gold; O, red; N, blue; C, brown; H atoms are omitted for clarity)[atom suffix a signifies the symmetry equivalent atom: $a = 1 - x, 1 - y, 1 - z$]. Ligand bonds are highlighted in black.

Although complex **3**·MeCN crystallises in a different space group, the bulkier carboxylate group appears to have no effect on the final complex isolated from solution as it is homeo-structural with **2**, where the pivalate ligands have been replaced by 2-phenoxybenzoate ligands maintaining the core observed for **2**. The ligand also displays the same μ_4 binding mode as seen previously for **2**. There are small differences in the internal structure such as the Fe–O–Fe bridging angles given in table 2.11.

Varying the synthesis of both complex **2** and **3** by altering the ratios of starting materials and the addition of different bases had no overall effect on the reaction and continued to form complexes with this stable core in different reactions.

Table 2.9 Data for the crystal structure determination of **3**·MeCN

Empirical formula	C ₆₄ H ₁₂₆ N ₆ O ₂₉ Fe ₆
fw(gmol ⁻¹)	1778.82
Spacegroup	P-1
a(Å)	14.7691(9)
b(Å)	15.4530(9)
c(Å)	15.4736(9)
α(deg)	74.161(3)
β(deg)	75.397(3)
γ(deg)	64.336(3)
V(Å ³)	3025.5(3)
Z	1
T(K)	100(2)
λ(Å)	0.71073
ρ _{calcd} (Mg/m ³)	1.439
μ(mm ⁻¹)	0.784
R ₁ (%)	5.27
wR ₂ (%)	10.95
Goodness of fit indicator	0.9594

[†]Estimated standard deviations in the least significant figure are given in parentheses.

$${}^a R_1 = \frac{\sum ||F_o| - |F_c||}{\sum |F_o|}$$

$${}^b wR_2 = \left[\frac{\sum [w(F_o^2 - F_c^2)]}{\sum [w(F_o^2)]} \right]^{1/2}$$

$$\text{where } w = 1/[\sigma^2(F_o^2) + (0.2P)^2] \text{ and } P = [F_o^2 + 2F_c^2]/3$$

Table 2.10 Selected ligand bond distance for **3**·MeCN

Bond	Distance (Å) [†]	Bonds	Distance (Å) [†]
Fe2–N1	2.225(4)	Fe1–O10	1.912(3)
Fe2–N2	2.258(4)	Fe3–O10	1.865(3)
Fe2–O9	2.044(3)	Fe3–O11	2.013(4)
Fe2–O10	1.920(3)	Fe3a–O11	2.015(3)
Fe2–O12	1.964(3)	Fe3–O12	2.002(3)
Fe1–O9	2.001(4)		

[†] Estimated standard deviations in the least significant figure are given in parentheses.

Table 2.11 Selected bond angles for **3**·MeCN

Atoms	Angle (°) [†]	Atoms	Angle (°) [†]
Fe1—O10—Fe2	101.5(15)	Fe3—O11—Fe3a	101.7(15)
Fe1—O10—Fe3	126.3(17)	Fe2—O9—Fe1	94.5(14)
Fe2—O10—Fe3	121.8(18)	Fe2—O12—Fe3a	118.1(15)

[†] Estimated standard deviations in the least significant figure are given in parentheses.

Table 2.12 Bond valence sums for the inorganic oxygen atoms in **3**·MeCN

Atom	BVS	Assignment
O10	1.94	O ²⁻

* The oxygen atom is an O²⁻ if the BVS is ~2, an OH⁻ if the BVS is ~1, and an H₂O if the BVS is ~0.²²

2.3.3.1 Magnetic Susceptibility Measurements for **3**·MeCN

Magnetic susceptibility measurements were carried out on an air-dried sample. For **3** the value of χT at 300K is 9.46 cm³ mol⁻¹ K, significantly lower than for six uncoupled Fe(III) ions (26.25 cm³ mol⁻¹ K for $g=2$), indicating strong antiferromagnetic interactions between the Fe(III) centres (figure 2.15).

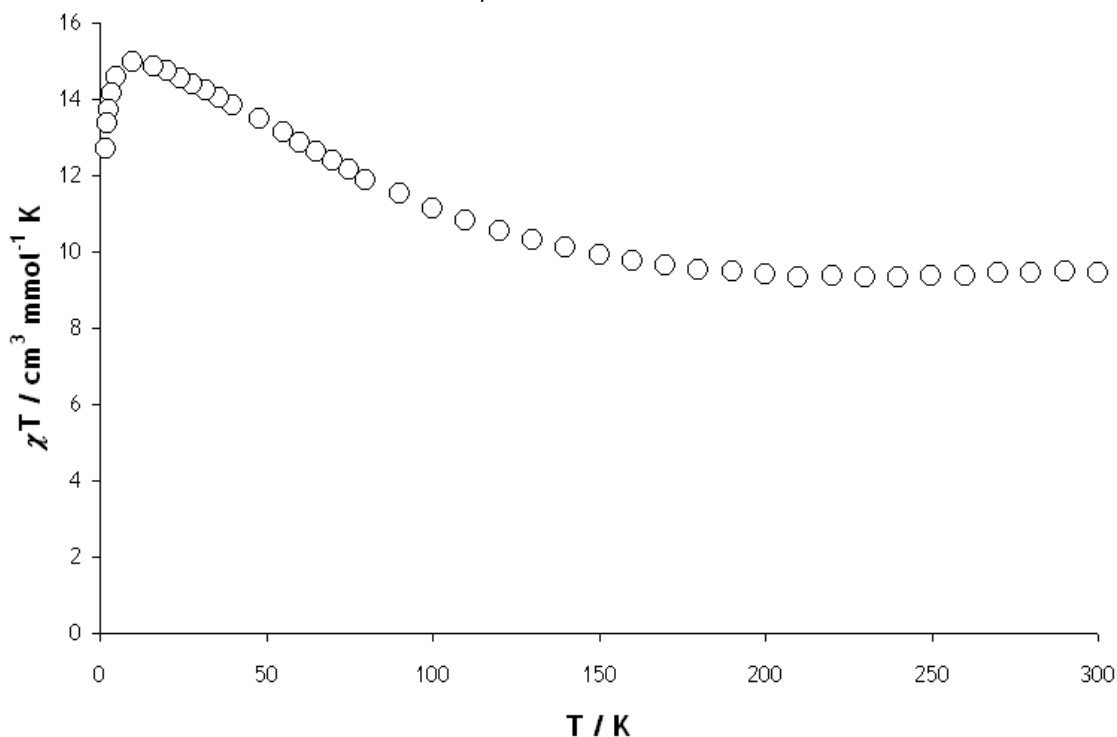


Figure 2.15: Temperature dependence of χT for **3** from 300-1.8 K measured in a field of 1 kOe

The value of χT increases steadily to a maximum of $15.0 \text{ cm}^3 \text{ mol}^{-1} \text{ K}$ at 10.0 K, then drops sharply to $12.7 \text{ cm}^3 \text{ mol}^{-1} \text{ K}$ at 1.8 K. This drop can be attributed to either zero-field splitting or intermolecular antiferromagnetic interactions. The magnetisation was measured as a function of applied field at 2 K, the curve does not reach saturation, rising to a maximum value of $M/N\beta=9.56$ at 5 T (figure 2.16).

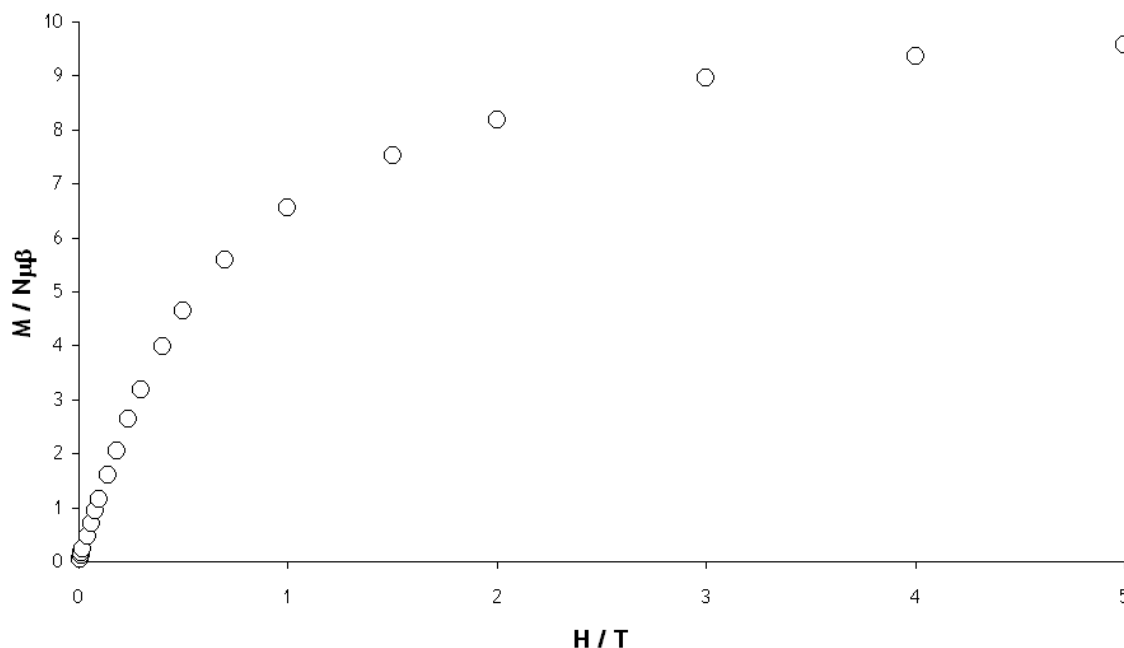


Figure 2.16: magnetisation versus field at 2K for **3**

Both the low temperature maximum in χT and the magnetization data are consistent with a spin ground state of $S = 5$ for **3**. Again, further measurements including EPR are required to determine the magnitude and size of any anisotropy.

We have attempted to rationalise the $S = 5$ ground state for both **2** and **3**. In both **2** and **3** the five different exchange pathways between Fe1/Fe2, Fe2/Fe3, Fe1/Fe3, Fe2/Fe3a and Fe3/Fe3a. Assuming the shortest Fe–O bond distances and largest Fe–O–Fe angles lead to the strongest exchange values,^{31,32} the exchange between Fe1/Fe3 and Fe2/Fe3 (through O5 and O10 for **2** and **3**) would lead to the strongest interactions in the cluster. The exchange between Fe2/Fe3a (through O3 or O12 for **2** and **3**) would be slightly weaker due to the slightly longer Fe–O pathway. Finally the exchange between Fe1/Fe2 and Fe3/Fe3a (via O2/O5, O1/O1a for **2** and O9/O10, O11/O11a for **3**) are similar to the previous exchanges with respect to bond length, however the Fe–O–Fe angles are much smaller (94.5-101.5) which would result in the weakest exchange within the cluster. Therefore the $S = 5$ ground state results from the two weakest exchange interactions being overcome by the stronger interactions and forced to align parallel to each other (figure 2.17).

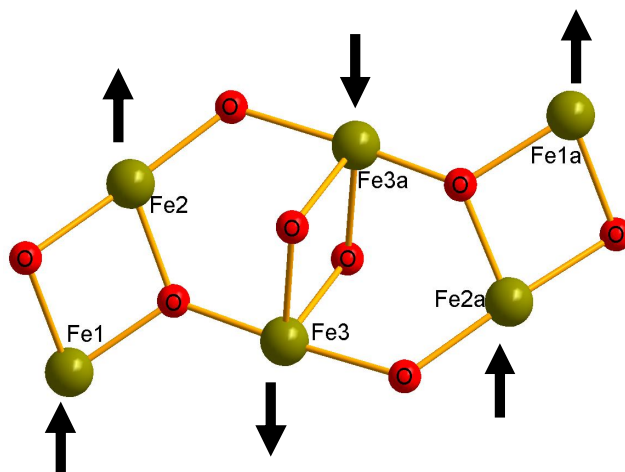


Figure 2.17: Possible spin alignment of six Fe(III) centres of **2** and **3** to rationalise the $S = 5$ ground state using simple magneto-structural correlations.

Fe1/Fe3 and Fe2/Fe3 are the stronger pairings and are aligned anti-parallel to each other. Although the weaker exchanges should align the spin of the pairings Fe1/Fe2 and Fe3/Fe3a anti-parallel, they are overcome by the stronger interactions and are forced to align parallel with each other.

2.3.4 Discussion of crystal structure of $[\text{Fe}_2^{\text{II}}\text{Fe}^{\text{III}}(\text{H}_2\text{L}^1)_2(\text{OBz})_2][\text{OBz}] \cdot \text{MeCN}$ (**4**·MeCN)

The use of a mixed valence triangle led to the synthesis of complex **4**, which crystallises in the monoclinic space group $P2_1/n$ (figure 2.18)

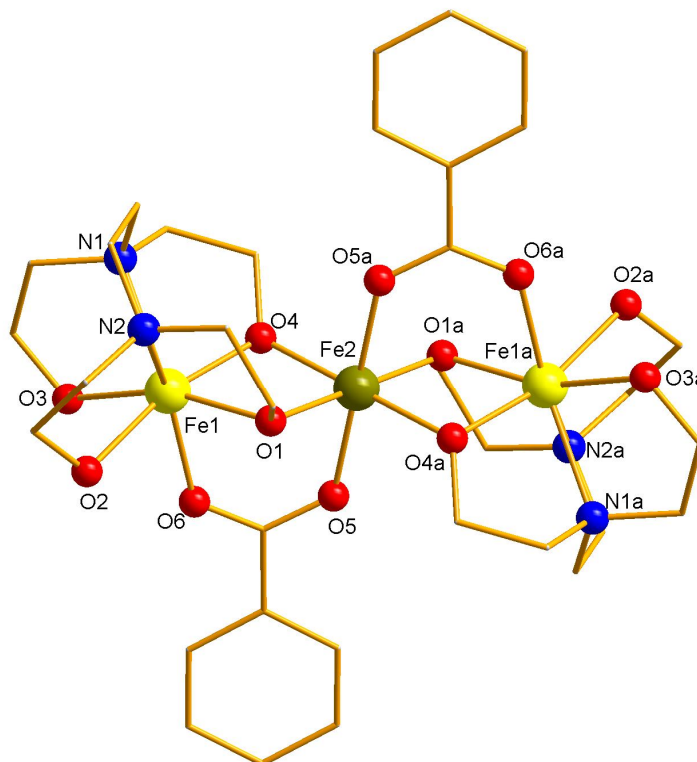


Figure 2.18: Structure of the cation of compound **4**, (ball and stick representation with Fe(III) gold; Fe(II) yellow; O, red; N, blue; C, brown; H atoms are omitted for clarity)[atom suffix a signifies the symmetry equivalent atom: $a = 1 - x, 1 - y, 1 - z$].

Complex **4** can be described as a linear arrangement of three Fe centres, the outer two being Fe(II) and the inner centre being Fe(III). The central Fe(III) is six coordinate and displays an octahedral geometry. It is bound by four oxygen donors from the ligand $\text{CH}_2\text{CH}_2\text{O}^-$ arms (O1, O4, O1a, O4a) and a further two from acetate ligands (O5, O5a). The outer Fe(II) atoms are seven coordinate and display a monocapped trigonal-prismatic geometry: the trigonal prism is formed from a $\{\text{N}_2\text{O}_4\}$ ligand donor set, with the cap from a binding benzoate oxygen atom (O6). The ligand is present in one binding mode, the two $\text{CH}_2\text{CH}_2\text{O}^-$ arms (O4, O1) μ_2 -bridging between Fe1 and Fe2. The two ligand alkoxide arms that remain protonated are bound to Fe1 (O2, O3). Both arms are hydrogen bonded to benzoate anions ($\text{O2} \cdots \text{O8}$ and $\text{O3} \cdots \text{O7}$) in the lattice (figure 2.19).

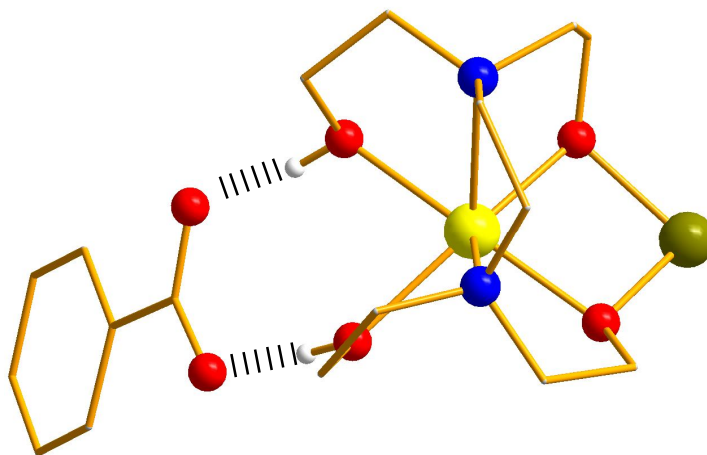


Figure 2.19: ligand binding mode of H_2L^1 present in **4**, showing protonated ligand arms and hydrogen bonding to a lattice benzoate anion.

Two complexes of iron are known in literature to have the same trimeric core as **4**, $[Fe_3(acac)(N-PhO-sal)_4]^{33}$ and $[Fe_3(Salpn)_2(O_2CCH_3)_2] \cdot 2DMF^{34}$ (where N-PhO-sal denotes N-2-hydroxyphenyl-salicylideneamine and salpn denotes N,N'-bis(salicylidene)propylenediamine). The former has all Fe(III) centres displaying six-coordinate octahedral geometry, with the core of the complex being non linear due to the environment of the central Fe(III) ion.³³ The latter displays the same linear configuration as **4**, however all centres are Fe(II) and display the same six-coordinate octahedral geometry. There are other examples of similar trimeric species³⁵ including a mixed valent trimeric cobalt complex.³⁶ Therefore, complex **4** is the first example of a trimeric mixed valence Fe(II)/Fe(III) complex which displays two seven coordinate Fe centres.

Table 2.13 Data for the crystal structure determination of **4**·MeCN

Empirical formula	C ₄₅ H ₆₃ N ₆ O ₁₄ Fe ₃
fw(gmol ⁻¹)	1079.58
Spacegroup	<i>P</i> 2 ₁ / <i>n</i>
<i>a</i> (Å)	7.9638(3)
<i>b</i> (Å)	14.4288(6)
<i>c</i> (Å)	23.4610(9)
β(deg)	94.545(2)
<i>V</i> (Å ³)	2687.38(18)
<i>Z</i>	1
<i>T</i> (K)	100(2)
λ(Å)	0.71073
ρ _{calcd} (Mg/m ³)	1.486
μ(mm ⁻¹)	0.874
<i>R</i> ₁ (%)	4.12
<i>wR</i> ₂ (%)	9.69
Goodness of fit indicator	0.9655

[†]Estimated standard deviations in the least significant figure are given in parentheses.

$$^a R_1 = \frac{\sum ||F_o| - |F_c||}{\sum |F_o|}$$

$$^b wR_2 = [\frac{\sum [w(F_o^2 - F_c^2)_2]}{\sum [w(F_o^2)_2]}]^{1/2}$$

$$\text{where } w = 1/[\sigma^2(F_o^2) + (0.2P)^2] \text{ and } P = [F_o^2 + 2F_c^2]/3$$

Table 2.14 Selected ligand bond distance for 4·MeCN

Bond	Distance (Å) [†]	Bond	Distance (Å) [†]
Fe1—O1	2.054(17)	Fe1—O6	2.121(18)
Fe1—O2	2.142(18)	Fe2—O4	1.988(17)
Fe1—O3	2.163(19)	Fe2—O5	2.054(17)
Fe1—O4	2.077(18)	Fe3a—O11	2.015(3)
Fe1—N1	2.312(2)	Fe3—O12	2.002(3)
Fe1—N2	2.419(2)		

[†]Estimated standard deviations in the least significant figure are given in parentheses.

Table 2.15 Selected bond angles for 4·MeCN

Atoms	Angle (°) [†]
Fe1—Fe2—Fe1a	180.0(0)
Fe1—O10—Fe2	98.50(7)
Fe2—O10—Fe3	97.39(18)

[†] Estimated standard deviations in the least significant figure are given in parentheses.

Table 2.16 Bond valence sums for the iron atoms in 4·MeCN

Atom	BVS	Assignment
Fe1	1.99	Fe ²⁺
Fe2	3.08	Fe ³⁺

2.3.4.1 Magnetic Susceptibility Measurements for 4·MeCN

Magnetic susceptibility measurements were carried out on an air-dried sample. The value of χT at 300K is 8.80 cm³ mol⁻¹ K, slightly lower than expected for two uncoupled Fe(II) ions and one uncoupled Fe(III) (10.37 cm³ mol⁻¹ K for $g=2$), indicating the presence of antiferromagnetic interactions between the Fe centres (figure 2.20).

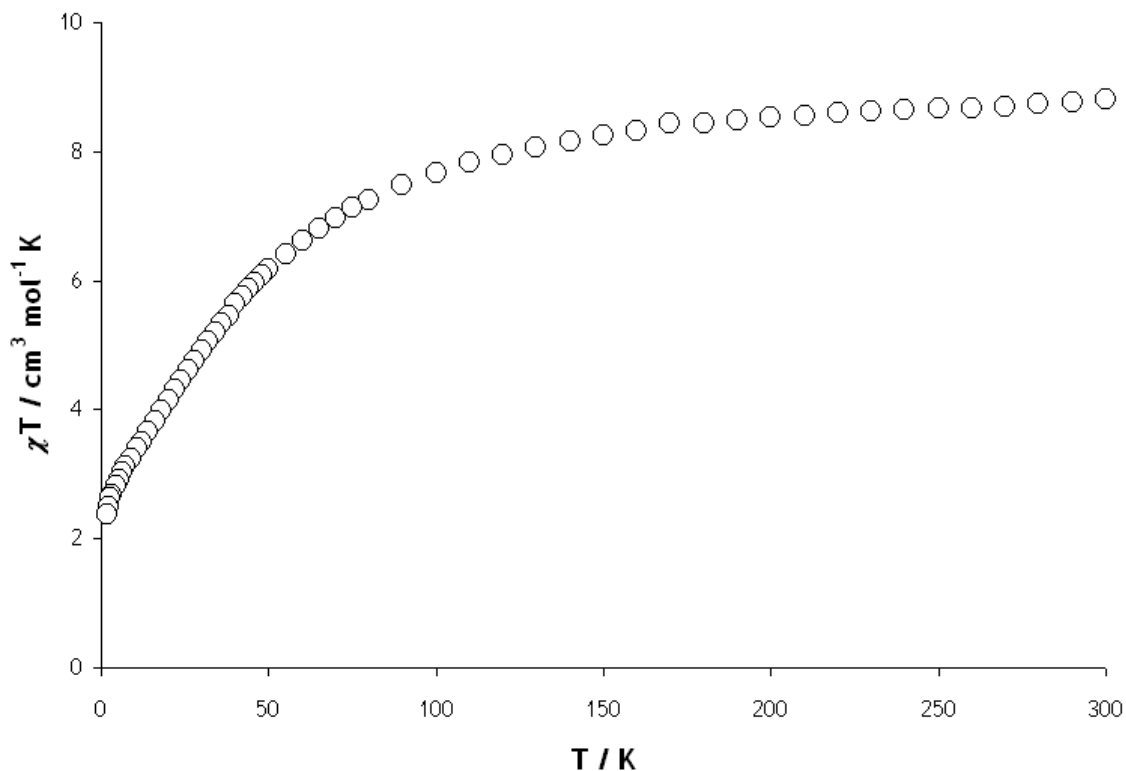


Figure 2.20: Temperature dependence of χT for **4** from 300-1.8 K measured in a field of 1 kOe

The value of χT decreases steadily to a $7.48 \text{ cm}^3 \text{mol}^{-1} \text{K}$ at 90.0 K, then drops sharply to $2.37 \text{ cm}^3 \text{mol}^{-1} \text{K}$ at 1.7 K. This drop can be attributed to intramolecular antiferromagnetic interactions. The magnetisation was measured as a function of applied field at 2 K, rising to a maximum value of $M/N\beta=3.05$ at 5 T (figure 2.21).

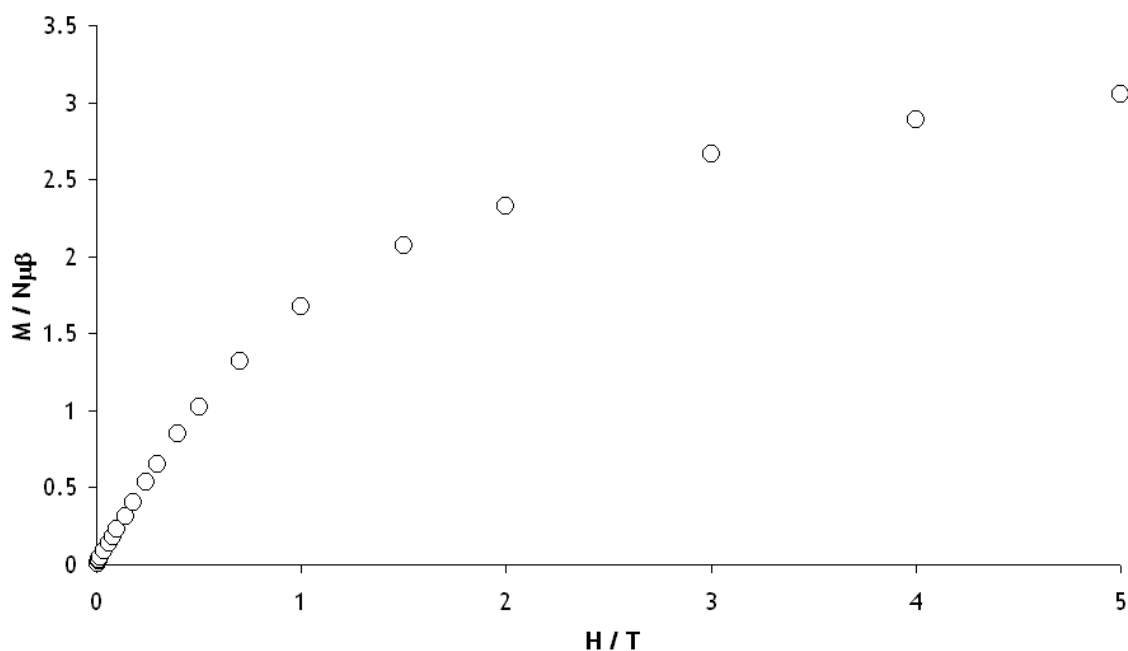


Figure 2.21: magnetisation versus field at 2K.

Both the low temperature minimum in χT and the magnetization data are consistent with a spin ground state of $S = 3/2$ for **4** which is consistent with the antiferromagnetic alignment of two spin up Fe(II) ions with one spin down Fe(III) ion. However, the magnetisation curve still appears to be rising. In order to try to determine the spin ground state and g value for **4**, magnetization data were collected in the ranges 5-50 kG and 2-7 K. However, no fit of the data was possible using the program MAGMOFIT,³⁷ suggesting that the complex does not have a well isolated spin ground state. Further measurements including EPR are required to determine the magnitude and size of any anisotropy.

2.3.5 Discussion of crystal structure of $[\text{Fe}_2(\text{H}_2\text{L}^{1a})_2]\cdot\text{MeCN}$ (**5**·MeCN)

The use of a mixed valance triangle led to the synthesis of complex **5** which crystallises in the monoclinic space group $P2_1/n$ (figure 2.22, where the atom suffix a signifies symmetry equivalents).

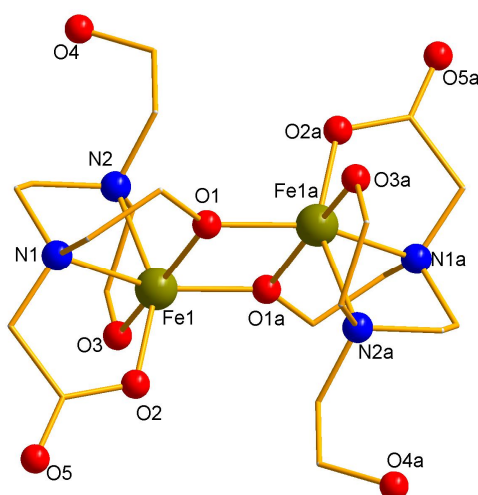


Figure 2.22: Structure of **5** (ball and stick representation with Fe(III) gold; O, red; N, blue; C, brown; H atoms are omitted for clarity)[atom suffix a signifies the symmetry equivalent atom: a = 1 _ x, 1 _ y, 1 _ z].

The dimer is composed of two $\{\text{Fe}(\text{HL}^{1a})\}$ units about an inversion centre between (Fe1, O1, Fe1a, O1a). The two Fe(III) centres are six coordinate displaying a distorted octahedral geometry and are bridged by a deprotonated $\text{CH}_2\text{CH}_2\text{O}^-$ arm of each ligand (O1, O1a). Each ligand binds five of the six coordination sites of the Fe(III) centre (O1, O2, O3, N1, N2) and the final site is bound by O1a from the second ligand present in the dimer. Fe dimers are not uncommon,^{38,39} the closest example to ours being $[\text{Fe}(\text{heidi})(\text{H}_2\text{O})_2]_2$ (were heidi is $\text{N}(\text{CH}_2\text{COOH})_2(\text{CH}_2\text{CH}_2\text{OH})$) by Powell *et al.*⁴⁰ There are two observations for this complex, the first being the complete breakdown of the oxo-centered starting material. The second and more interesting is the oxidation of one of the ligand arms (O5, O5a) to give a carboxylate group (figure 2.23).

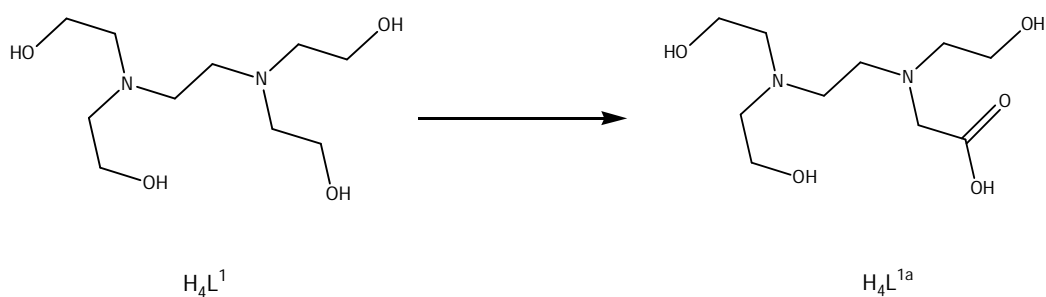
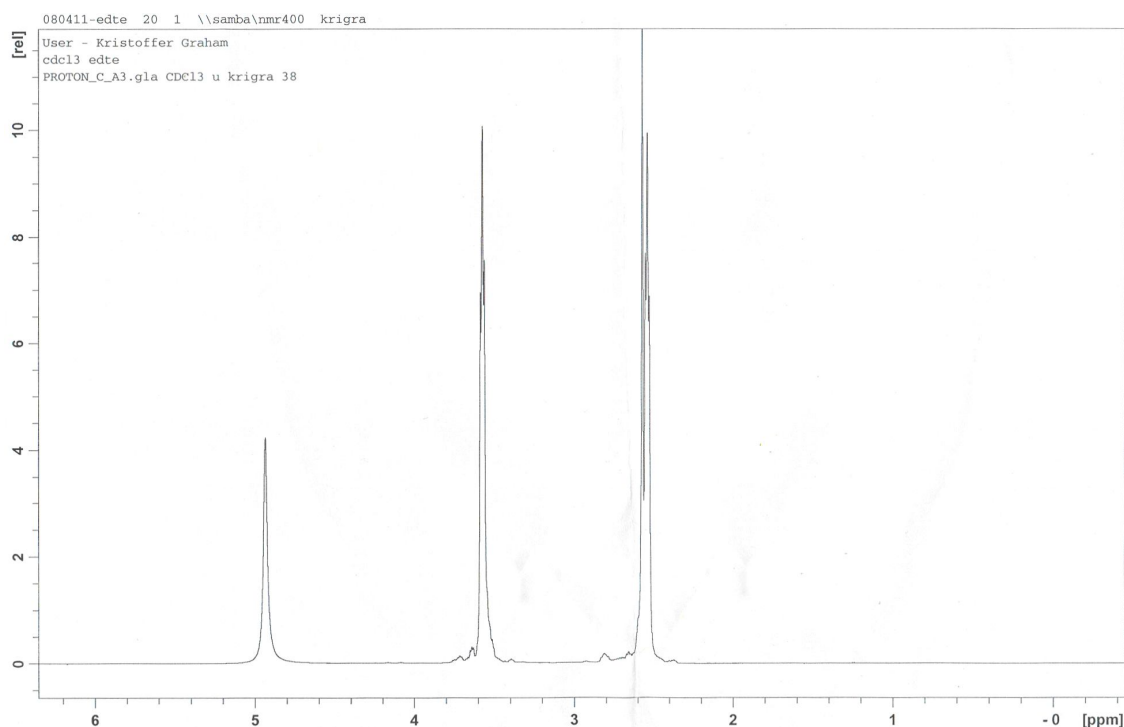


Figure 2.23: The ligands H_4L^1 to H_4L^{1a}

To check that the ligand had not oxidised after exposure to air 1H NMR (figure 2.24), was used to analyse and distinguish between any changes in functional groups i.e if the ligand had oxidised the carboxylate group would appear around 14ppm.

**Figure 2.24** 1H Nmr spectra of H_4L^1

The analysed data for the 1H NMR spectrum of H_4L^1 is as follows:

δ_H (400 MHz, $CDCl_3$) 2.54 ppm (8H, t, J 4.6 Hz, 4 x CH_2OH), 2.57 ppm (4H, s, $N(CH_2)_2N$), 3.57 ppm (8H, t, J 4.6 Hz, 4 x CH_2CH_2OH) and 4.94 ppm (4H, br s, 4 x OH).

The 1H NMR confirmed no oxidation of the ligand occurs on the bench meaning it occurs in the reaction. There are no known examples of this occurring with this edte and the cause remains unclear. Reactions such as Swern and Jones are used in organic synthesis when oxidising a primary alcohol to a carboxylic acid.^{41,42} Iron(III) is also used in catalytic processes to oxidise alcohol to aldehydes and ketones.^{43,44} In this process iron(III) is reduced to iron(II) during the oxidation process of the

alcohol. From the literature, it is possible to assume the iron(III) could oxidise our ligand to an aldehyde although it does not explain the formation of the carboxylate. The mechanism for this oxidation is unknown, therefore we can only assume that iron(III) together with a strong base can oxidise the ligand which is common in Mn chemistry.

Table 2.17 Data for the crystal structure determination of 5·MeCN

Empirical formula	C ₂₂ H ₄₂ N ₄ O ₈ Fe ₂
fw(gmol ⁻¹)	602.30
Spacegroup	<i>P</i> 2 ₁ / <i>n</i>
<i>a</i> (Å)	11.2267(4)
<i>b</i> (Å)	7.9879(3)
<i>c</i> (Å)	13.9169(5)
β(deg)	103.0490(10)
<i>V</i> (Å ³)	1215.81(8)
<i>Z</i>	1
<i>T</i> (K)	100(2)
λ(Å)	0.71073
ρ _{calcd} (Mg/m ³)	1.656
μ(mm ⁻¹)	1.256
R ₁ (%)	4.21
wR ₂ (%)	11.52
Goodness of fit indicator	0.8279

[†]Estimated standard deviations in the least significant figure are given in parentheses.

$${}^a R_1 = \frac{\sum ||F_o| - |F_c||}{\sum |F_o|}$$

$${}^b wR_2 = [\frac{\sum [w(F_o^2 - F_c^2)]}{\sum [w(F_o^2)]}]^{1/2}$$

$$\text{where } w = 1/[\sigma^2(F_o^2) + (0.2P)^2] \text{ and } P = [F_o^2 + 2F_c^2]/3$$

Table 2.18 Selected ligand bond distance for **5**·MeCN

Bond	Distance (Å) [†]	Bond	Distance (Å) [†]
Fe1–N1	2.208(17)	Fe1–O2	1.957(15)
Fe1–N2	2.235(16)	Fe1–O3	1.918(14)
Fe1–O1	2.050(14)	Fe1a–O1	1.957(14)

[†] Estimated standard deviations in the least significant figure are given in parentheses.

Table 2.19 Selected bond angles for **5**·MeCN

Atoms	Angle (°) [†]
Fe1–O1–Fe1a	107.7(6)

[†] Estimated standard deviations in the least significant figure are given in parentheses.

Table 2.20 Bond valence sums for the iron atoms in **5**·MeCN

Atom	BVS	Assignment
Fe1 , Fe1a	2.939486	Fe ³⁺

2.3.5.1 Magnetic Susceptibility Measurements for **5**·MeCN

Magnetic susceptibility measurements were carried out on an air-dried sample. The χT value at 300K is 4.90 cm³ mol⁻¹ K smaller than expected for two uncoupled Fe(III) ions (8.75 cm³ mol⁻¹ K for $g=2$) indicating the presence of strong antiferromagnetic interactions within the cluster. χT decreases steadily to a value of 0.07 cm³ mol⁻¹ K at 1.8K (figure 2.24). The χT data was fitted using MAGMUN down to 1.8 K using a 1J model (figure 2.25).⁴⁵ The best fit gave a spin ground state of $S = 0$, with $g = 2$, $J_1 = -16$ cm⁻¹, which is in agreement with the calculated values from the high temperature χT data.

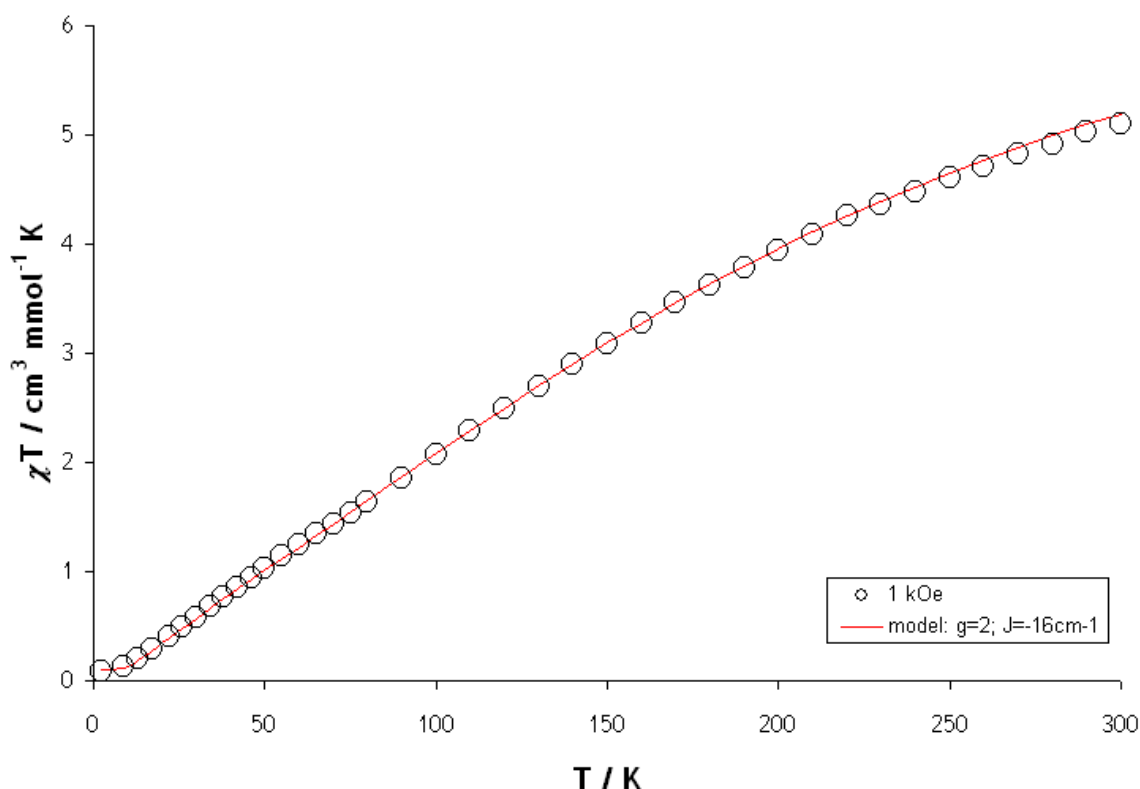


Figure 2.24: Temperature dependence of χT for **5** from 300-1.8 K measured in a field of 1 kOe. Red line indicates model of χT data vs T

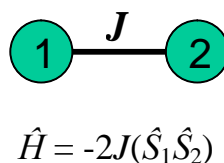


Figure 2.25: Representation of 1J model for **5**

2.4 Conclusions

A total of five new polynuclear iron complexes have been synthesised using H_4L^1 which contain six and seven coordinate iron centres. These clusters have illustrated the excellent bonding potential of H_4L^1 and its functionality as a bridging ligand as seen for complexes **2**, **3**, **4**, and **5** and or a capping ligand as seen for complex **1** depending on the level of deprotonation. The clusters synthesised along with the work of Bagai²¹ have added to an already growing family of Fe_2 , Fe_3 , Fe_6 and Fe_{12}

clusters. Of these the core of Fe₆ and Fe₁₂ complexes have never been observed in iron(III) chemistry. Complex **4** represents only the third example of a trimeric iron complex and the first trimeric mixed valence iron complex to be observed with this ligand. We have also illustrated the effect of the counter ion in the synthesis of complex **1** resulting in altering the crystal packing from *C2/c* to *F-43c*. A total of three of the five complexes synthesised have non-zero ground states ranging from 3/2 to 5, which we have attempted to rationalise.

2.5 Future work

H₄L¹ has been investigated extensively in both iron and manganese chemistry resulting in the synthesis of many clusters.^{20,21} Further investigation is needed into complex **1** and its potential use in gas absorption. EPR is needed to determine any anisotropy of complexes **2**, **3** and **4**. We have seen that a change of metal ion from manganese to iron can produce clusters with the same structural motif therefore it may be possible to use this synthetic approach to produce analogues of **1** using other metal ions such as Cr(III) or perhaps using mixed valence mixed metal triangles to synthesis new clusters. The use of Cr(III) as the metal ion would be more difficult due it being generally unreactive at room temperature. Therefore we would need to employ solvothermal techniques,⁴⁶ which would change the reaction conditions entirely.

2.6 References

- ¹ C. Delfs, D. Gatteschi, L. Pardi, R. Sessoli, K. Wieghardt, D. Hanke; *Inorg. Chem.* **1993**, 32, 3099.
- ² L. F. Jones, A. Batsanov, E. K. Brechin, D. Collison, M. Helliwell, T. Mallah, E. J. L. McInnes, S. Piligkos; *Angew. Chem. Int. Ed.* **2002**, 41, 4318.
- ³ S. Koizumi, M. Nihei, M. Nakano, H. Oshio; *Inorg. Chem.* **2005**, 44, 1208.
- ⁴ J. K. McKlusker, J. B. Vincent, E. A. Schmitt, M. L. Mino, K. Shin, D. K. Coggin, P. M. Hagen, J. C. Huffan, G. Christou, D. N. Hendrickson; *J. Am. Chem. Soc.* **1991**, 113, 3012.
- ⁵ O. Kahn; *Chem. Phys. Lett.* **1997**, 109.
- ⁶ C. Vilalta, T. A. O'Brien, E. K. Brechin, M. Pink, E. R. Davidson, G. Christou; *Inorg. Chem.* **2004**, 43, 5505.
- ⁷ D. M. Low, L. F. Jones, A. Bell, E. K. Brechin, T. Mallah, E. Rivière, S. J. Teat, E. J. L. McInnes; *Angew. Chem. Int. Ed.* **2003**, 42, 3781–3784.
- ⁸ A. L. Barra, A. Caneschi, A. Cornia, F. Fabrizi de Biani, D. Gatteschi, C. Sangregorio, R. Sessoli, L. Sorace; *J. Am. Chem. Soc.* **1999**, 121, 5302.
- ⁹ A. K. Boudalis, Y. Sanakis, J. Modesto, C. Juan, B. Donnadiou, V. Nastopoulos, A. Mari, Y. Coppel, J. P. Tuchagues, S. P. Perlepes; *Chem. Eur. J.* **2008**, 14, 2514.
- ¹⁰ L. F. Jones, E. K. Brechin, D. Collison, M. Helliwell, T. Mallah, S. Piligkos, G. Rajarman, W. Wernsdorfer; *Inorg. Chem.* **2003**, 42, 6601.
- ¹¹ J. C. Goodwin R. Sessoli, D. Gatteschi, W. Wernsdorfer, A. K. Powell, S.L. Heath *J. Chem. Soc. Dalton. Trans.* **2000**, 1835.
- ¹² W. Schmitt, C. E. Anson, W. Wernsdorfer, A. K. Powell; *Chem. Commun.* **2005**, 2098.
- ¹³ A. M. Ako, O. Waldmann, V. Mereacre, F. Klöwer, I. J. Hewitt, C. E. Anson, H. U. Güdel, A. K. Powell; *Inorg. Chem.* **2007**, 46, 756.
- ¹⁴ L. F. Jones, D. M. Low, M. Helliwell, J. Raftery, D. Collison, G. Aromí, J. Cano, T. Mallah, W. Wernsdorfer, E. K. Brechin, E. J.L. McInnes; *Polyhedron*, **2006**, 25, 325.
- ¹⁵ X. Solans, M. Font Altaba, J. Garcia-Oricain; *Acta. Cryst.* **1984**, C40, 635.
- ¹⁶ R. Meier, S. A. Bedell, G. Henkel; *Inorg. Chim. Acta.* **2002**, 337.
- ¹⁷(a) T. C. Stamatou, G. Christou, C. M. Jones, B. J. O'Callaghan, K. A. Abboud, T. A. O'Brien; *J. Am. Chem. Soc.* **2007**, 129, 9840 ;(b) A. A. H. Abu-Nuwwas, J. Cano; P. Christian, T. Mallah, G. Rajaraman, S. J. Teat, R. E. P. Winpenny, Y. Yukawa; *Chem. Commun.* **2004**, 314; (c) D. Sellman, F. Geipel, F. W. Heinemann; *Chem-Eur. J.* **2002**, 8, 958; (d) C. P. Raptopoulou, V. Tangoulis, E. Devlin; *Angew. Chem. Int. Ed.* **2002**, 41, 2386.
- ¹⁸ M. Murugesu, K. A. Abboud, G. Christou; *Polyhedron* **2004**, 23, 2779.
- ¹⁹ C. Boskovic, H. U. Güdel, G. Labat, A. Neels, W. Wernsdorfer, B. Moubaraki, K. S. Murray; *Inorg. Chem.* **2005**, 44, 318.
- ²⁰ A. Zhou, L. Qin, C. C. Beedle, S. Ding, M. Nakano, J. Leng, M. Tong, D. N. Hendrickson; *Inorg. Chem.* **2007**, 46, 8111.
- ²¹ R. Bagai, M. R. Daniels, K. A. Abboud, G. Christou; *Inorg. Chem.* **2008**, 47, 3318.

- ²² W. Liu, H. H. Thorp; *Inorg. Chem.* **1993**, 32, 4102.
- ²³ (a) C. A. Christmas, H. L. Tsai, L. Pardi, J. M. Kesselman, P. K. Gantzel, R. K. Chadha, D. Gatteschi, D. F. Harvey, D. N. Hendrickson; *J. Am. Chem. Soc.* **1993**, 115, 12483; (b) S. Yoon, S. J. Lippard; *J. Am. Chem. Soc.* **2005**, 127, 8386.
- ²⁴ (a) A. A. Smith, R. A. Coxall, A. Harrison, M. Helliwell, S. Parsons, R. E. P. Winpenny; *Polyhedron*. **2004**, 23, 1557. (b) P. S. Ammala, J. D. Cashion, C. M. Kepert, K. S. Murray, B. Moubaraki, L. Spiccia, B. O. West; *Dalton Trans.* **2001**, 2032. (c) R. Çelenligil-Çetin, R. J. Staples, P. Stavropoulos; *Inorg. Chem.* **2000**, 39, 5838.
- ²⁵ A. Cornia, D. Gatteschi, K. Hegetschweiler, L. Hausherr-Primo, V. Gramlich; *Inorg. Chem.* **1996**, 35, 15, 4414 and references therein
- ²⁶ (a) H. Burkill, N. Robertson, R. Vilar, A. J. P. White, D. J. Williams; *Inorg. Chem.* **2005**, 44, 9, 3337; (b) E. J. Seddon, J. C. Huffman, G. Christou; *J. Chem. Soc. Dalton Trans.* **2000**, 4446.
- ²⁷ (a) E. J. Seddon, J. Yoo, K. Folting, J. C. Huffman, D. N. Hendrickson G. Christou; *J. Chem. Soc. Dalton Trans.* **2000**, 3640; (b) W. Micklitz, S. J. Lippard; *J. Am. Chem. Soc.* **1988**, 27, 3067; (c) A. A. Smith, R. A. Coxall, A. Harrison, M. Helliwell, S. Parsons, R. E. P. Winpenny, *Polyhedron*. **2004**, 23, 1557.
- ²⁸ (a) S. Koizumi, M. Nihei, M. Nakano, H. Oshio, *Inorg. Chem.* **2005**, 44, 1208; (b) M. Murugesu, K. A. Abboud, G. Christou, *Dalton Trans.* **2003**, 4552; (c) R. W. Saalfrank, C. Deutscher, S. Sperner, T. Nakajima, A. M. Ako, E. Uller, F. Hampel, F. W. Heinemann, *Inorg. Chem.* **2004**, 43, 4372.
- ²⁹ C. A. Christmas, H. L. Tsai, L. Pardi, J. M. Kesselman, P. K. Gantzel, R. K. Chadha, D. Gatteschi, D. F. Harvey, D. N. Hendrickson, *J. Am. Chem. Soc.* **1993**, 115, 12483.
- ³⁰ C. P. Raptopoulou, A. K. Boudalis, Y. Sanakis, V. Psycharis, J. M. Clemente-Juan, M. Fardis, G. Diamantopoulos, G. Papavassiliou; *Inorg. Chem.* **2006**, 45, 2317.
- ³¹ (a) S. M. Gorun, S. J. Lippard, *Inorg. Chem.* **1991**, 30, 1625; (b) H. Weihe, H. U. Güdel, *J. Am. Chem. Soc.* **1997**, 119, 6539. (c) R. Werner, S. Ostrovsky, K. Griesar, W. Haase, *Inorg. Chim. Acta.* **2001**, 326, 78.
- ³² C. Vilalta, T. A. O'Brien, E. K. Brechin, M. Pink, E. R. Davidson, G. Christou; *Inorg. Chem.* **2004**, 43, 5505.
- ³³ T. Nakamura, E. Kuranuki, K. Niwa, M. Fujiwara, T. Matsushita; *Chem. Lett.* **2000**, 248.
- ³⁴ A. Gerli, K. S. Hagen, L. G. Marzilli; *Inorg. Chem.* **1991**, 30, 24, 4673.
- ³⁵ (a) J. A. Bonadies, M. L. Kirk, M. L. Soo, D. P. Kessissoglou, W. E. Hatfield, V. L. Pecoraro; *Inorg. Chem.* **1989**, 28, 2037 (b) C. Fukuhara, T. Kazuhiko, N. Matsumoto, S. Kida, M. Mikuriya, M. Masayasu; *J. Chem. Soc. Dalton Trans.* 1990, 3473.
- ³⁶ C. Fukuhara, E. Asato, T. Shimoji, K. Katsura, M. Mori, K. Matsumoto, S. Ooi, *J. Chem. Soc. Dalton Trans.* **1987**, 1305.
- ³⁷ Dr S. Piligkos, University of Copenhagen.
- ³⁸ D. M. Kurtz. JR; *Chem. Rev.* **1990**, 90, 585.
- ³⁹ S. Yoon, S. J. Lippard; *J. Am. Chem. Soc.* **2005**, 127, 23, 8386.

- ⁴⁰ A. K. Powell, S. L. Heath, D. Gatteschi, L. Pardi, R. Sessoli, G. Spina, F. Del Giallo, F. Pieralli; *J. Am. Chem. Soc.* **1995**, 117, 9, 2491.
- ⁴¹ K. Omura, D. Swern; *Tetrahedron*, **1978**, 34, 1651.
- ⁴² I. Heilbrone, R. H. Jones, F. Sondheimer; *J. Chem. Soc.*, **1953**, 457.
- ⁴³ M. J. Schultz, M. S. Sigman; *Tetrahedron*, **2006**, 62, 8227.
- ⁴⁴ S. S. Kim, I. Trushkov, S. K. Sar; *Bull. Korean Chem. Soc.* **2002**, 23, 9, 1331.
- ⁴⁵ Dr. L. K. Thompson; Memorial University, Newfoundland.
- ⁴⁶ R. H. Laye, E. J. L. McInnes; *Eur. J. Inorg. Chem.*, **2004**, 2811.

3. Synthesis of Iron complexes: Bicine

Following on from the success of edte with Fe(III), we turned our attention to bicine (H_3L^2). By maintaining the ligand backbone of edte, (the $\{N(CH_2CH_2OH)_2\}$ group) and altering the functional groups, we hoped this would produce new large polynuclear clusters with unique topologies. The only polynuclear Fe(III) complex known for this ligand is the star shaped Fe_6Bic_6 wheel¹ reported in 2003 (figure 3.1).

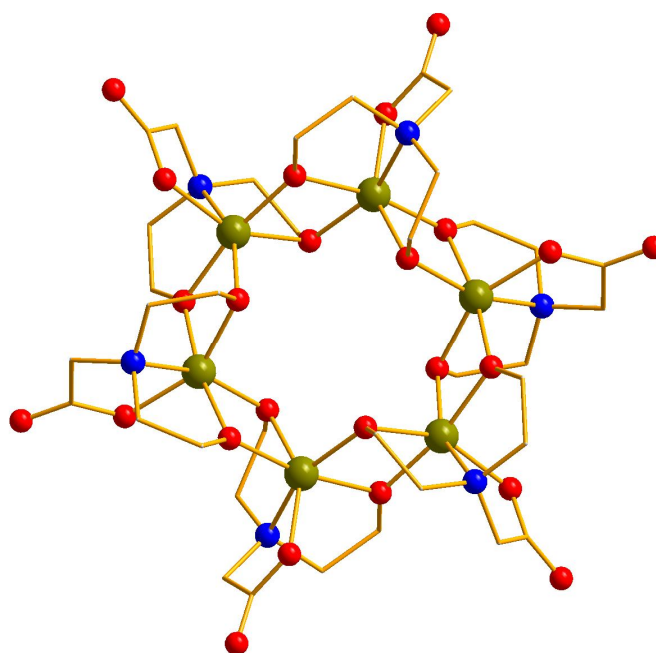


Figure 3.1: structure of Fe_6Bic_6 (ball and stick representation with Fe(III) gold; O, red; N, blue; C, brown; H atoms are omitted for clarity)

The cluster contains no carboxylate ligands in the final product although it was present in the reaction. Also it featured as a product in many of our reactions regardless of carboxylate, base and ratios, although it was only when other clusters were synthesised that this cluster remained in the final solution. We reacted this ligand in the same way to edte by using the pre-formed oxo-centred triangles, again altering the base and varying the ratios of reactants. We continued to focus on the same six triangles used for edte, as they were highly successful in producing some unique and interesting clusters. This approach has resulted in six new iron complexes being produced. The synthesis, structure and magnetic characterisation of these are reported below for bicine (H_3L^2).

3.1 Synthesis of complexes containing bicine H_3L^2

3.1.1 Synthesis of $[Et_2NH_2]_2[Fe_6O_2(OH)_2(L^2)_2(piv)_8] \cdot 2MeCN$ ($6 \cdot 2MeCN$)

To a stirred solution of $[Fe_3O(piv)_6(H_2O)_3][piv][Hpiv] \cdot EtOH \cdot 2H_2O$ (0.5 g, 0.44 mmol) in MeCN (20 ml), H_3L^2 (0.07 g, 0.44 mmol) was added, followed by Et_2NH (0.3 g, 0.44 mmol). The solution was stirred overnight then filtered to give a dark red solution and a small amount of precipitate. The filtrate was stored in a sealed vial. After 4 weeks small orange/brown crystals formed in the sealed solution and were collected in approximately 16 % yield. Selected IR data: $\nu = 2961, 1667, 1556, 1482, 1421, 1347, 1220, 1069, 905, 881, 787, 651 \text{ cm}^{-1}$. Air-dried crystals analyse as $6 \cdot 2MeCN \cdot 4H_2O$, analysis (%) calc. (found): C, 42.59 (42.38); H, 7.37 (7.04); N, 3.10 (3.36).

3.1.2 Synthesis of $[Fe_6O_2(OMe)_2(L^2)_2(phbenz)_4(MeOH)_6][NO_3]_2 \cdot MeOH$ ($7 \cdot MeOH$)

To a stirred solution of $[Fe_3O(phbenz)_6(MeOH)_3][NO_3] \cdot 3MeOH$ (0.5 g, 0.3 mmol) in MeCN (20 ml), H_3L^2 (0.05 g, 0.3 mmol) was added. The solution was stirred overnight then filtered to give an orange solution and a yellow precipitate. The filtrate was stored in a sealed vial and after 3 weeks brown crystals formed and were collected in 14 %. Selected IR data: $\nu = 1580, 1538, 1479, 1394, 1230, 1014, 881, 750, 695, 647 \text{ cm}^{-1}$. Air-dried crystals analyse as $7 \cdot MeOH \cdot 3H_2O$, analysis (%) calc. (found): C, 44.45 (44.10); H, 4.91 (4.65); N, 2.84 (2.98).

3.1.3 Synthesis of $[Et_2NH_2]_2[Fe_6O_2(OH)_2(L^2)_2(OAc)_8]$ (**8**)

To a stirred solution of $[Fe_2^{III}Fe^{II}O(OAc)_6(H_2O)_3]$ (0.5 g, 0.845 mmol) in MeCN (20 ml), H_3L^2 (0.14 g, 0.845 mmol) was added followed by Et_2NH (0.12 g, 1.69 mmol). The solution was stirred overnight then filtered to give a dark brown solution. The filtrate was stored in a sealed vial. Small portions of solution were taken and layered with Et_2O by vapour diffusion. After 4 weeks brown crystals were observed in vapour diffusion experiments and were collected in approximately 4 % yield.

Selected IR data: $\nu = 2868, 1551, 1417, 1048, 907, 642 \text{ cm}^{-1}$. Air-dried crystals analyse was not obtained for **(8)** due to a lack of sample.

3.1.4 Synthesis of $[\text{Fe}_{12}\text{O}_4(\text{L}^2)_4(\text{H}_1\text{L}^2)_4(\text{piv})_8] \cdot 5\text{MeCN}$ (**9**·5MeCN)

To a stirred solution of $[\text{Fe}_3\text{O}(\text{piv})_6(\text{H}_2\text{O})_3][\text{piv}][\text{Hpiv}] \cdot \text{EtOH} \cdot 2\text{H}_2\text{O}$ (0.5 g, 0.44 mmol) in MeCN (20 ml), H_3L^2 (0.07 g, 0.44 mmol) was added, followed by NaOMe (0.02 g, 0.44 mmol). The solution was stirred overnight then filtered to give a dark orange solution. The solution was filtered and stored in a sealed vial. After 4 weeks small brown crystals formed in the sealed solution and were collected in approximately 12 % yield. Selected IR data: $\nu = 3397$ (broad); 2962, 1624, 1533, 1484, 1422, 1358, 1227, 1080, 1040, 889, 795, 690 cm^{-1} . Air-dried crystals analyse as **9**·2MeCN·4H₂O, analysis (%) calc. (found): C, 37.05 (36.77); H, 5.75 (5.67); N, 4.70 (4.95).

3.1.5 Synthesis of $[\text{Fe}_2^{\text{III}}\text{Fe}_4^{\text{II}}\text{O}_2(\text{benz})_{10}(\text{MeCN})_4]$ (**10**)

To a stirred solution of $[\text{Fe}_2^{\text{III}}\text{Fe}^{\text{II}}\text{O}(\text{benz})_6(\text{H}_2\text{O})_2(\text{MeCN})]$ (0.5 g, 0.18 mmol) in MeCN (20 ml), H_4L^1 (0.03 g, 0.18 mmol) was added, followed by Et₂NH (0.01 g, 0.18 mmol). The solution was stirred overnight then filtered to give a dark orange solution. The solution was stored in a sealed vial with small portions of solution taken and layered with Et₂O by vapour diffusion. After 3 weeks small brown crystals formed in both the sealed solution and from vapour diffusion. Crystals from the sealed solution were collected in approximately 18 % yield. Selected IR data: $\nu = 1594, 1524, 1395, 1175, 1024, 712, 652 \text{ cm}^{-1}$. Air-dried crystals analyse as **10**, analysis (%) calc. (found): C, 53.77 (53.65); H, 3.59 (3.60); N, 3.22 (3.17).

3.1.6 Synthesis of $[\text{Et}_2\text{NH}_2][\text{Et}_2\text{NH}][\text{Fe}_6\text{O}_2(\text{OAc})_{15}(\text{HOAc})_2] \cdot 2\text{MeCN}$ (**11**·2MeCN)

To a stirred solution of $[\text{Fe}_2^{\text{III}}\text{Fe}^{\text{II}}\text{O}(\text{OAc})_6(\text{H}_2\text{O})_3]$ (0.5 g, 0.845 mmol) in MeCN (20 ml), H_3L^2 (0.03 g, 0.28 mmol) was added, followed by Et₂NH (0.08 g, 1.12 mmol). The solution was stirred overnight then filtered to give a dark brown solution. The solution was filtered and stored in a sealed vial. After 6 weeks small brown crystals formed in the sealed solution that were collected. Selected IR data: $\nu = 3371, 2876,$

1536, 1438, 1043, 889, 680 cm^{-1} . Air-dried crystal analysis was not obtained for **11** again due to a lack of sample.

3.2 Complexes containing Bicine (H_3L^2)

3.2.1 Discussion of crystal structure of $[\text{Et}_2\text{NH}_2]_2[\text{Fe}_6\text{O}_2(\text{OH})_2(\text{L}^2)_2(\text{piv})_8] \cdot 2\text{MeCN}$ (**6**·2MeCN)

Complex **6**·2MeCN contains two crystallographically independent dianionic hexanuclear Fe(III) complexes which crystallise in the triclinic space group $P-1$ (figure 3.2 where the atom suffix a signifies symmetry equivalents).

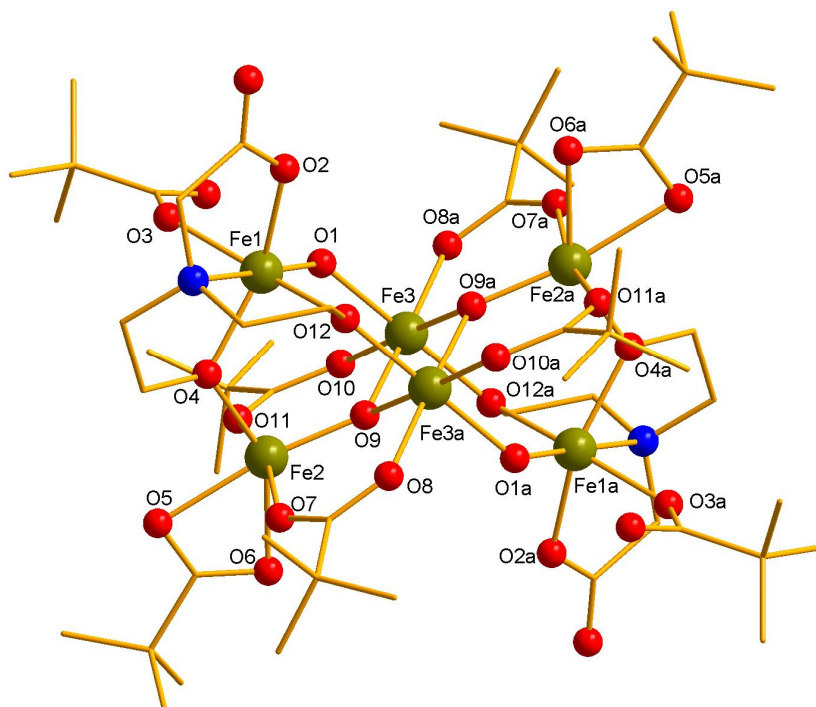


Figure 3.2: Structure of the anion of **6** (ball and stick representation with Fe(III), gold; O, red; N, blue; C, brown; H atoms are omitted for clarity)[atom suffix a signifies the symmetry equivalent atom: $a = 1 - x, 1 - y, 1 - z$].

The Fe_6 complex consists of an $\{\text{Fe}_4\text{O}_2\}$ butterfly unit (Fe2, Fe3, Fe2a, Fe3a), which is capped by two $\{\text{Fe}(\text{Bic})\}$ units that sit above and below the central $\{\text{Fe}_4\text{O}_2\}$ core (figure 3.3). The two bicine ligands are triply deprotonated binding to Fe1 (and

symmetry equivalent) through N1 and N1a. The carboxylate arm (O2) binds monodentate to Fe1, the two remaining $\text{CH}_2\text{CH}_2\text{O}^-$ arms bridge bidentate between Fe1 and the outer Fe2 ion at O4 and between Fe1–Fe3a at O2 (and symmetry equivalents). The coordination sphere of Fe1 is completed by O1, that is μ_2 -bridging between Fe1 and Fe3 and the terminal pivalate ligand (O3). The complex contains eight pivalate ligands, four of which bridge the central $\{\text{Fe}_4\text{O}_2\}$ 'butterfly' core in a 1,3 binding mode. Of the remaining pivalate ligands, two cap the outer Fe2 and Fe2a ions in a 1,1 mode and the final two bind monodentate to Fe1 and Fe1a and are hydrogen-bonded to the hydroxide ligands (O1 and O1a). The Et_2NH_2 cations are positioned above and below the Fe_6 cluster and are hydrogen bonded to the carboxylate of the bicine ligand at O2, O2a and to the capping pivalate ligands, O6 and O6a.

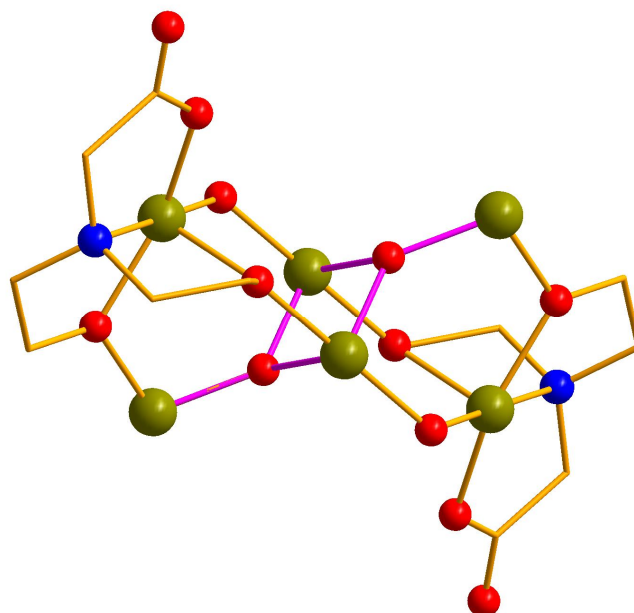


Figure 3.3: $\{\text{Fe}_4\text{O}_2\}$ butterfly core of the anion highlighted in purple with pivalate ligands removed. Bicine ligand binding mode is shown.

The $\{\text{Fe}_4\text{O}_2\}$ core of this cluster is not unusual in Fe(III) chemistry usually resulting in $S = 0$ ground states attributed to strong antiferromagnetic interactions between the wing tip Fe and the body Fe ions.² However there are two additional Fe centres in the anion of **6**, each coupled to the $\{\text{Fe}_4\text{O}_2\}$ core by three μ_2 -O atoms.

Table 3.1 Data for the crystal structure determination of **6**·2MeCN

Empirical formula	C ₆₄ H ₁₃₂ N ₄ O ₃₂ Fe ₆
fw(gmol ⁻¹)	1804.86
Spacegroup	<i>P</i> -1
<i>a</i> (Å)	11.9471(15)
<i>b</i> (Å)	14.6166(19)
<i>c</i> (Å)	26.363(3)
α (deg)	89.775(4)
β (deg)	88.835(4)
γ (deg)	66.725(4)
<i>V</i> (Å ³)	4228.0(9)
<i>Z</i>	2
<i>T</i> (K)	100(2)
λ (Å)	0.71073
ρ_{calcd} (Mg/m ³)	1.367
μ (mm ⁻¹)	1.077
<i>R</i> ₁ (%)	9.7
<i>wR</i> ₂ (%)	9.54
Goodness of fit indicator	1.0708

[†]Estimated standard deviations in the least significant figure are given in parentheses.

$$^a R_1 = \frac{\sum ||F_o| - |F_c||}{\sum |F_o|}$$

$$^b wR_2 = \left[\frac{\sum [w(F_o^2 - F_c^2)]}{\sum [w(F_o^2)]} \right]^{1/2}$$

$$\text{where } w = 1/[\sigma^2(F_o^2) + (0.2P)^2] \text{ and } P = [F_o^2 + 2F_c^2]/3$$

Table 3.2 Selected ligand bond distance for **6**·2MeCN

Bond	Distance (Å) [†]	Bond	Distance (Å) [†]
Fe1–N1	2.213(3)	Fe2–O9	1.834(2)
Fe1–O4	2.006(2)	Fe3–O1	1.998(13)
Fe1–O12	2.004(2)	Fe3–O9	1.965(19)
Fe1–O2	2.031(2)	Fe3a–O9	1.962(2)
Fe1–O1	1.903(2)	Fe3a–O2	2.010(2)
Fe1–O4	1.950(2)		

[†] Estimated standard deviations in the least significant figure are given in parentheses.

Bonds in red are for comparison with tables, 3.6 and 3.10.

Table 3.3 Selected bond angles for **6·2MeCN**

Atoms	Angle (°) [†]	Atoms	Angle (°) [†]
Fe1—O4—Fe2	116.1(3)	Fe2—O9—Fe3a	128.6(3)
Fe1—O12—Fe3a	123.9(4)	Fe2—O9—Fe3	127.4(4)
Fe1—O1—Fe3	128.4(3)	Fe3—O9—Fe3a	95.0(3)

[†] Estimated standard deviations in the least significant figure are given in parentheses.

Bond angle in red is for comparison with tables, 3.7 and 3.11.

Table 3.4 Bond valence sums for the inorganic oxygen atoms in **6·2MeCN**

Atom	BVS	Assignment
O1	1.86	O ²⁻
O9	0.94	OH ⁻

[†] The oxygen atom is an O²⁻ if the BVS is ~2, an OH⁻ if the BVS is ~1, and an H₂O if the BVS is ~0.³

3.2.1.1 Magnetic Susceptibility Measurements for **6·2MeCN**

Magnetic susceptibility measurements were carried out on an air-dried sample. For **6** the value of χT at 300K is 9.87 cm³ mol⁻¹ K, significantly lower than for six uncoupled Fe(III) ions (26.25 cm³ mol⁻¹ K for $g=2$), indicating strong antiferromagnetic interactions between the Fe(III) centres (figure 3.4).

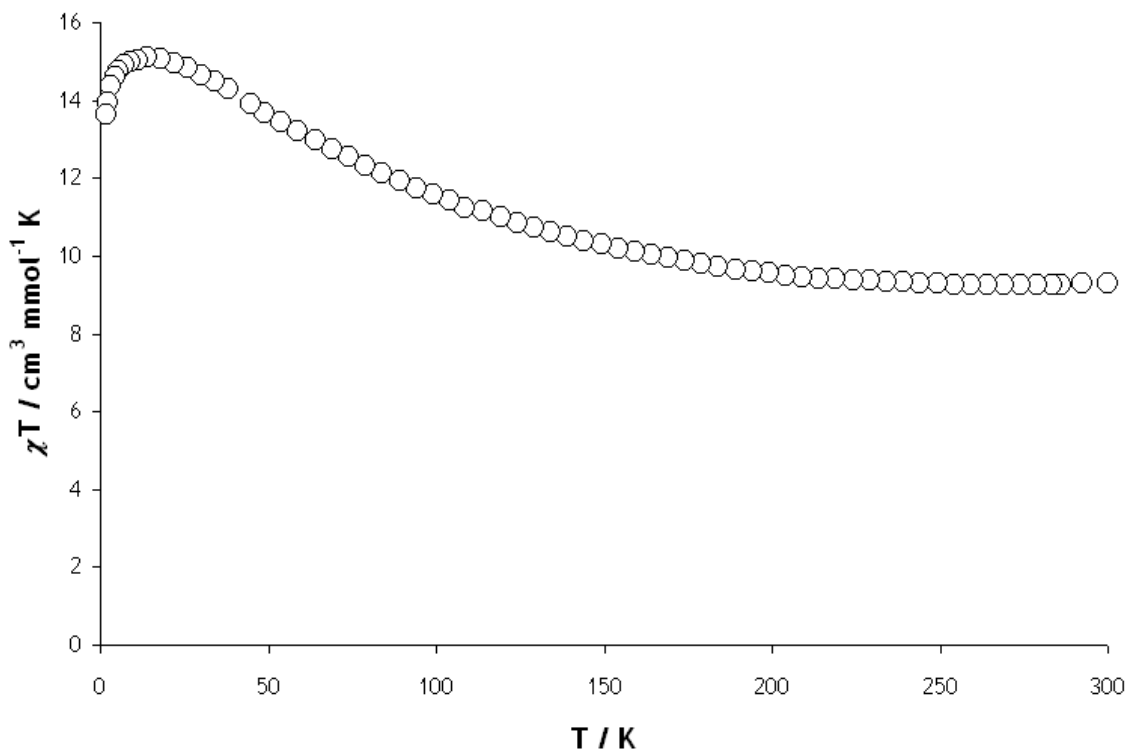


Figure 3.4: Temperature dependence of χT for **6** from 300-1.8 K measured in a field of 1 kOe

The value of χT increases steadily to a maximum of $15.0 \text{ cm}^3 \text{ mol}^{-1} \text{ K}$ at 14.0 K, then drops sharply to $13.6 \text{ cm}^3 \text{ mol}^{-1} \text{ K}$ at 1.8 K. This drop can be attributed to either zero-field splitting or intermolecular antiferromagnetic interactions. The magnetisation was measured as a function of applied field at 2 K, rising to a maximum value of $M/N\beta=10.0$ at 7 T (figure 3.5).

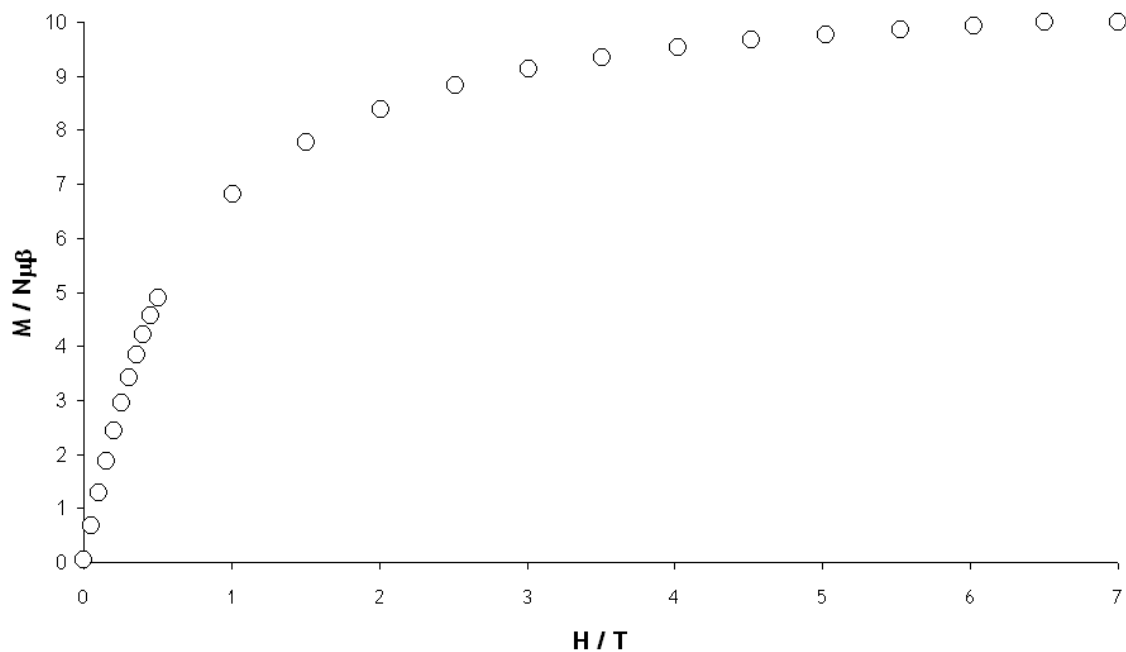


Figure 3.5: magnetisation versus field at 2K for **6**

Both the low temperature maximum in χT and the magnetization data are consistent with a spin ground state of $S = 5$ for **6**. However, EPR measurements are required to determine the magnitude and size of any anisotropy. The most logical explanation of an $S = 5$ ground state for this type of complex would be an antiferromagnetically coupled $\{\text{Fe}_4(\mu_3\text{-O})_2\}$ core ($S = 0$) with two coupled Fe centres (Fe2 and Fe2a) indicated in figure 3.6.

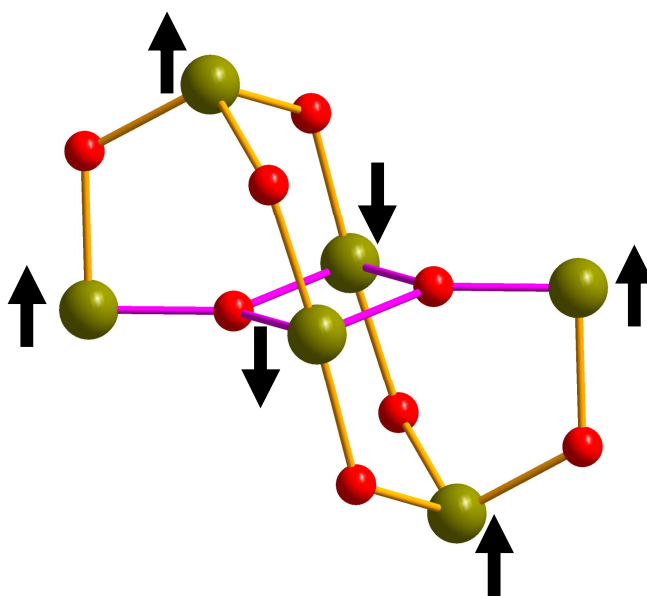


Figure 3.6: Representation of the spin alignment of complexes **6**

Complex **6** appears to follow this rationale.

3.2.2 Discussion of crystal structure of $[\text{Fe}_6\text{O}_2(\text{OMe})_2(\text{L}^2)_2(\text{phbenz})_4(\text{MeOH})_6][\text{NO}_3]_2 \cdot \text{MeOH}$ (**7**·MeOH)

Complex **7**·MeOH contains a hexanuclear Fe(III) complexes which crystallise in the monoclinic space group $P2_1/n$ (figure 3.7 where the atom suffix a signifies symmetry equivalents).

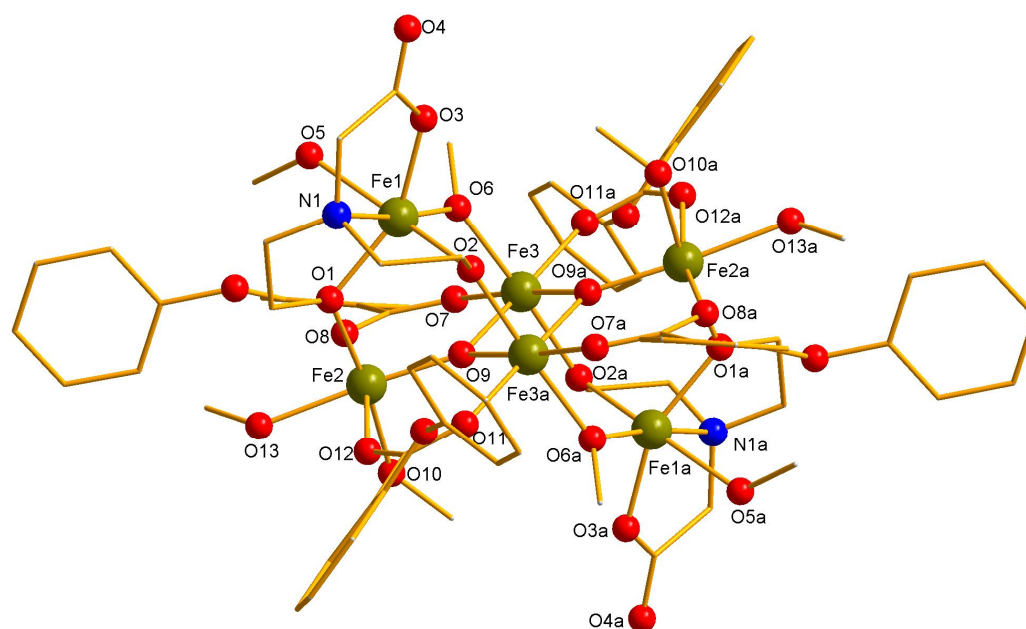


Figure 3.7: Structure of the cation of **7** (ball and stick representation with Fe(III) Gold; O, red; N, blue; C, brown; H atoms are omitted for clarity)[atom suffix a signifies the symmetry equivalent atom: a = 1 _ x, 1 _ y, 1 _ z].

Complex **7** crystallises in a different space group to **6** although only minor changes are observed in the cluster. The Fe_6 complex displays the same $\{\text{Fe}_4\text{O}_2\}$ butterfly unit core (Fe2, Fe3, Fe2a, Fe3a) as **6**, which is capped by two $\{\text{Fe}(\text{Bic})\}$ units that sit above and below the central $\{\text{Fe}_4\text{O}_2\}$ core (figure 3.8). The two bicine ligands display the same binding mode present in **6**. The main difference is the presence of

carboxylate in the final structure. The complex now contains four phenoxybenzoate ligands, which bridge the central $\{\text{Fe}_4\text{O}_2\}$ 'butterfly' core in a 1,3 binding mode. The OH groups found in **6** have now been replaced by two methoxide groups (O6 and O6a). Finally the four pivalate ligands at Fe2 and Fe2a are replaced by four MeOH ligands (O5 and O13) resulting in a change in geometry at the Fe centres to octahedral. The NO_3^- anions are not found positioned above and below the Fe_6 cluster as in complex **6**, instead they are located at the edge of the cluster hydrogen bonded to the terminal methanol ligands (O5) at Fe1 and a methanol solvent molecule in the lattice.

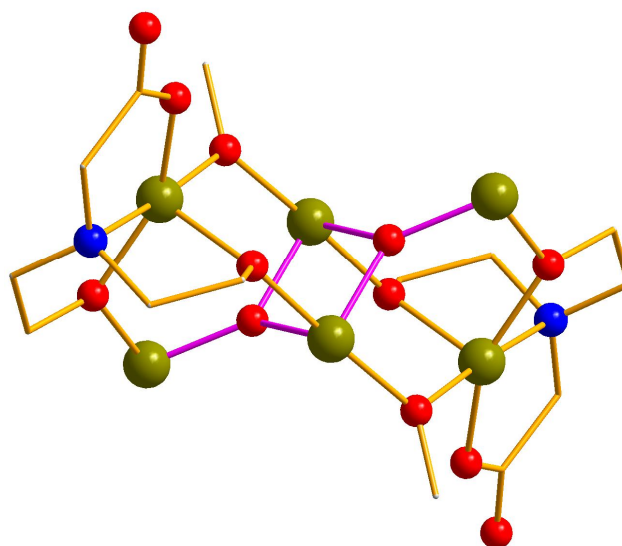


Figure 3.8: $\{\text{Fe}_4\text{O}_2\}$ butterfly core of the cation highlighted in purple with phenoxybenzoate ligands removed. Bicine ligand binding mode is shown.

There are many examples of Fe_6 clusters given in previous chapters, however there are only two relevant examples, $[\text{Fe}_6(\mu_4\text{-O})_2(\mu_2\text{-OMe})_2(\text{OMe})_4(\text{tren})_2]^{2+}$ which shows structural similarities⁴ (for both complex **6** and **7**) and $[\text{Fe}_6(\mu_3\text{-O})_2(\mu_2\text{-OPr}^i)_2(\mu\text{-OPr}^i)_4(\text{O}_2\text{CPh})_4(\mu\text{-O}_2\text{CPh})_4]^{5}$ which displays the same 1,3 bridging and 1,1 capping modes present for complex **6**.

Table 3.5 Data for the crystal structure determination of **7**·MeOH

Empirical formula	C ₇₃ H ₉₂ N ₄ O ₃₉ Fe ₆
fw(gmol ⁻¹)	1984.63
Spacegroup	<i>P</i> 2 ₁ / <i>n</i>
<i>a</i> (Å)	17.841(3)
<i>b</i> (Å)	14.263(2)
<i>c</i> (Å)	18.258(2)
β(deg)	114.857(7)
<i>V</i> (Å ³)	4215.7(11)
<i>Z</i>	2
<i>T</i> (K)	100(2)
λ(Å)	0.71073
ρ _{calcd} (Mg/m ³)	1.599
μ(mm ⁻¹)	1.099
R ₁ (%)	5.13
wR ₂ (%)	8.47
Goodness of fit indicator	0.955

[†]Estimated standard deviations in the least significant figure are given in parentheses.

$${}^aR_1 = \frac{\sum ||F_o| - |F_c||}{\sum |F_o|}$$

$${}^b wR_2 = \left[\frac{\sum [w(F_o^2 - F_c^2)_2]}{\sum [w(F_o^2)_2]} \right]^{1/2}$$

where $w = 1/[\sigma^2(F_o^2) + (0.2P)^2]$ and $P = [F_o^2 + 2Fc^2]/3$

Table 3.6 Selected ligand bond distance for **7**·MeOH

Bond	Distance (Å) [†]	Bond	Distance (Å) [†]
Fe1—N1	2.214(6)	Fe2—O9	1.839(5)
Fe1—O1	1.972(5)	Fe3—O6	2.050(5)
Fe1—O2	1.988(5)	Fe3—O9	1.957(4)
Fe1—O3	1.974(5)	Fe3a—O9	1.943(5)
Fe1—O6	1.995(5)	Fe3a—O2	2.022(5)
Fe2—O1	2.010(6)		

[†] Estimated standard deviations in the least significant figure are given in parentheses.

Bonds in red are for comparison with tables, 3.2 and 3.10.

Table 3.7 Selected bond angles for **7**·MeOH

Atoms	Angle (°) [†]	Atoms	Angle (°) [†]
Fe1—O1—Fe2	116.8(3)	Fe2—O9—Fe3a	133.1(3)
Fe1—O2—Fe3a	121.5(2)	Fe2—O9—Fe3	129.1(3)
Fe1—O6—Fe3	121.5(2)	Fe3—O9—Fe3a	96.8(3)

[†] Estimated standard deviations in the least significant figure are given in parentheses.

Bond angle in red is for comparison with tables, 3.3 and 3.11.

Table 3.8 Bond valence sums for the inorganic oxygen atoms in **7**·MeOH

Atom	BVS	Assignment
O9	1.86	O ²⁻
O6	0.94	OH ⁻

[†] The oxygen atom is an O²⁻ if the BVS is ~2, an OH⁻ if the BVS is ~1, and an H₂O if the BVS is ~0.³

3.2.2.1 Magnetic Susceptibility Measurements for **7**·MeOH

Magnetic susceptibility measurements were carried out on an air-dried sample. For **7**, χT at 300K has a value of 10.10 cm³ mol⁻¹ K, again significantly lower than expected for six non-interacting Fe(III) ions (26.25 cm³ mol⁻¹ K for $g=2$), suggesting strong antiferromagnetic interactions between the Fe(III) centres (figure 3.9).

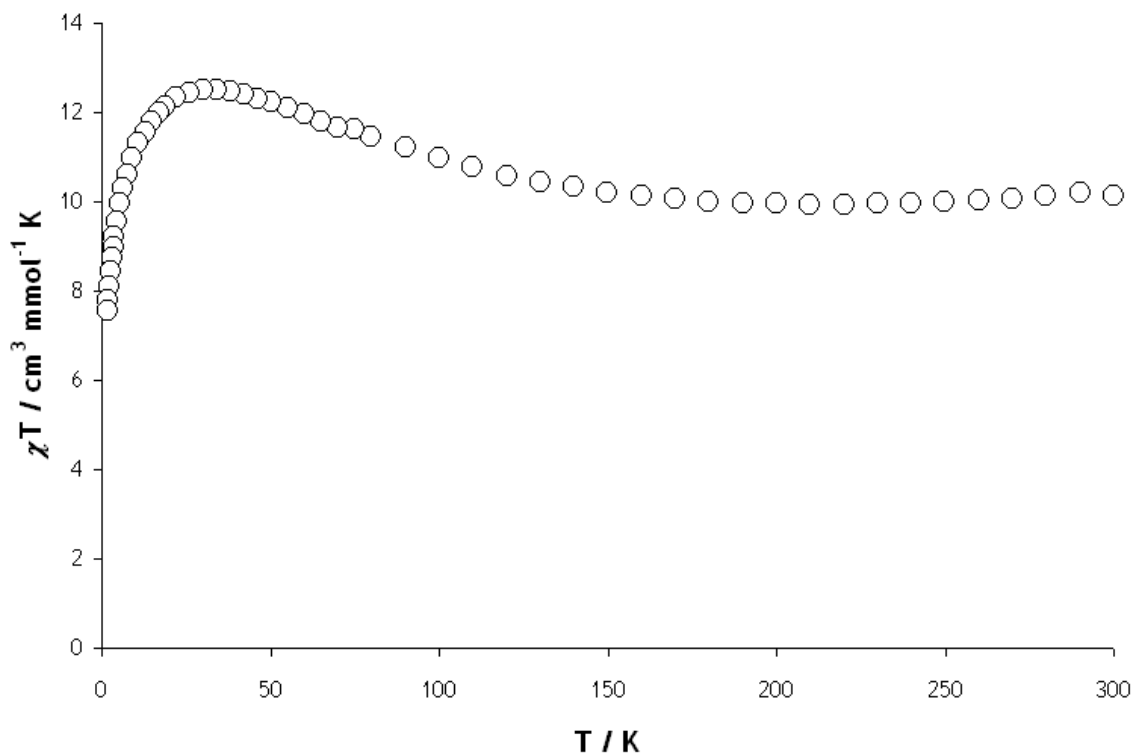


Figure 3.9: Temperature dependence of χT for **7** from 300-1.8 K measured in a field of 1 kOe

The value of χT goes through a local minimum of $10.20 \text{ cm}^3 \text{ mol}^{-1} \text{ K}$ at 170.0 K and slowly begins to rise to a maximum of $12.51 \text{ cm}^3 \text{ mol}^{-1} \text{ K}$ at 34.0 K, then drops sharply to $7.57 \text{ cm}^3 \text{ mol}^{-1} \text{ K}$ at 1.8 K. The magnetisation was measured as a function of applied field at 2 K, the curve does not reach saturation, rising to a value of $M/N\beta=8.6$ at 5 T (figure 3.10).

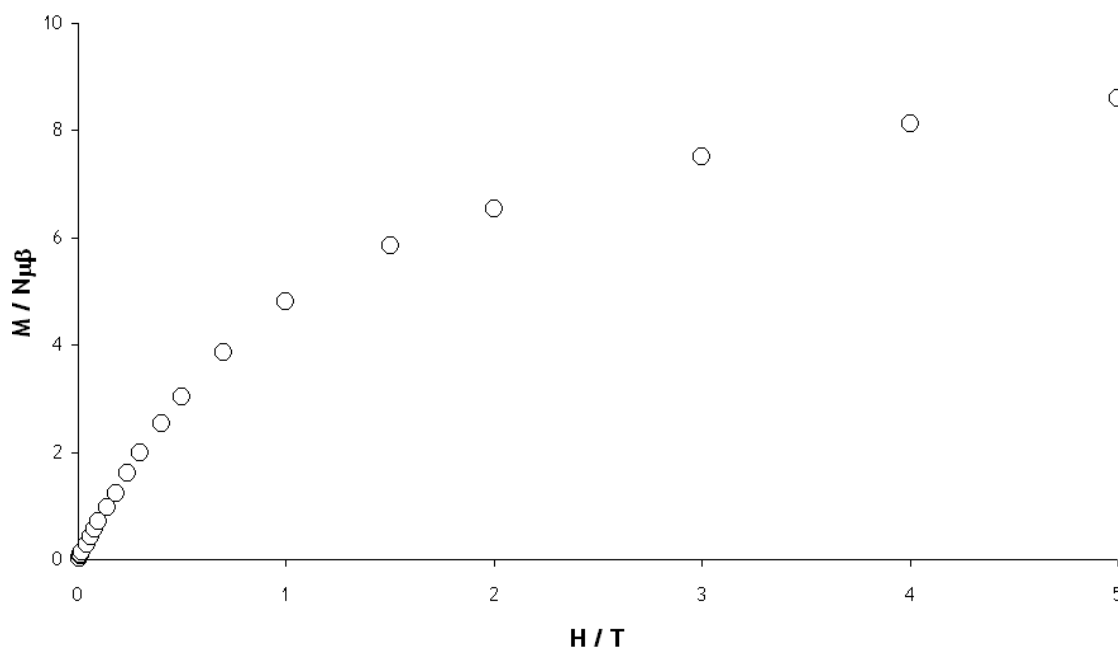


Figure 3.10: magnetisation versus field at 2K for **7**

Both the low temperature maximum in χT and the magnetization data are consistent with a spin ground state of between $S = 4$ and 5 for **7**.

The major difference between complexes **6** and **7** concerns the bridging hydroxide found in **6**, (O1) vs. the methoxide, (O6) found in **7**. The hydroxide could provide a stronger exchange pathway compared to the methoxide which would account for the difference in the magnetic data, associated with the differences in the Fe–O–Fe bridging angles (tables 2.7 and 2.11). The shorter Fe–O bond distance and the larger Fe–O–Fe angles would lead to the strongest exchange.

This type of temperature dependence behaviour was seen for $\text{Fe}_6(\mu_3\text{-O})_2(\mu_2\text{-OPr}^i)_2(\mu\text{-OPr}^i)_4(\text{O}_2\text{CPh})_4(\mu\text{-O}_2\text{CPh})_4$ by Ammalla *et al.*,⁴ who reported their complex to possess an $S = 3$ ground state.

3.2.3 Discussion of crystal structure of $[\text{Et}_2\text{NH}_2]_2[\text{Fe}_6\text{O}_2(\text{OH})_2(\text{L}^2)_2(\text{OAc})_8]$ (**8**)

A change of carboxylate in the triangle starting material resulted in complex **8**, a hexanuclear Fe(III) complex which crystallise in the orthorhombic space group *Pbca* (figure 3.11).

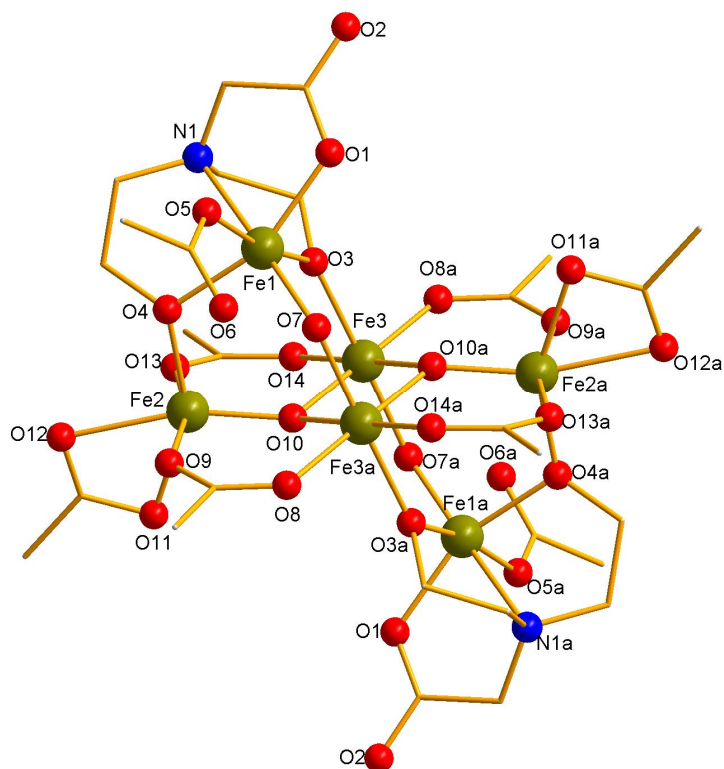


Figure 3.11: Structure of the anion of **8** (ball and stick representation with Fe(III) Gold; O, red; N, blue; C, brown; H atoms are omitted for clarity)[atom suffix a signifies the symmetry equivalent atom: $a = 1 - x, 1 - y, 1 - z$].

We have another complex that crystallises in a different space group however, no overall difference in structure is observed in the final complex as **8** is homeo-structural to **6**, with pivalate ligands replaced by acetate. The bicine ligand displays the same μ_3 binding mode seen in both **6** and **7**. The change of ligand has resulted in small changes in the structure such as Fe–O–Fe bond angles. Magnetic characterisation of complex **8**, was not completed due to poor crystal yield obtained from the synthesis. However from the previous complexes we can speculate that **8** will also possess a ground state of $S = 5$. A comparison of the bond

angles and distances of **8** with both **6** and **7** indicates that complex **8** should show similar magnetic behaviour to complex **6** although magnetic characterisation is still needed to confirm this. Although **8** was not completely characterised, these complexes formed highlight the stability of the product formed in solution, which add to the growing family of Fe₆ complexes.

Table 3.9 Data for the crystal structure determination of **8**

Empirical formula	C ₂₈ H ₇₀ N ₂ O ₂₈ Fe ₆
fw(gmol ⁻¹)	1314.04
Spacegroup	<i>Pbca</i>
a(Å)	12.556(19)
b(Å)	19.948(3)
c(Å)	22.503(3)
V(Å ³)	5636.4(15)
Z	1
T(K)	100(2)
λ(Å)	0.71073
ρ _{calcd} (Mg/m ³)	1.579
μ(mm ⁻¹)	1.589
R ₁ (%)	13.69
wR ₂ (%)	23.59
Goodness of fit indicator	1.158

[†]Estimated standard deviations in the least significant figure are given in parentheses.

$${}^aR_1 = \frac{\sum ||F_o| - |F_c||}{\sum |F_o|}$$

$${}^b wR_2 = \left[\frac{\sum [w(F_o^2 - F_c^2)]}{\sum [w(F_o^2)]} \right]^{1/2}$$

$$\text{where } w = 1/[\sigma^2(F_o^2) + (0.2P)^2] \text{ and } P = [F_o^2 + 2F_c^2]/3$$

Table 3.10 Selected ligand bond distance for **8**

Bond	Distance (Å) [†]	Bond	Distance (Å) [†]
Fe1–N1	2.224(13)	Fe2–O10	1.829(9)
Fe1–O4	2.054(11)	Fe3a–O7	1.983(10)
Fe1–O3	1.998(10)	Fe3–O10	1.968(9)
Fe1–O1	2.036.(12)	Fe3a–O10	1.968(9)
Fe1–O7	1.925(9)	Fe3–O3	2.032(9)
Fe2–O4	1.953(12)		

[†] Estimated standard deviations in the least significant figure are given in parentheses.

Bonds in red are for comparison with tables, 3.2 and 3.6.

Table 3.11 Selected bond angles for **8**

Atoms	Angle (°) [†]	Atoms	Angle (°) [†]
Fe1–O3–Fe3	125.3(4)	Fe2–O10–Fe3	129.7(3)
Fe1–O4–Fe2	115.5(5)	Fe2–O10–Fe3a	125.1(5)
Fe1–O7–Fe3	127.9(2)	Fe3–O10–Fe3a	96.0(4)

[†] Estimated standard deviations in the least significant figure are given in parentheses.

Bond angle in red is for comparison with tables, 3.3 and 3.7.

Table 3.12 Bond valence sums for the inorganic oxygen atoms in **8**

Atom	BVS	Assignment
O10	1.86	O ²⁻
O7	0.94	OH ⁻

[†] The oxygen atom is an O²⁻ if the BVS is ~2, an OH⁻ if the BVS is ~1, and an H₂O if the BVS is ~0.³

3.2.4 Discussion of crystal structure of $[\text{Fe}_{12}\text{O}_4(\text{L}^2)_4(\text{HL}^2)_4(\text{piv})_8]$ (**9**·5MeCN)

The change of base from Et_2NH to NaOMe resulted in a dodecanuclear complex **9**, which crystallises in the monoclinic space group $C2/c$ (figure 3.12).

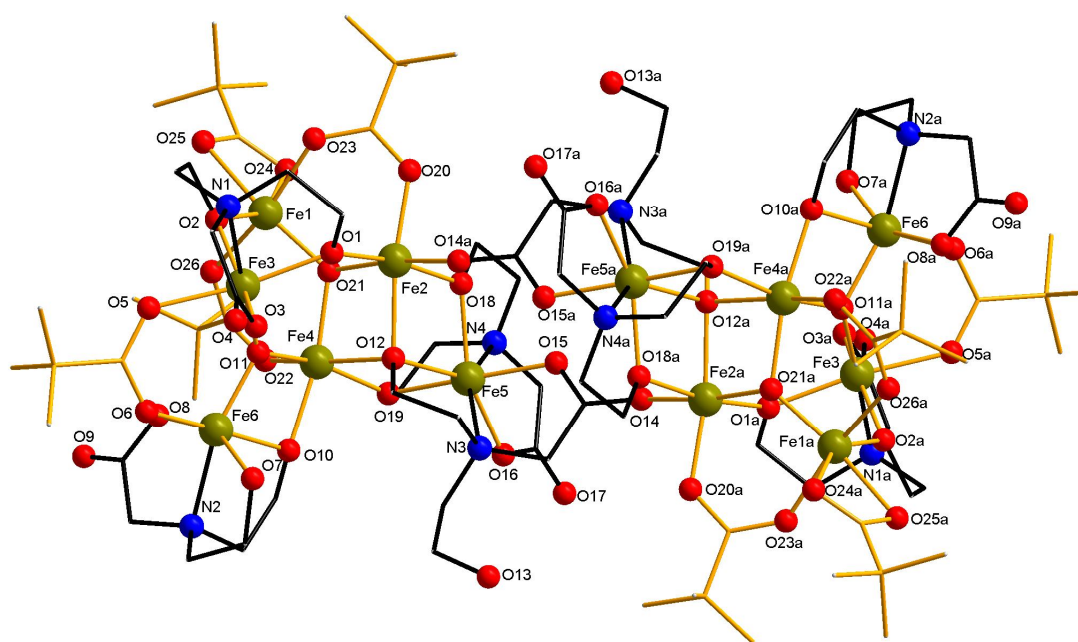


Figure 3.12: Structure of **9** (ball and stick representation with Fe(III) Gold; O, Red; N, Blue; C, Brown; H atoms are omitted for clarity)[atom suffix a signifies the symmetry equivalent atom: $a = 1 _ x, 1 _ y, 1 _ z$]. Ligand bonds are highlighted in black.

Complex **9** is best described as a dimer of Fe_6 units, both of which display a different cluster topology to the previous Fe_6 clusters. The two units are linked through the carboxylate arms of the bicine ligand (O14a and O15a) at a distance of 6 Å between Fe2 and Fe5a (and symmetry equivalents figure 3.13).

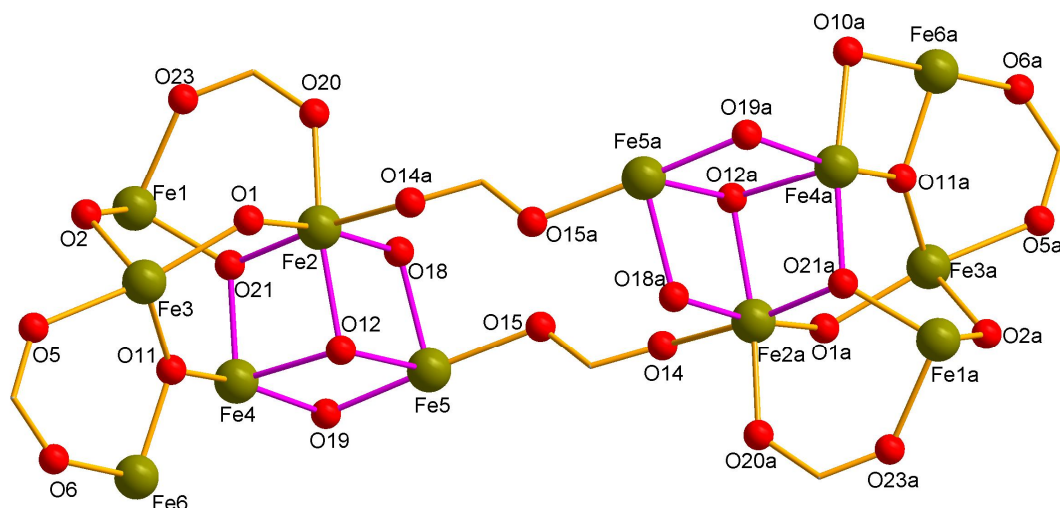


Figure 3.13: Core structure of **9**

Surprisingly, the stable butterfly core seen for complexes **6** – **8** is absent from the final structure of **9** most likely due to more bicine being incorporated into the structure. The structure of each Fe_6 unit is formed from two corner sharing Fe_3O triangles ($\text{Fe}_3, \text{Fe}_6, \text{Fe}_4$ and $\text{Fe}_1, \text{Fe}_2, \text{Fe}_4$). Three $\text{CH}_2\text{CH}_2\text{O}^-$ arms ($\text{O}_{18}, \text{O}_{19}$ and O_{12}) bridge Fe_5 to Fe_2 and Fe_4 to form an incomplete cubane. The bicine ligand is present in three different binding modes. The triply deprotonated bicine ligands, which binds to Fe_3 through N_1 and Fe_5 through N_4 displays the same μ_3 binding mode to that found in **6** – **8**. One doubly deprotonated ligand caps Fe_6 , with one of the $\text{CH}_2\text{CH}_2\text{O}^-$ arms bridging bidentate (Fe_6 to Fe_4). The CH_2COO^- arm (O_8) binds monodentate as well as the remaining $\text{CH}_2\text{CH}_2\text{OH}$ arm which is protonated and binds monodentate to Fe_6 . The final bicine ligand (bound at Fe_5 through N_3) displays a new binding mode, bridging the two dimer units through the CH_2COO^- arms (O_{14} and O_{15a}). One $\text{CH}_2\text{CH}_2\text{O}^-$ arm (O_{12}), displays μ_3 bridging (between $\text{Fe}_5, \text{Fe}_2, \text{Fe}_4$), the final $\text{CH}_2\text{CH}_2\text{OH}$ arm (O_{13}) remains protonated and unbound (figure 3.14).

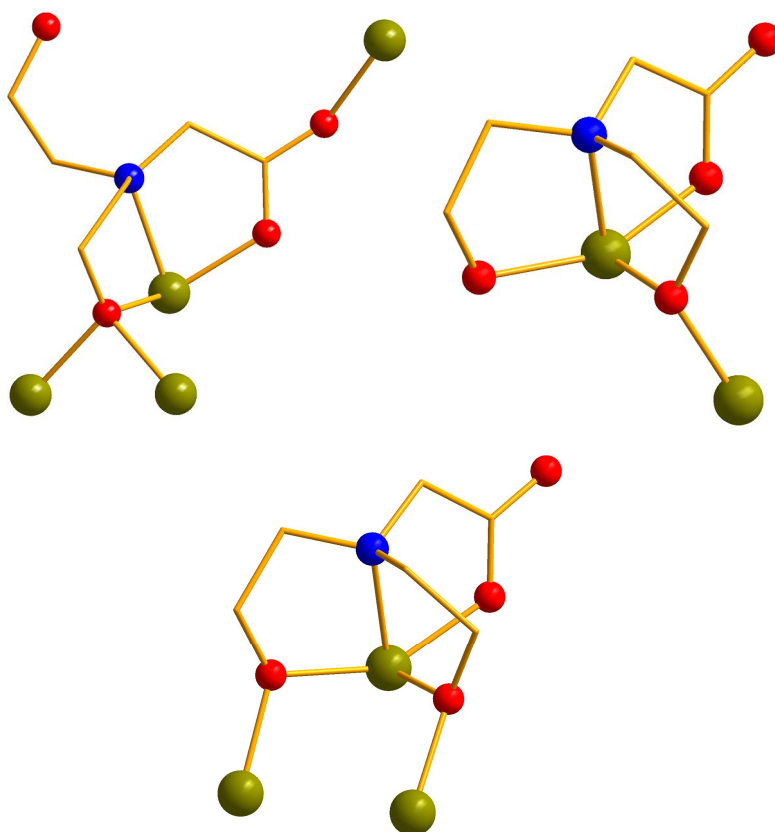


Figure 3.14: binding modes of HL^2 and L^2 found in complex **9**

The pivalate ligands are present in two forms, six of which display the 1,3-bridging mode and the remaining two, 1,1 capping at Fe1 and Fe1a as found in complexes **6** – **8**. All Fe centres are six-coordinate except Fe5 (and Fe5a) which displays 7-coordinate pentagonal bipyramid geometry. Again this geometry has been previously seen with these ligand types.⁶ The core of this cluster is completely novel, the closest relevant example being an Fe_{12} complex in which the core is comprised of face-sharing defect $\{Fe_3O_4\}^+$ cuboidal units.⁷ These findings highlight not only the versatility of the bicine ligand, which can exist in different binding modes, but the importance of the nature of the base used and its effect on the cluster produced from the reaction.

Table 3.13 Data for the crystal structure determination of **9**

Empirical formula	C ₉₂ H ₁₇₀ N ₁₀ O ₅₆ Fe ₁₂
fw(gmol ⁻¹)	2982.58
Spacegroup	C2/c
a(Å)	29.795(5)
b(Å)	20.638(4)
c(Å)	27.218(8)
β(deg)	120.749(7)
V(Å ³)	14384(6)
Z	8
T(K)	100(2)
λ(Å)	0.71073
ρ _{calcd} (Mg/m ³)	1.304
μ(mm ⁻¹)	1.247
R ₁ (%)	5.75
wR ₂ (%)	6.04
Goodness of fit indicator	1.0927

[†] Estimated standard deviations in the least significant figure are given in parentheses.

$${}^a R_1 = \frac{\sum ||F_o| - |F_c||}{\sum |F_o|}$$

$${}^b wR_2 = \left[\frac{\sum [w(F_o^2 - F_c^2)]}{\sum [w(F_o^2)]} \right]^{1/2}$$

$$\text{where } w = 1/[\sigma^2(F_o^2) + (0.2P)^2] \text{ and } P = [F_o^2 + 2F_c^2]/3$$

Table 3.14 Selected ligand bond distance for **9**

Bond	Distance (Å) [†]	Bond	Distance (Å) [†]
Fe5—N3	2.274(4)	Fe5—N4	2.276(4)
Fe5—O ₂ CCH ₂ R	2.037(3)	Fe5—O ₂ CCH ₂ R	2.070(3)
Fe5—OCH ₂ CH ₂ R'	2.214(3)	Fe5—OCH ₂ CH ₂ R'	1.992-2.053(3)
Fe2—O ₂ CCH ₂ R	2.047(3)	Fe3—N1	2.206(4)
Fe6—N2	2.211(4)	Fe3—O ₂ CCH ₂ R	2.042(4)
Fe6—O ₂ CCH ₂ R	1.998(4)	Fe3—OCH ₂ CH ₂ R'	2.012-2.045(4)
Fe6—OCH ₂ CH ₂ R'	1.996-2.112(5)		

Where $R = N(CH_2CH_2OH)_2$ and $R' = (O_2CCH_2)N(CH_2CH_2OH)$

[†] Estimated standard deviations in the least significant figure are given in parentheses.

Table 3.15 Selected bond angles for **9**

Atoms	Angle (°) [†]	Atoms	Angle (°) [†]
Fe1–O2–Fe3	116.5(15)	Fe4–O12–Fe5	98.6(14)
Fe2–O1–Fe3	125.4(17)	Fe5–O18–Fe2	110.2(17)
Fe2–O12–Fe5	100.7(15)	Fe5–O19–Fe4	110.0(17)
Fe4–O12–Fe2	92.7(13)	Fe6–O10–Fe4	96.87(15)

[†] Estimated standard deviations in the least significant figure are given in parentheses.

Table 3.16 Bond valence sums for the inorganic oxygen atoms in **9**

Atom	BVS	Assignment
O11	1.85	O ²⁻
O21	1.77	O ²⁻

[†] The oxygen atom is an O²⁻ if the BVS is ~2, an OH⁻ if the BVS is ~1, and an H₂O if the BVS is ~0.³

3.2.4.1 Magnetic Susceptibility Measurements for **9**·5MeCN

Magnetic susceptibility measurements were carried out on an air-dried sample. The χT value at 300K is 16.7 cm³ mol⁻¹ K, significantly lower than the expected value for twelve uncoupled Fe(III) ions of 52.5 cm³ mol⁻¹ K, indicating strong antiferromagnetic interactions within the cluster. The value of χT decreases sharply to a value of 0.09 cm³ mol⁻¹ K at 1.8 K, consistent with a spin ground state of zero (figure 3.15).

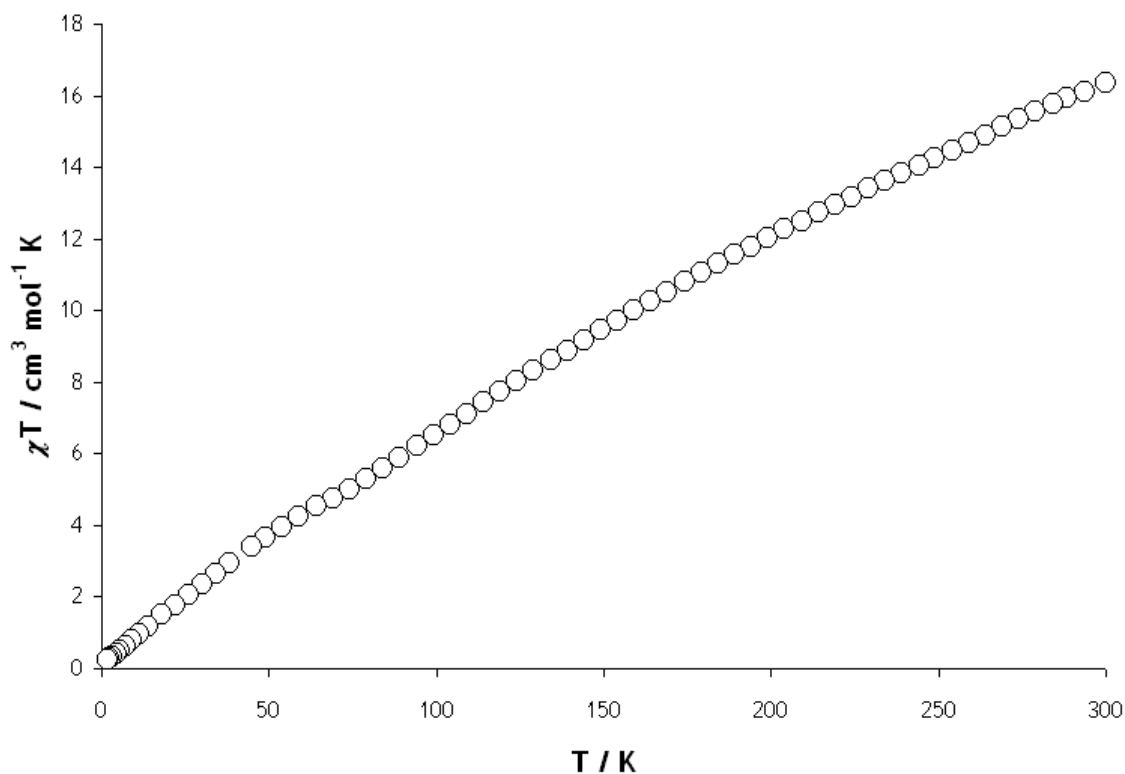


Figure 3.15: Temperature dependence of χT for **9** from 300-1.8 K measured in a field of 1 kOe

3.2.5 Synthesis of $[\text{Fe}_2^{\text{III}}\text{Fe}_4^{\text{II}}\text{O}_2(\text{OBz})_{10}(\text{MeCN})_4]$ (**10**)

The synthesis of complexes **6** to **9** highlight the importance of not only the triangle employed in the reaction but also the significance of base used. The synthesis of **10** highlights the importance of controlling the ratio of reactants. Complex **10** is a mixed valence hexanuclear iron cluster composed of two Fe(III) and four Fe(II) ions, which crystallises in the orthorhombic space group $P2_12_12_1$ (figure 3.16).

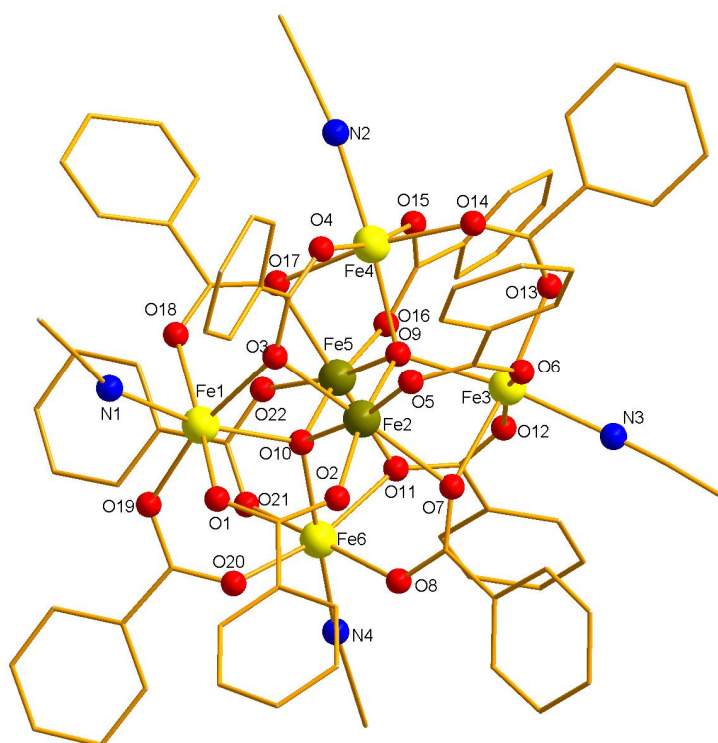


Figure 3.16: Structure of **10** (ball and stick representation with Fe(III) gold; Fe(II) yellow; O, red; N, blue; C, brown; H atoms are omitted for clarity)

The structural core consists of an edge-sharing bi-tetrahedral core. At the centre of each tetrahedra lie two μ_4 O^{2-} ions (figure 3.17). Of the ten benzoate ligands, six are 1,3 bridging and a further four are 1,1,3-bridging between one Fe(III) ion and two Fe(II) ions (figure 3.18). Finally four MeCN groups are located at the four Fe(II) ions completing their coordination sphere. Each Fe centre is six coordinate and displays slightly distorted octahedral geometry. The Fe_6O_2 core can also be described as two smaller $[Fe_3O]^{5+}$ units joined together by each of the two μ_3-O^{2-} atoms which become μ_4 due to ligation of the Fe(III) centre from the adjacent Fe_3O unit, Fe(1, 6 and 2) O(10) and Fe(4, 3 and 5) O(9) or Fe(1, 6 and 5) O(10) and Fe(4, 3 and 2) O(9).

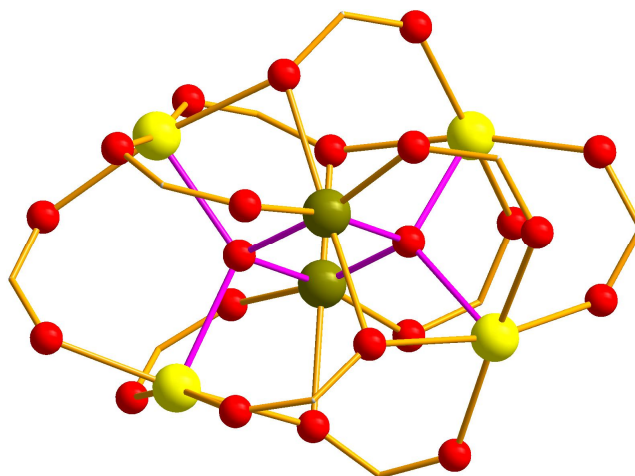


Figure 3.17: Bi-tetrahedral core of **10**

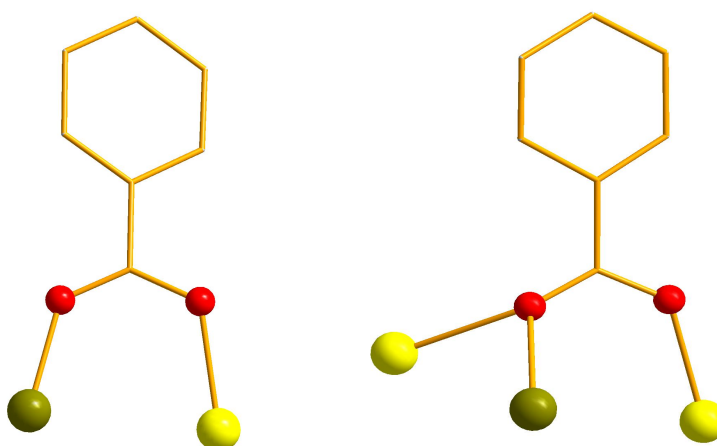


Figure 3.18: Bidentate and tridentate binding mode of benzoate ligands in **10**

Interestingly no bicine is present in the final structure. If we compare the synthesis of **10** with the previous bicine complexes, we can identify two main differences: a change of carboxylate and an increase of three equivalents of the oxo-centred carboxylate triangle has resulted in the absence of bicine from the structure. Complex **10** is analogous to $[\text{Mn}^{\text{II}}_2\text{Mn}^{\text{III}}_4\text{O}_2(\text{O}_2\text{CPh})_{10}(\text{MeCN})_4]$.⁸ In-fact there are only seven clusters with the same $\{\text{Mn}_4^{\text{II}}\text{Mn}_2^{\text{III}}\text{O}_2\}^{10+}$ core. The synthetic approach to these varies from simple $\text{Mn}_2(\text{O}_2\text{CPh})_2 \cdot 2\text{H}_2\text{O}$ salts to $[\text{Mn}_3\text{O}(\text{O}_2\text{CPh})_6(\text{py})_2(\text{H}_2\text{O})]$ ⁹ triangles similar to ours. Theses Mn_6 structures vary in ligation of nitrogen donors at the $\text{M}(\text{II})$ centres from four MeCN molecules⁷ to a mixture of pyridine, 4-(hydroxymethyl)pyridine and pyrimidine.⁸ In all of these the ligand employed in the reactions are incorporated into the final structure which is not the case for our

complex. Although the structure of **10** is known in manganese chemistry, to the best of our knowledge it is unique in iron chemistry.

Table 3.17 Data for the crystal structure determination of **10**

Empirical formula	C ₇₈ H ₆₂ N ₄ O ₂₂ Fe ₆
fw(gmol ⁻¹)	1742.46
Spacegroup	P2 ₁ 2 ₁ 2 ₁
a(Å)	17.55(7)
b(Å)	25.26(4)
c(Å)	38.67(15)
V(Å ³)	17150(100)
Z	8
T(K)	100(2)
λ(Å)	0.71073
ρ _{calcd} (Mg/m ³)	1.349
μ(mm ⁻¹)	1.057
R ₁ (%)	6.78
wR ₂ (%)	9.31
Goodness of fit indicator	0.739

[†]Estimated standard deviations in the least significant figure are given in parentheses.

$${}^a R_1 = \frac{\sum ||F_o| - |F_c||}{\sum |F_o|}$$

$${}^b wR_2 = \left[\frac{\sum [w(F_o^2 - F_c^2)]_2}{\sum [w(F_o^2)]_2} \right]^{1/2}$$

$$\text{where } w = 1/[\sigma^2(F_o^2) + (0.2P)^2] \text{ and } P = [F_o^2 + 2F_c^2]/3$$

Table 3.18 Selected bond distance for **10**

Bond	Distance (Å) [†]	Bond	Distance (Å) [†]
Fe1–N1	2.351(18)	Fe4–N2	2.322(16)
Fe1–O1	2.229(13)	Fe4–O4	2.219(9)
Fe1–O3	2.408(16)	Fe4–O9	2.239(13)
Fe1–O10	2.249(13)	Fe4–O14	2.193(15)
Fe1–O18	2.199(14)	Fe4–O15	2.233(14)
Fe1–O19	2.163(16)	Fe4–O17	2.312(15)
Fe2–O2	2.030(15)	Fe5–O9	1.980(13)
Fe2–O3	2.277(14)	Fe5–O10	1.969(12)
Fe2–O5	2.032(14)	Fe5–O11	2.315(14)
Fe2–O7	2.299(14)	Fe5–O16	2.028(14)
Fe2–O9	1.973(14)	Fe5–O17	2.305(14)
Fe2–O10	1.968(13)	Fe5–O22	2.034(14)
Fe3–N3	2.320(17)	Fe6–N4	2.329(16)
Fe3–O6	2.260(13)	Fe6–O8	2.208(15)
Fe3–O7	2.380(16)	Fe6–O10	2.263(13)
Fe3–O9	2.264(13)	Fe6–O11	2.310(17)
Fe3–O12	2.217(14)	Fe6–O20	2.171(15)
Fe3–O13	2.179(15)	Fe6–O21	2.255(15)

[†] Estimated standard deviations in the least significant figure are given in parentheses.

Table 3.19 Selected bond angles for **10**

Atoms	Angle (°) [†]	Atoms	Angle (°) [†]
Fe1–O2–Fe3	116.5(15)	Fe4–O12–Fe5	98.6(14)
Fe2–O1–Fe3	125.4(17)	Fe5–O18–Fe2	110.2(17)
Fe2–O12–Fe5	100.7(15)	Fe5–O19–Fe4	110.0(17)
Fe4–O12–Fe2	92.7(13)	Fe6–O10–Fe4	96.87(15)

[†] Estimated standard deviations in the least significant figure are given in parentheses.

Table 3.20 Bond valence sums for the inorganic oxygen atoms in **10**

Atom	BVS	Assignment
O9	1.64	O ²⁻
O10	1.61	O ²⁻

The oxygen atom is an O²⁻ if the BVS is ~2, an OH⁻ if the BVS is ~1, and an H₂O if the BVS is ~0.³

Table 3.21 Bond valence sums for the iron centres in **10**

Atom	BVS	Assignment
Fe1	1.56	Fe ²⁺
Fe2	2.64	Fe ³⁺
Fe3	1.53	Fe ²⁺
Fe4	1.59	Fe ²⁺
Fe5	2.53	Fe ³⁺
Fe6	1.58	Fe ²⁺

3.2.5.1 Magnetic Susceptibility Measurements for **10**

Magnetic susceptibility measurements were carried out on an air-dried sample, which analysed as **10**. For **10**, χT at 300 K has a value of 7.00 cm³ mol⁻¹ K, significantly lower than expected for four non-interacting Fe(II) ions and two non-interacting Fe(III) ions (20.75 cm³ mol⁻¹ K for $g=2$), suggesting very strong antiferromagnetic interactions between the Fe(II)/Fe(III) centres (figure 3.20).

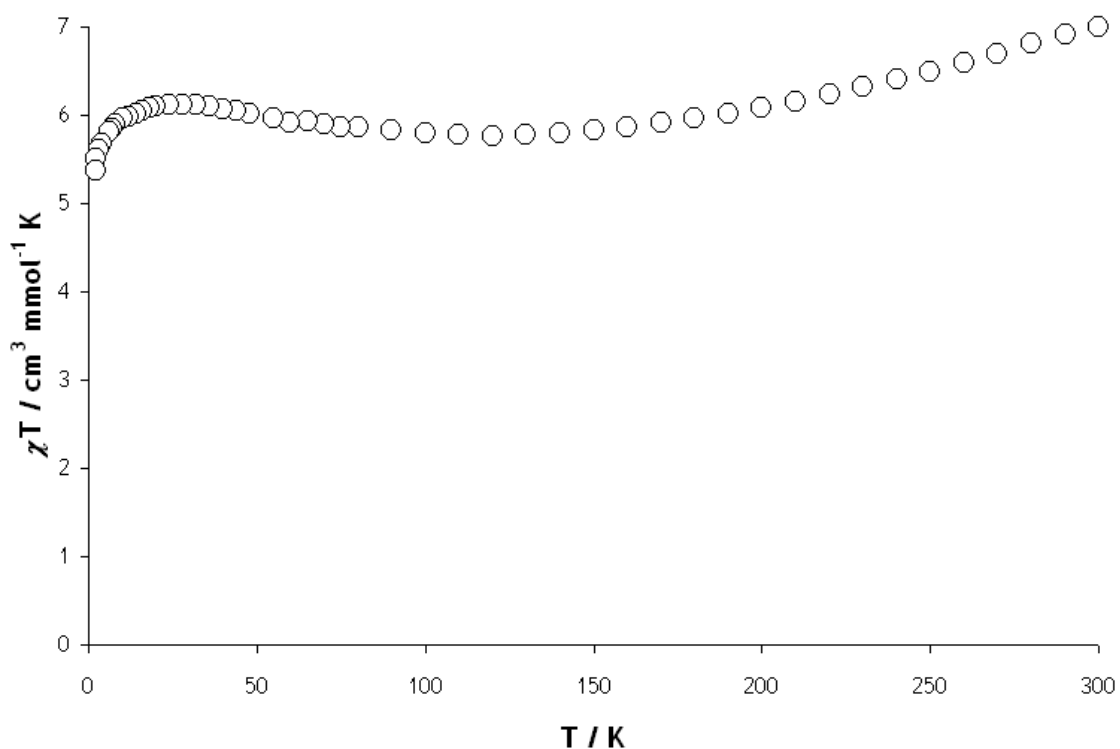


Figure 3.20: Temperature dependence of χT for **10** from 300-1.8 K measured in a field of 1 kOe

The value of χT slowly decreases to a minimum of $5.76 \text{ cm}^3 \text{ mol}^{-1} \text{ K}$ at 120.0 K, then begins to rise slightly to a maximum of $6.13 \text{ cm}^3 \text{ mol}^{-1} \text{ K}$ at 26.0 K then drops to $5.31 \text{ cm}^3 \text{ mol}^{-1} \text{ K}$ at 1.8 K. The low temperature maximum in χT suggests an $S = 3$ ground state consistent with the antiferromagnetic exchange between four Fe(II) centres and two Fe(III) centres. The magnetisation was measured as a function of applied field at 2 K, the curve does not reach saturation, rising to a value of $M/N\beta=4.51$ at 5 T (figure 3.21).

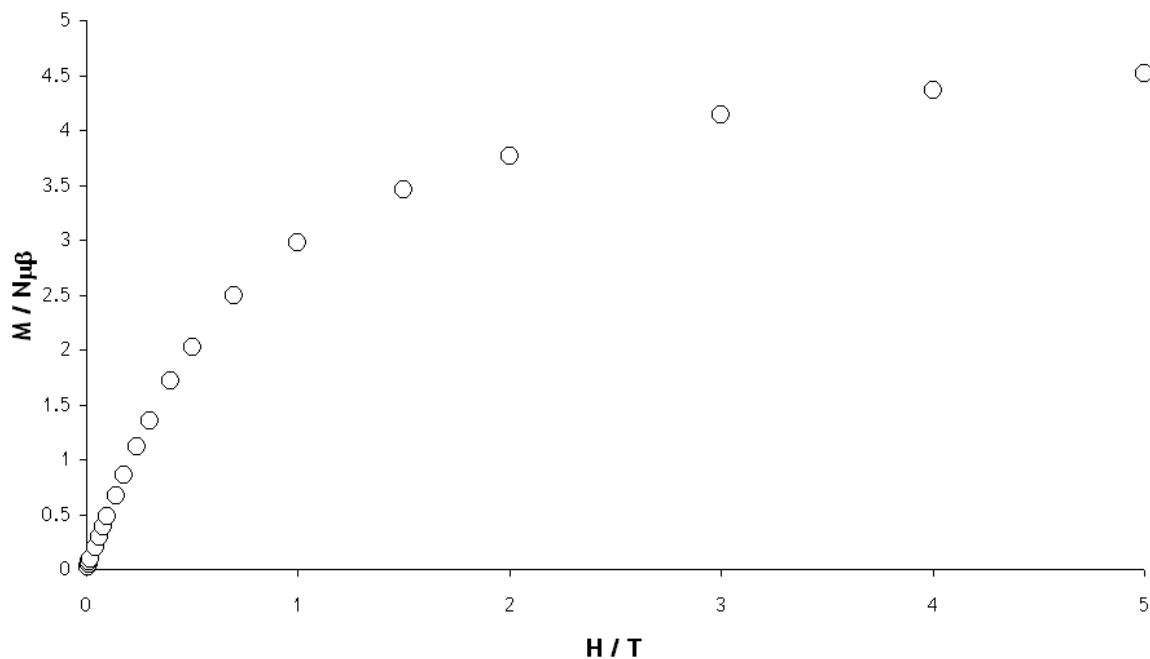


Figure 3.21: magnetisation versus field at 2K for **10**

Both the low temperature maximum in χT and the magnetisation data are consistent with a spin ground state of $S = 3$ for **10**. This is consistent with the antiferromagnetic exchange between four Fe(II) centres and two Fe(III) centres. The slightly lower value observed in the magnetisation vs. field could be attributed to anisotropy of the cluster.

By examination of the bridging angles in the cluster we can separate them into two categories. Angles between the terminal Fe centres (Fe1–Fe6 and Fe3–Fe4) are between 119.01–120.40 and the remaining Fe centres (Fe5–Fe2) are 96.70–97.40. If we assume the largest angle will contribute the strongest antiferromagnetic interaction *i.e* the spins of Fe1–Fe6 and Fe4–Fe3 will be antiferromagnetically coupled to the central Fe atoms (Fe2 and Fe5). The remaining spins of Fe2 and Fe5 we would assume to be ferromagnetically coupled due to the shorter bridging angles close to 90°. ¹⁰ This would give a total of four “spin up” $S = 2$ centres and two “spin down” $S = 5/2$ centres and an $S = 3$ ground state (figure 3.22).

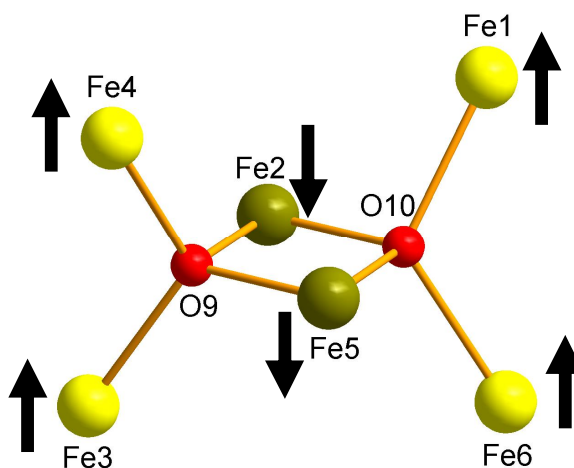


Figure 3.22: Representation of the spin alignment present in **10** with carboxylate removed

In order to determine the zero-field splitting parameter D and confirm the spin ground-state, and g value for **10**, magnetisation data were collected in the ranges 5-30 kG and 3-7 K (figure 3.23). The data were fit by a matrix digitalization method using the program MAGMOFIT to a model that assumes only the ground state is populated, includes axial zero-field splitting ($D\hat{S}_z^2$) and the Zeeman interaction, and carries out a full powder average.¹¹ The corresponding Hamiltonian is given by *Equation 3.1*.

$$\hat{H} = D\hat{S}_z^2 + g\mu_B\mu_0\hat{S}_zH$$

Equation 3.1

Where D is the axial anisotropy, μ_B is the Bohr magneton, μ_0 is the vacuum permeability, \hat{S}_z is the easy-axis spin operator, and H_z is the applied field. The best fit gave a spin ground state of $S = 3$ with $g = 2.088$ and $D = -2.40 \text{ cm}^{-1}$.

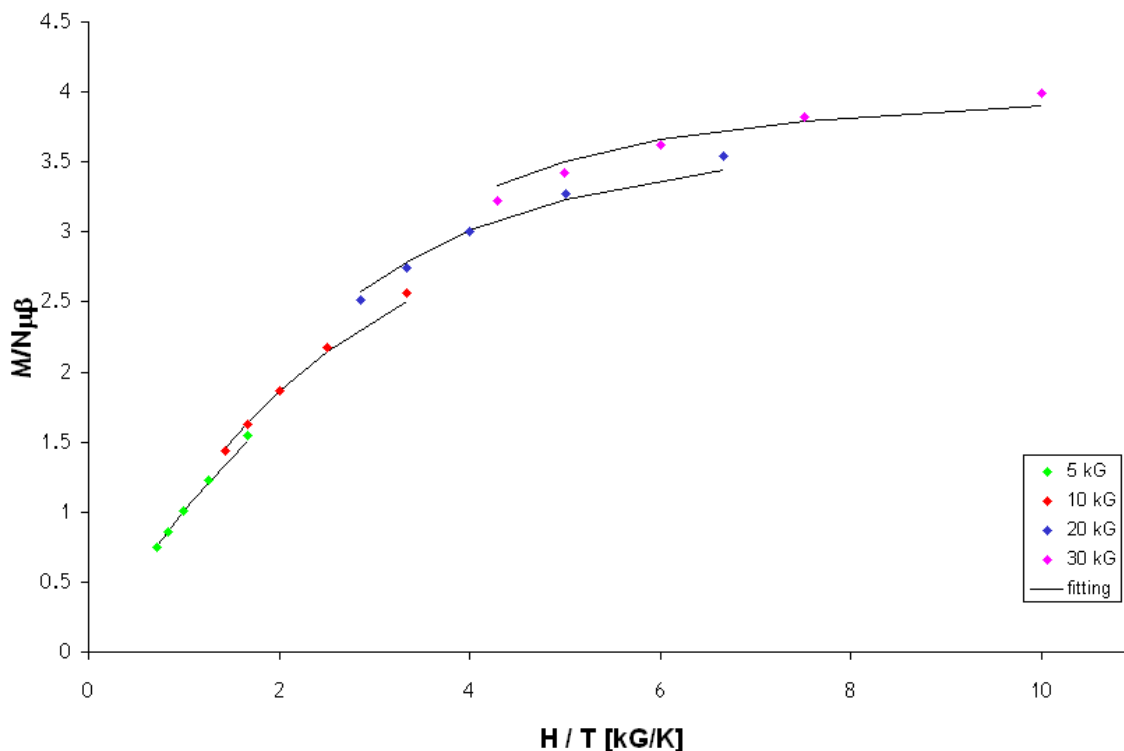


Figure 3.23: magnetisation data collected in the ranges 5-30 kG and 3-7 K

Ac susceptibility measurements were also carried out for **10**, however there was no increase in the χ'' signal down to 1.8K for any of the frequencies measured. This suggests that the compound shows no slow relaxation of magnetization down to 1.8 K. This is surprising as the energy barrier to the reorientation of magnetisation would be 21.6 cm^{-1} if the value of D is accurate from the fit of the reduced magnetization. Further magnetic measurements to lower temperature and EPR are needed to confirm whether or not **10** is an SMM and to determine the correct value of D .

3.2.6 Synthesis of $[\text{Et}_2\text{NH}][\text{Et}_2\text{NH}_2][\text{Fe}_6\text{O}_2(\text{OAc})_{15}(\text{HOAc})_2]$ (**11**·2MeCN)

Continuing to alter the reaction conditions resulted in the synthesis of complex **11**, a hexanuclear complex that crystallises in the orthorhombic space group $Pn\bar{m}$ (figure 3.24 where the atom suffix a signifies symmetry equivalents).

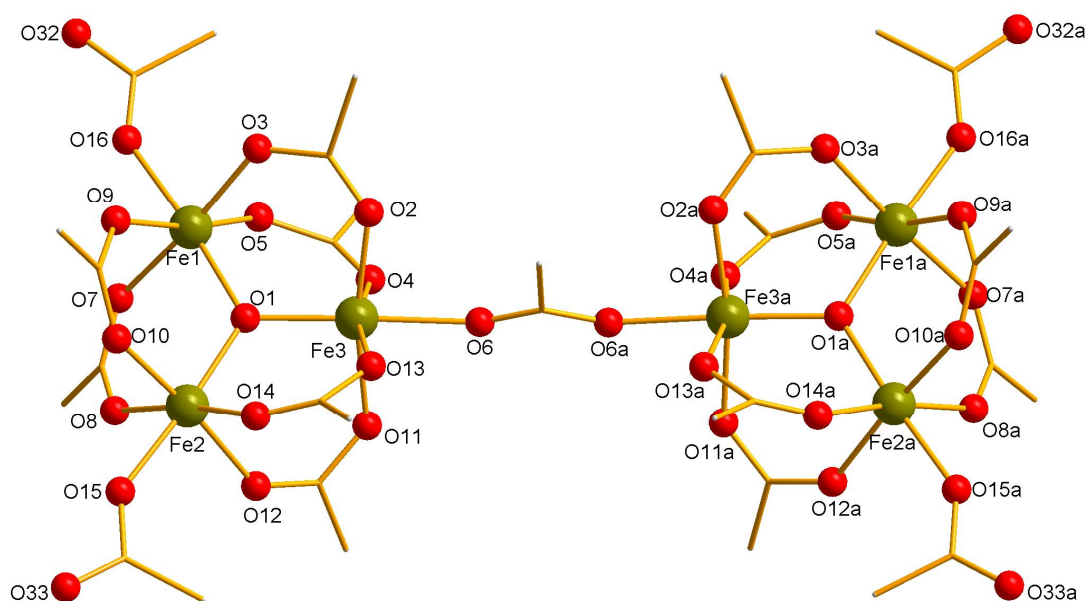


Figure 3.24: Structure of the anion of **11** (ball and stick representation with Fe(III) Gold; O, Red; C, Brown; H atoms are omitted for clarity)[atom suffix a signifies the symmetry equivalent atom: a = 1 - x, 1 - y, 1 - z].

Notably the bicine ligand again has failed to be incorporated into the final structure. This was achieved by not only an increase in the amount of metal triangle but also the amount of base was increased four fold. The complex is best described as two oxo-centred carboxylate triangles linked through a central acetate group. The acetate ligands are present in three binding modes; twelve bind in a 1,3 bridging mode, four act as terminal ligands; two of which remain protonated (O32) and hydrogen bonded to Et_2NH in the lattice. The other two ligands are deprotonated (O33) and hydrogen bonded to Et_2NH_2 in the lattice. All four bind mono-dentate to the outer Fe centres (Fe1, Fe1a, Fe2 and Fe2a). The final acetate ligand displays a 1,3 mode and bridges the two units binding Fe3 to Fe3a. All Fe centres display an octahedral geometry that is slightly distorted due to the carboxylate groups. It is not unusual to observe these triangles as a final product, (see the Cambridge structural database, CSD)¹² however triangles that are linked together are less common. Only one example with manganese involves linking one carboxylate triangle to another manganese centre via dichloroacetate creating a 1-

D manganese chain.¹³ The only examples of linked carboxylate triangle are reported by Bino and Gibson.¹⁴ These use hydrogen oxide (H_3O_2^-) to bridge tungsten and molybdenum oxo-triangles through hydrogen bonding. Therefore complex **11** presents the first example of linked carboxylate triangles involving Iron(III).

Table 3.22 Data for the crystal structure determination of **11**

Empirical formula	$\text{C}_{44}\text{H}_{82}\text{N}_3\text{O}_{37}\text{Fe}_6$
fw(g mol^{-1})	1552.21
Spacegroup	<i>Pnmm</i>
a(Å)	20.67(5)
b(Å)	12.92(3)
c(Å)	13.16(15)
V(Å ³)	3513 (100)
Z	2
T(K)	100(2)
λ (Å)	0.71073
ρ_{calcd} (Mg/m^3)	1.510
μ (mm^{-1})	1.296
R ₁ (%)	6.31
wR ₂ (%)	16.78
Goodness of fit indicator	1.187

[†]Estimated standard deviations in the least significant figure are given in parentheses.

$$^a R_1 = \frac{\sum ||F_o| - |F_c||}{\sum |F_o|}$$

$$^b wR_2 = \left[\frac{\sum [w(F_o^2 - F_c^2)]}{\sum [w(F_o^2)]} \right]^{1/2}$$

$$\text{where } w = 1/[\sigma^2(F_o^2) + (0.2P)^2] \text{ and } P = [F_o^2 + 2F_c^2]/3$$

Table 3.23 Selected ligand bond distance for **11**

Bonds	Distance (Å) [†]	Bonds	Distance (Å) [†]
Fe1—O1	1.947(11)	Fe2—O12	2.050(19)
Fe1—O3	1.982(15)	Fe2—O14	1.965(18)
Fe1—O5	2.017(12)	Fe2—O15	1.987(14)
Fe1—O7	2.075(12)	Fe3—O1	1.903(13)
Fe1—O9	2.008(12)	Fe3—O2	1.953(17)
Fe1—O16	1.996(13)	Fe3—O4	2.072(14)
Fe2—O1	1.926(12)	Fe3—O6	2.085(18)
Fe2—O8	2.070(16)	Fe3—O11	2.043(18)
Fe2—O10	1.961(16)	Fe3—O13	2.018(13)

[†] Estimated standard deviations in the least significant figure are given in parentheses.

Table 3.24 Selected bond angles for **11**

Atoms	Angle (°) [†]
Fe1—O2—Fe3	116.5(15)
Fe2—O1—Fe3	125.4(17)
Fe2—O12—Fe5	100.7(15)
Fe4—O12—Fe2	92.7(13)

[†] Estimated standard deviations in the least significant figure are given in parentheses.

Table 3.25 Bond valence sums for the inorganic oxygen atoms in **11**

Atom	BVS	Assignment
O1	1.80	O ²⁻

[†] The oxygen atom is an O²⁻ if the BVS is ~2, an OH⁻ if the BVS is ~1, and an H₂O if the BVS is ~0.³

3.3 Conclusions

A total of six new iron complexes have been synthesised using bicine. These clusters consist of either six or seven coordinate iron centres. The flexibility of the ligand and its ability to exist in different binding modes showing three different coordination geometries has been illustrated. One of which previously unseen for this ligand. The effects of base have also been illustrated in the isolation of different clusters of higher nuclearity and the effect of base on the ligand. We have highlighted the stability of the products formed from the synthesis of clusters **6-8** and the previously reported Fe_6Bic_6 wheel¹, which was also seen in several reactions. Also we have highlighted the effect of base on the ligand and the importance of the choice of base leading to higher nuclearity species from six iron centres to twelve. The absence of bicine from the final structure arises from an increase in metal:ligand:base ratio 3:1:1 for complex **10** and 3:1:4 for **11** again illustrating further the effects of base. Three of these clusters **6**, **7** and **10** all possess non zero ground states of $S = 3$ or $S = 5$ with **9** having a ground state $S = 0$.

3.4 Future work

Bicine is still a relatively novel ligand to investigate, our work has concentrated on the use of iron oxo-centred triangles, therefore it is still a viable route to explore using other metal centres such as manganese, and nickel. Due to the lack of complexes reported apart from the monomers and 1-D chains mentioned previously, it would be interesting to explore the use of manganese oxo-centred triangles which have been used to produce some interesting clusters using other ligands. Also this work could be extended to nickel. Previous work¹⁵ has used diethanolamine which is structurally similar to bicine to synthesise nickel(II) cubanes. These cubanes have shown SMM behaviour, however hysteresis loops and EPR indicate the presence of interaction between neighbouring cubanes. The presence of an extra arm/binding site could result in new clusters or result in the synthesis of different clusters due to the extra binding site.

Also we focused on reacting mixed metal oxo-centred triangles such as $[\text{Fe}_2\text{CuO}(\text{O}_2\text{CR})_6(\text{H}_2\text{O})_3]$ (where $\text{R} = \text{OAc}$ or O_2CPh) with our ligand. Due to antiferromagnetic interactions within polynuclear iron complexes being common, we tried to incorporate a second d-block metal to provide additional exchange interactions such as Fe–Cu–Fe instead to Fe–Fe. We had hoped this would lead to an overall increase in the spin ground state of clusters synthesised. However this approach led to complexes **6-8** being produced with no copper(II) present in the structure, again highlighting the stability of these complexes.

It may be of interest to synthesise a mixed metal analogue of complex **10** substituting Fe(II) for other M(II) ions such as Mn(II), Ni(II) or Cu(II) using mixed metal triangles, to compare the magnetic properties of the clusters once formed.

3.5 References

- ¹ M. Murugesu, K. A. Abboud, G. Christou; *Dalton. Trans.* **2003**, 4552.
- ² J. K. McCusker, J. B. Vincent, E. A. Schmitt, M. L. Mino, K. Shin, D. K. Coggin, P. M. Hagen, J. C. Huffman, G. Christou, D. N. Hendrickson; *J. Am. Chem. Soc.* **1991**, 113, 8, 3012.
- ³ W. Liu, H. H. Thorp; *Inorg. Chem.* **1993**, 32, 4102.
- ⁴ V. S. Nair, K. S. Hagen; *Inorg. Chem.* **1992**, 31, 4048.
- ⁵ P. S. Ammala, S. R. Batten, J. D. Cashion, C. M. Kepert, B. Moubaraki, K. S. Murray, L. Spiccia, B. O. West; *Inorg. Chim. Acta.* **2002**, 331, 90.
- ⁶ W. Clegg, A. K. Powell, M. J. Ware; *Acta. Cryst. Sec C.* **1984**, C40, 1822.
- ⁷ C. Boskovic, H. U. Gudel, G. Habat, A. Neels, W. Wernsdorfer, B. Moubaraki, K. S. Murray; *Inorg. Chem.* **2005**, 44, 3181.
- ⁸ M. A. Halcrow, W. E. Streib, K. Folting, G. Christou; *Acta. Cryst. Sec C.* **1995**, C51, 1263.
- ⁹ T. C. Stamatos, D. Foguet-Albiol, S. P. Perlepes, C. P. Raptopoulou, A. Terzis, C. S. Patrickios, G. Christou, A. J. Tasiopoulos; *Polyhedron.* **2006**, 25, 1737.
- ¹⁰ I. A. Gass, C. J. Milios, A. G. Whittaker, F. P. A. Fabiani, S. Parsons, M. Murrie, S. P. Perlepes, E. K. Brechin et. al, *Inorg. Chem.* **2006**, 45, 5281.
- ¹¹ Dr S. Piligkos, University of Copenhagen.
- ¹² Cambridge Structural Database; **2008**.
- ¹³ J. Kim, M. Kim, Y. Do; *Eur. J. Inorg. Chem.* **2003**, 25, 63.
- ¹⁴ A. Bino, D. Gibson; *Inorg. Chem.* **1984**, 23, 1, 109.
- ¹⁵ A. Ferguson, Ph. D. Thesis, University of Glasgow, *Synthesis and Characterisation of SMMs*, **2007**.

4.0 Synthesis of Iron Complexes: Tricine (H_4L^3)

We continued our investigation into the synthesis of polynuclear iron complexes using Tricine. Tricine is a mix of two ligands; Bicine which was successfully used in the synthesis of iron complexes in chapter 3 and Bis-Tris which has been successful in linking small iron fragments into larger clusters with unique topologies.¹ In fact, tripodal alcohol ligands have been thoroughly investigated in the synthesis of iron(III) complexes and manganese chemistry resulting in a series of beautiful clusters some of which display SMM behaviour.^{2,3} The tripodal ligand tris, ($H_2NC(CH_2COH)_3$) has previously been studied in both manganese and iron chemistry.⁴ Depending on the metal centre the tris ligand can either cap clusters as seen for manganese⁴ or act as a bridging ligand in which one of the CH_2OH arms remain protonated (figure 4.1).⁴

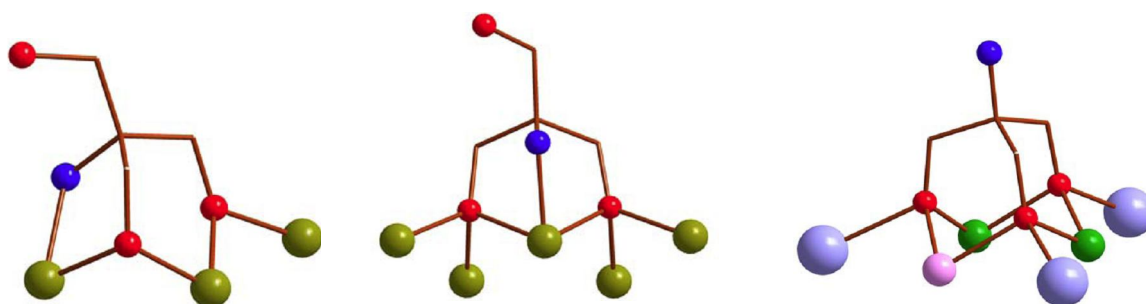


Figure 4.1: Different binding modes for tris depicted for iron and manganese (Ball and stick representation with Fe(III), Gold; Mn(II), Pink; Mn(III), Green; O, Red; N, Blue; C, Brown; Na, Purple).

A small number of complexes are known for tricine ranging from monomeric species of Co, Cd, Zn, Cu and Ni (figure 4.2),⁵ a one dimensional Cu(II) chain⁶ and the dimer $[Sn_2(CH_3)_4(H_2L^3)_2]$.⁷

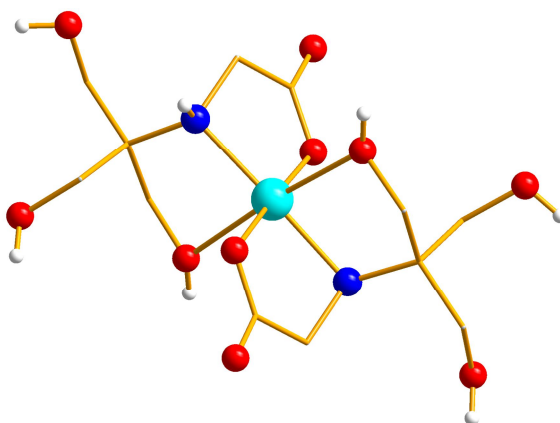


Figure 4.2: Structure of the $[\text{Cu}(\text{H}_3\text{L}^3)_2]$ showing the ligand binding. (ball and stick representation with Cu(II) light blue; O, red; N, blue; C, brown; H atoms white).

The tricine ligand displays the same binding mode for all known monomeric and chain complexes, however the deprotonation of the CH_2OH arm at O3 and O3a results in the formation of the Sn_2 dimer (figure 4.3).

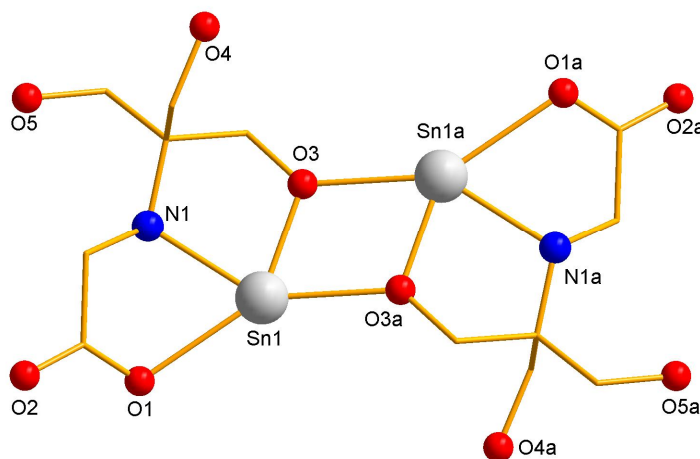


Figure 4.3: Structure of the $[\text{Sn}_2(\text{CH}_3)_4(\text{H}_2\text{L}^3)_2]$ showing the ligand binding. (ball and stick representation with Sn(III) white; O, red; N, blue; C, brown; H atoms and methyl groups are omitted for clarity)[atom suffix a signifies the symmetry equivalent atom: $a = 1 - x, 1 - y, 1 - z$].

Therefore, if full deprotonation of the ligand can be achieved it should be possible to synthesise large polynuclear complexes of iron. We reacted this ligand in the same way to both edte and bicine by using the pre-formed oxo-centred triangles, again altering the base and varying the ratios of reactants. We continued to focus on the same six triangles used for edte, as they were successful in producing unique

and interesting clusters. This approach has resulted in three new iron complexes being produced. The syntheses, structures and magnetic characterisation of these are reported below.

4.1 Synthesis of complexes containing tricine, H_4L^3

4.1.1 Synthesis of $Et_2NH_2[Fe_9O_4(OH)_2(HL^3)_2(phbenz)_{12}] \cdot 5MeCN \cdot H_2O$ ($12 \cdot 5MeCN \cdot H_2O$)

To a stirred solution of $[Fe_3O(phbenz)_6(MeOH)_3][NO_3] \cdot 3MeOH$ (0.5 g, 0.3 mmol) in MeCN (20 ml), H_4L^3 (0.02 g, 0.1 mmol) was added, followed by Et_2NH (0.02 g, 0.3 mmol). The solution was stirred overnight and filtered yielding a dark red filtrate. Small aliquots of solution were used in vapour diffusion of Et_2O . After 3 months small single brown crystals were observed in vapour diffusion experiments in approximately 11% yield. Selected IR data: $\nu = 1581, 1541, 1479, 1396, 1226, 1159, 1097, 881, 746 \text{ cm}^{-1}$. Crystals analyse as $12.6H_2O$ (%) calc. (found) C, 56.93, (56.30); H, 4.20 (3.79); N, 1.14, (1.14).

4.1.2 Synthesis of $[Na_3Fe_7O_4(OH)(H_3L^3)_2(phbenz)_{11}(H_2O)_2] \cdot 4H_2O$ ($13 \cdot 4H_2O$)

To a stirred solution of $[Fe_3O(phbenz)_6(MeOH)_3][NO_3] \cdot 3MeOH$ (0.5 g, 0.3 mmol) in MeCN (20 ml), H_4L^3 (0.05 g, 0.3 mmol) was added, followed by NaOMe (0.05 g, 0.9 mmol). The solution was stirred overnight and filtered yielding a dark brown filtrate. Small aliquots of solution were used in vapour diffusion of Et_2O . After 1 month, small brown single crystals were observed in vapour diffusion experiments in approximately 4%. Selected IR data: $\nu = 1580, 1536, 1479, 1396, 1223, 1159, 1095, 1021, 880, 748, 648 \text{ cm}^{-1}$. Elemental analysis was not obtained for this complex due to lack of sample.

4.1.3 Synthesis of $[\text{NaFe}_{11}\text{O}_6(\text{OH})_6(\text{phbenz})_{15}][\text{OMe}]$ (**14**)

To a stirred solution of $[\text{Fe}_3\text{O}(\text{phbenz})_6(\text{MeOH})_3][\text{NO}_3] \cdot 3\text{MeOH}$ (0.5 g, 0.3 mmol) in MeCN (20 ml), H_4L^3 (0.05 g, 0.3 mmol) was added, followed by NaOMe (0.05 g, 0.9 mmol). The solution was stirred for 30 minutes and placed in a sealed Teflon container. The container was placed in an oven and heated to 150°C over 5 minutes. The oven temperature was held at 150°C for 12h. After 12h, the solution was allowed to cool to room temp inside the oven. X-ray quality crystals appeared on opening the MeCN solution, in approximately 15% yield. Selected IR data: $\nu = 1582, 1480, 1396, 1226, 1159, 1096, 1022, 881, 779, 689, 648 \text{ cm}^{-1}$. Crystals analyse as **14**. (%) calc. (found) C, 57.92, (57.59); H, 3.57 (3.33).

4.2 Complexes containing Tricine, H_4L^3

4.2.1 Discussion of crystal structure of

$[\text{Et}_2\text{NH}_2][\text{Fe}_9\text{O}_4(\text{OH})_2(\text{HL}^3)_2(\text{phbenz})_{12}] \cdot 5\text{MeCN} \cdot \text{H}_2\text{O}$ (**12**·5MeCN·H₂O)

Complex **12** is a nonanuclear Fe(III) complex which crystallises in the monoclinic space group $P2_1/c$ (figure 4.4).

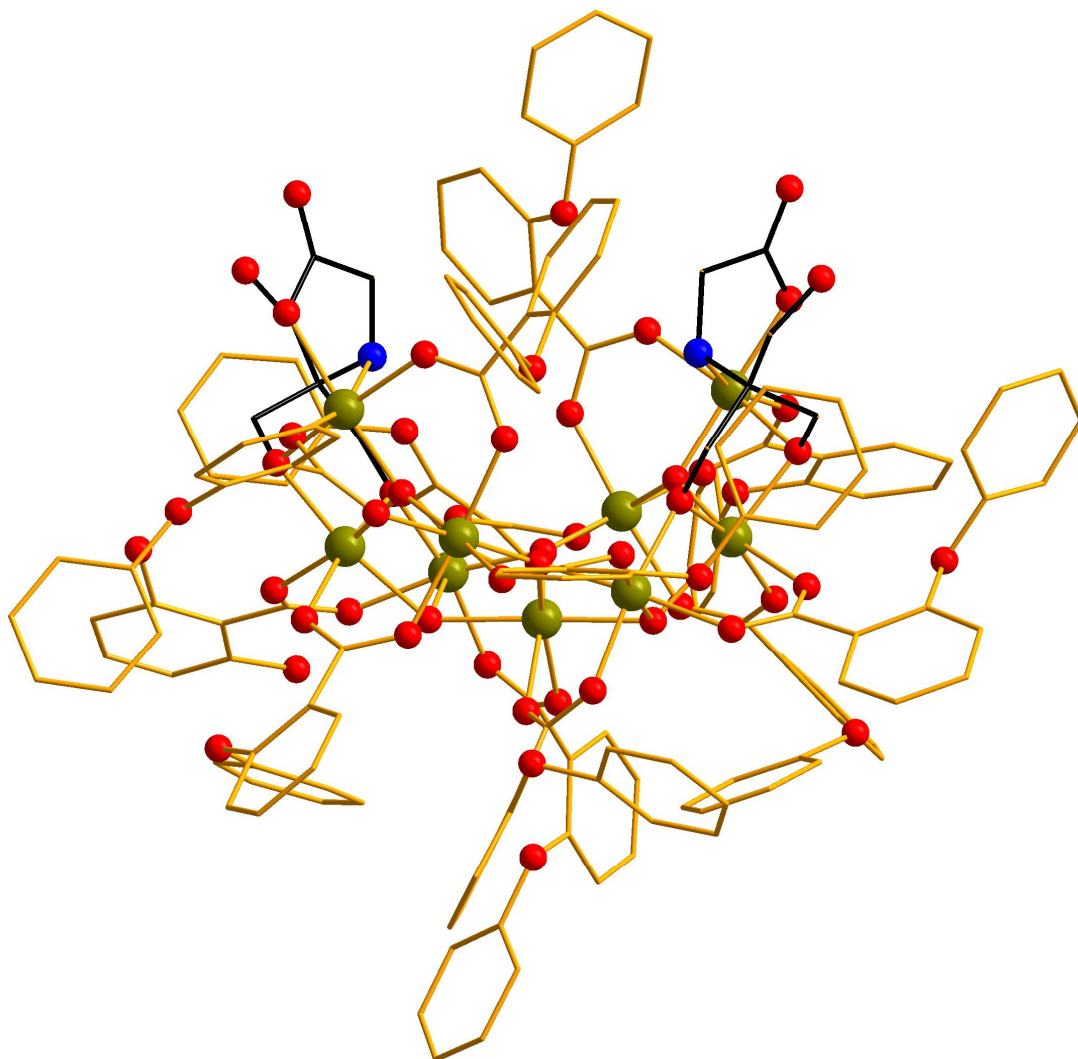


Figure 4.4: Structure of the anion of **12** (ball and stick representation with Fe(III)
Gold; O, Red; N, Blue; C, Brown; H atoms are omitted for clarity)

The boat like structure of **12**, can be described two fused distorted butterfly $[\text{Fe}_4\text{O}(\text{OH})]^{9+}$ units capped by an $[\text{Fe1}(\text{HL}^3)]$ unit on either side (figure 4.5 where the atom suffix a signifies symmetry equivalents).

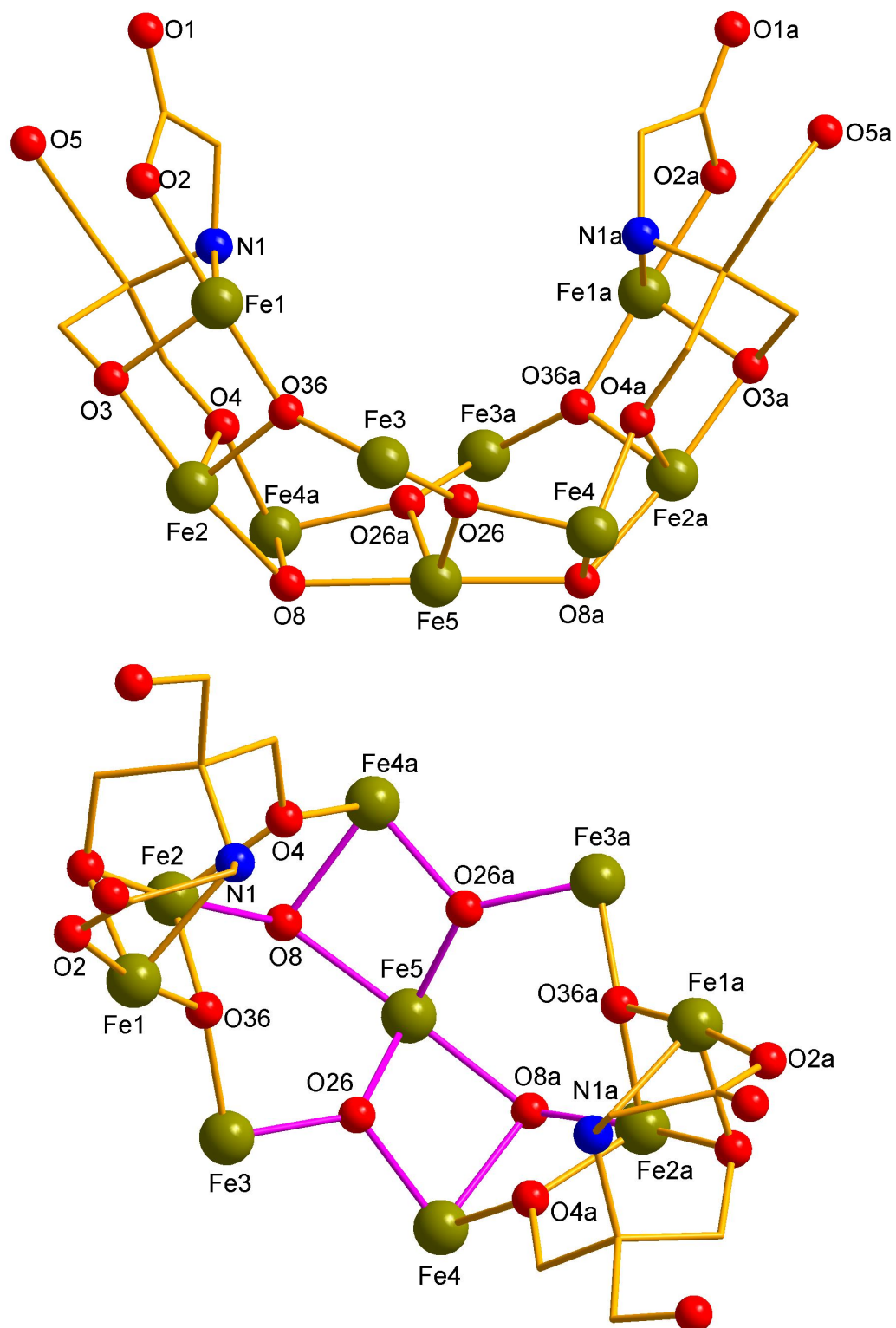


Figure 4.5 top: displaying the boat like core of **12**; [atom suffix a signifies the symmetry equivalent atom: a = 1 _ x, 1 _ y, 1 _ z].

The two distorted butterflies in the central core ([Fe2a, Fe4, Fe3] and symmetry equivalents), share a body Fe ion (Fe5) through four oxygen atoms: two O²⁻ atoms (O26/O26a) and two OH⁻ ions (O8/O8a), forming a distorted central [Fe₇O₂(OH)₂]¹⁵⁺ unit. Another two O²⁻ atoms (O36/O36a) binds Fe1 to Fe2 and Fe3 of the fused distorted butterfly core. The complex contains one independent tricine ligand which displays a new binding mode (figure 4.6). The ligand is tri-deprotonated binding to Fe1 at N1. The carboxylate group binds monodentate at O2, whereas two of the tris unit CH₂O⁻ arms are bidentate, bridging Fe1 to Fe2 via O3 and Fe2 to Fe4a via O4. The remaining ligand arm is protonated and unbound, hydrogen bonded to the carboxylate of the tricine ligand (O1) on an adjacent cluster.

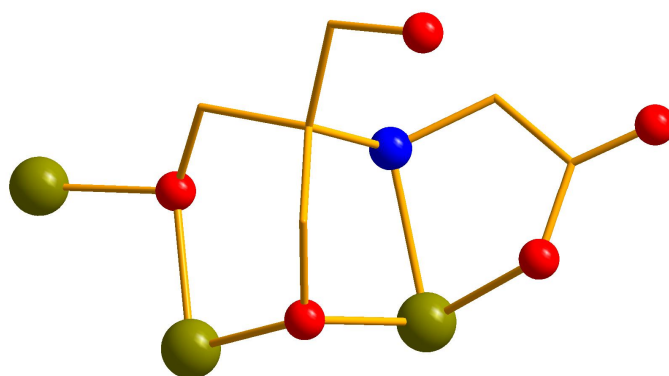


Figure 4.6: binding mode of HL³ found in **12**

The twelve phbenz ligands bind in a typical 1, 3 bridging mode completing the octahedral geometry of all the iron centres. Finally the cation Et₂NH₂⁺ is located between adjacent clusters, hydrogen bonded to O2 and O1a of the adjacent molecules.

A small number of nonanuclear iron clusters exist that display SMM behaviour⁸ however the closest example to **12** is [Fe₉O₄(O₂CCMe₃)₁₃(thme)₂]² which incorporates the tripodal ligand thme (MeC(CH₂OH)₃). The rhomb-like cluster displays the same fused butterfly core with the thme ligands located above and below the core resulting in a planar cluster (figure 4.7).

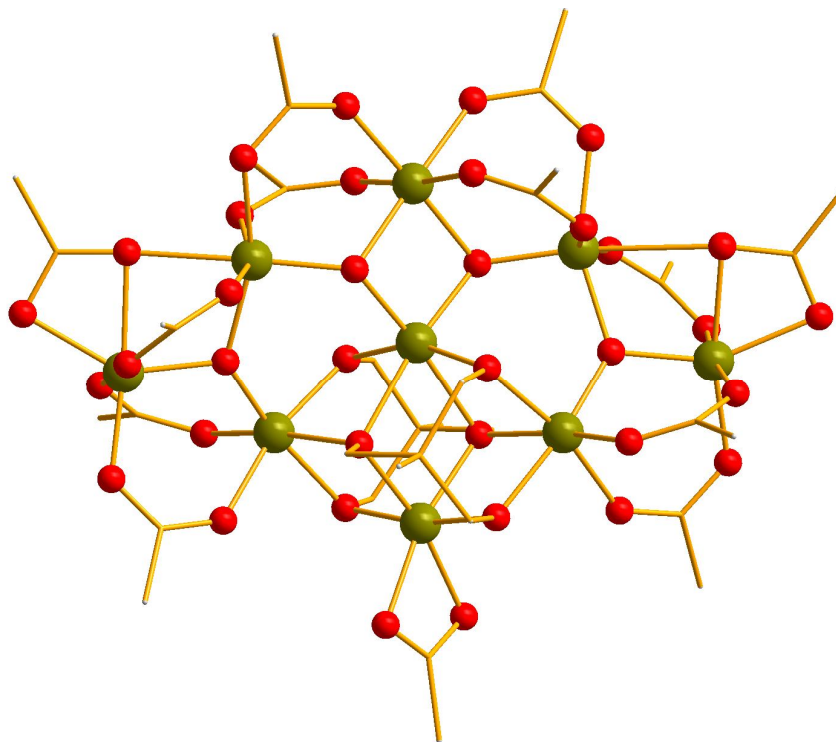


Figure 4.7: Structure of $[\text{Fe}_9\text{O}_4(\text{O}_2\text{CCMe}_3)_{13}(\text{thme})_2]^{2-}$ (ball and stick representation with Fe(III) gold; O, red; N, blue; C, brown; H atoms and methyl groups are omitted for clarity)

The boat-shaped core of **12** appears to be directed by the ligand geometry due to the flexibility of the carboxylate arm, which once coordinated restricts the binding of the tris unit of the tricine ligand. As a result only two arms coordinate and 'pull' the Fe2 and Fe2a centre away from the plane resulting in the boat shaped core of **12**.

Table 4.1 Data for the crystal structure determination of **12**

Empirical formula	C ₁₇₂ H ₁₅₄ N ₃ O ₅₈ Fe ₉
fw(gmol ⁻¹)	3693.75
Spacegroup	<i>P</i> 2 ₁ / <i>c</i>
<i>a</i> (Å)	24.5836(5)
<i>b</i> (Å)	23.4043(4)
<i>c</i> (Å)	32.2296(5)
β(deg)	108.2720(10)
<i>V</i> (Å ³)	17608.7
<i>Z</i>	6
<i>T</i> (K)	100(2)
λ(Å)	0.71073
ρ _{calcd} (Mg/m ³)	1.466
μ(mm ⁻¹)	1.232
R ₁ (%)	5.22
wR ₂ (%)	12.57
Goodness of fit indicator	0.784

[†]Estimated standard deviations in the least significant figure are given in parentheses.

$${}^a R_1 = \frac{\sum ||F_o| - |F_c||}{\sum |F_o|}$$

$${}^b wR_2 = \left[\frac{\sum [w(F_o^2 - F_c^2)]}{\sum [w(F_o^2)]} \right]^{1/2}$$

where $w = 1/[\sigma^2(F_o^2) + (0.2P)^2]$ and $P = [F_o^2 + 2F_c^2]/3$

Table 4.2 Selected ligand bond distances for **12**

Bonds	Distance (Å)	Bonds	Distance (Å)
Fe1—N1	2.224(8)	Fe2—O3	2.004(6)
Fe1—O2	2.048(7)	Fe2—O8	2.101(6)
Fe1—O3	2.006(6)	Fe8—O8	2.111(6)

Table 4.3 Selected bond angles for **12**

Atoms	Angle (°) [†]	Atoms	Angle (°) [†]
Fe1–O3–Fe2	94.99(3)	Fe4a–O26a–Fe5	100.70(3)
Fe2–O4–Fe4a	102.29(3)	Fe5–O26–Fe4	101.25(3)
Fe4a–O8–Fe5	89.88(2)	Fe5–O8a–Fe4	90.73(2)

[†] Estimated standard deviations in the least significant figure are given in parentheses.

Table 4.4 Bond valence sums for the inorganic oxygen atoms in **12**

Atom	BVS	Assignment
O8	1.06	OH ⁻
O26	1.78	O ²⁻
O36	1.94	O ²⁻

The oxygen atom is an O²⁻ if the BVS is ~2, an OH⁻ if the BVS is ~1, and an H₂O if the BVS is ~0⁹

4.2.1.1 Magnetic Susceptibility Measurements for **12**

Magnetic susceptibility measurements were carried out on an air-dried sample. For **12** the value of χT at 300K is 20.6 cm³ mol⁻¹ K, again significantly lower than for nine uncoupled Fe(III) ions (39.4 cm³ mol⁻¹ K for $g=2$), indicating the presence of strong antiferromagnetic interactions between the Fe(III) centres (figure 4.8).

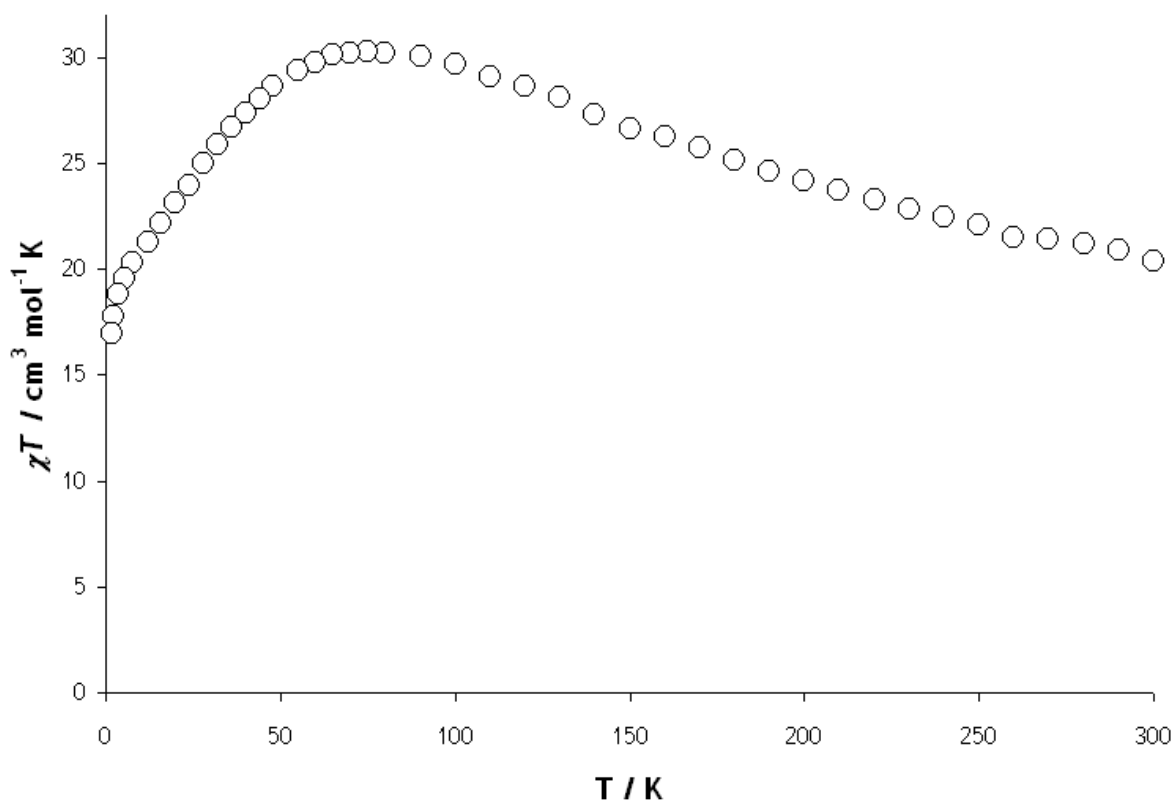


Figure 4.8: Temperature dependence of χT for **12** from 300-1.8 K measured in a field of 1 kOe

The value of χT increases steadily to a maximum of $30.2 \text{ cm}^3 \text{ mol}^{-1} \text{ K}$ at 75 K, then drops steadily to $17.1 \text{ cm}^3 \text{ mol}^{-1} \text{ K}$ at 1.8 K. This gives an indication of competing ferromagnetic and antiferromagnetic interactions within the cluster. The magnetisation was measured as a function of applied field at 2 K, the curve does not reach saturation, rising to a value of $M/N\beta=11.9$ at 5 T (figure 4.9).

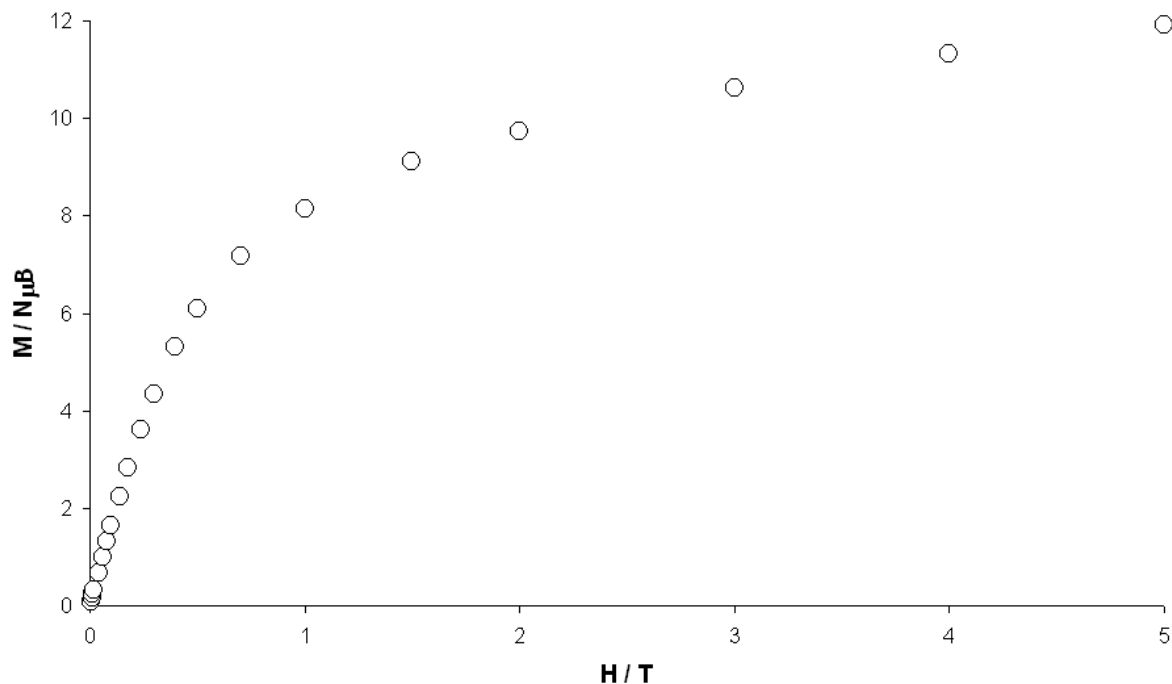


Figure 4.9: magnetisation versus field at 2 K for **12**

Both the low temperature maximum in χT and the magnetization data are consistent with a spin ground state of $S = 11/2$ for **12**.

In order to determine the zero-field splitting parameter D and confirm the spin ground-state for **12**, magnetisation data were collected in the ranges 5-20 kG and 5-7 K (figure 4.10). The data were fit by a matrix diagonalization method using the program MAGMOFIT to a model that assumes only the ground state is populated, includes axial zero-field splitting ($D\hat{S}_z^2$) and the Zeeman interaction, and carries out a full powder average.¹⁰ The corresponding Hamiltonian is given by *Equation 4.1*.

$$\hat{H} = D\hat{S}_z^2 + g\mu_B\mu_0\hat{S}H$$

Equation 4.1

Where D is the axial anisotropy, μ_B is the Bohr magneton, μ_0 is the vacuum permeability, \hat{S}_z is the easy-axis spin operator, and H_z is the applied field. $S = 11/2$ with $g = 2.10$ and $D = 0.41 \text{ cm}^{-1}$.

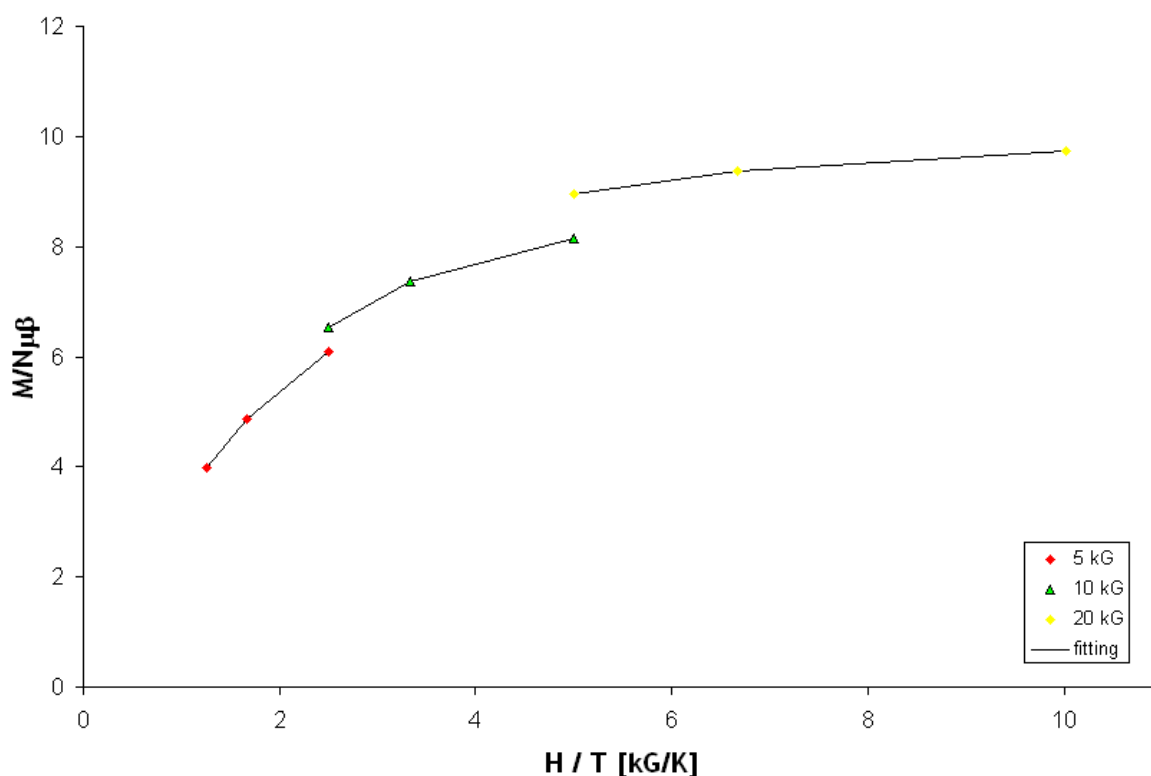


Figure 4.10: magnetisation data collected in the ranges 5-20 kG and 5-7 K

Ac susceptibility measurements were also carried out for **12**, however there was no increase in the χ'' signal down to 1.8 K for any of the frequencies measured. This suggests that the Fe_9 cluster shows no slow relaxation of magnetization down to 1.8 K. If the value of D is correct then **12** is not an SMM. Further magnetic measurements to lower temperature and EPR are needed to confirm the correct value and sign of D .

4.2.2 Discussion of crystal structure of

$[\text{Na}_3\text{Fe}_7\text{O}_4(\text{OH})(\text{H}_2\text{L}^3)_2(\text{phbenz})_{11}(\text{H}_2\text{O})_2] \cdot 4\text{H}_2\text{O}$ (**13**·4H₂O)

Complex **13**·4H₂O is a heptanuclear Fe(III) complex which crystallises in the triclinic space group $P-1$ (figure 4.11).

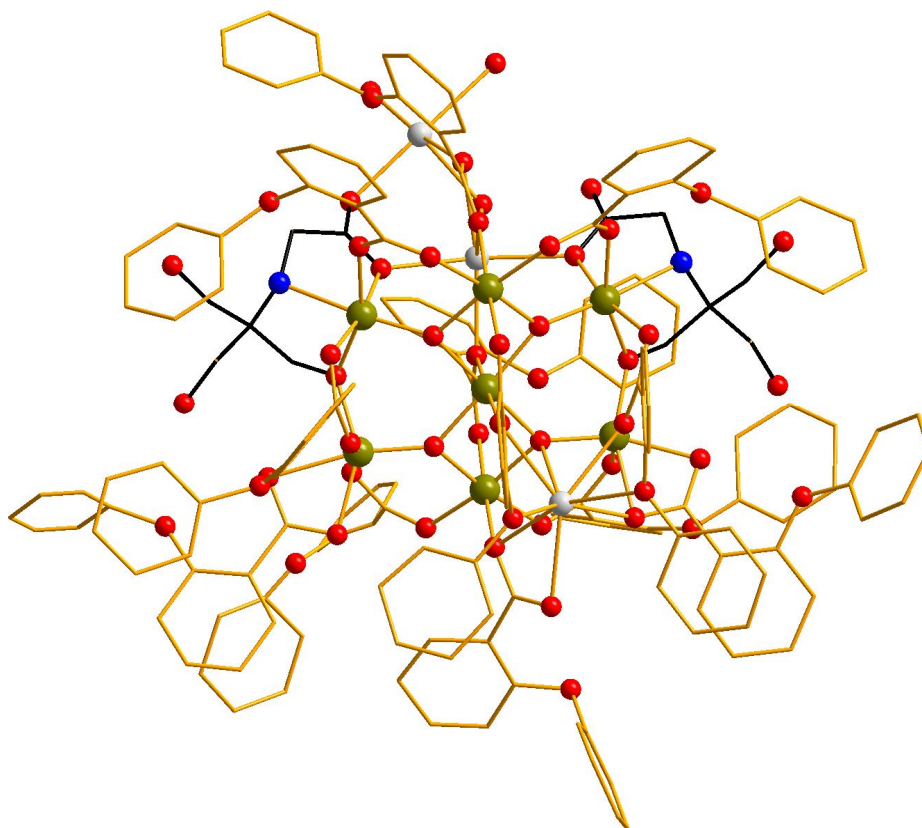


Figure 4.11: Structure of **13** (ball and stick representation with Fe(III) gold; O, red; N, blue; C, brown; Na, white; H atoms are omitted for clarity)

A change of base from Et_2NH to NaOMe has resulted in the substitution of three Na^+ ions into the final structure. As for complex **12**, **13** also is composed of the similar fused butterfly, the major difference being the core is less strained due to the absence of two Fe atoms bound at O2 and O37 as seen for the previous cluster (Fe1 bound at O2, figure 4.12).

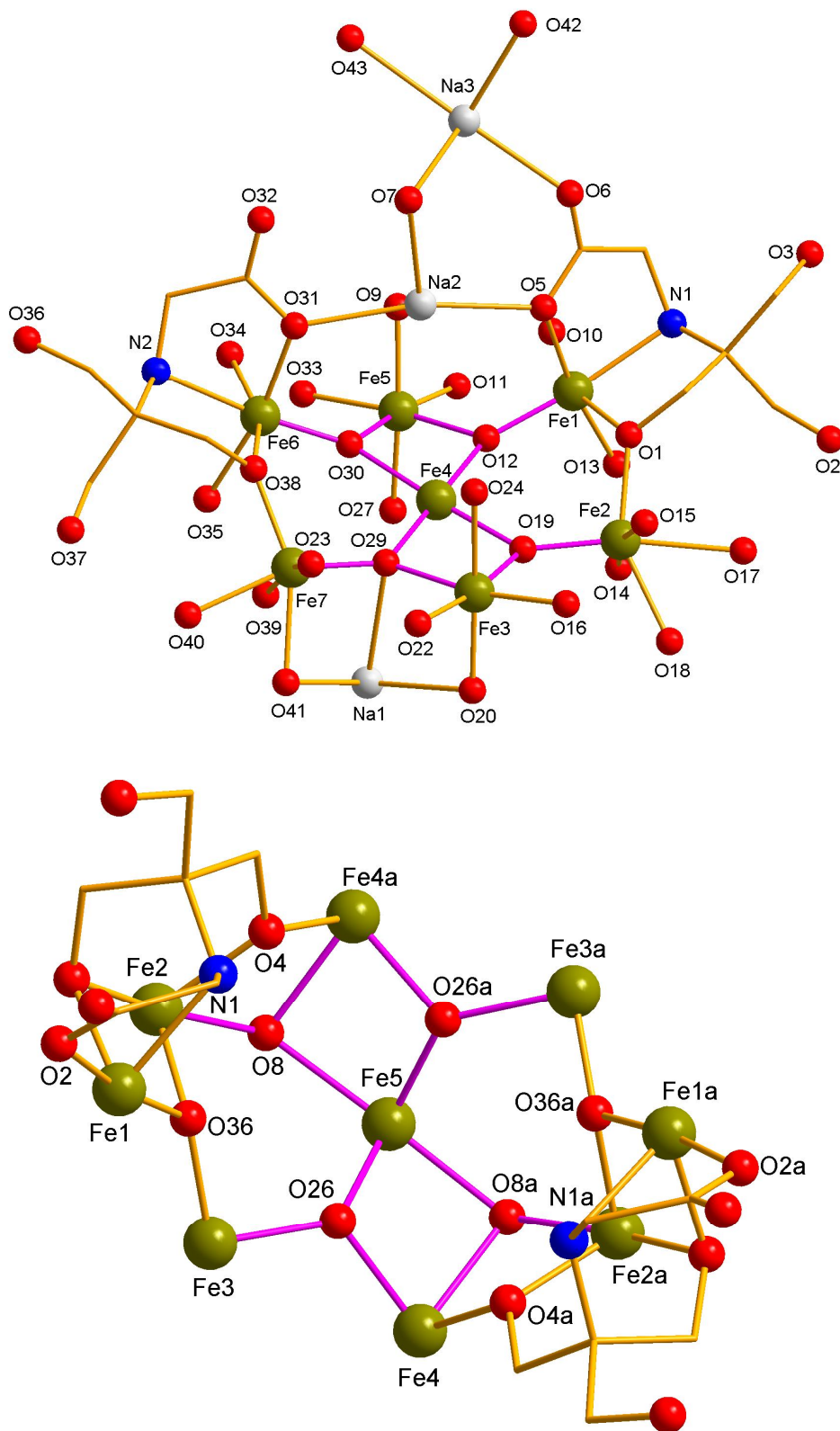


Figure 4.12 Top: The planar fused core of **13**
Bottom: The distorted fused core of **12** for comparison

The tricine ligands (figure 4.13), are doubly deprotonated binding to Fe1 through N1 and Fe6 through N2. The carboxylate arm exists in two binding modes, the deprotonated arm O5 and O31 binds between Fe1/Na2 and Fe6/Na2 respectively. O32 is hydrogen bonded to O36 on a neighbouring cluster whereas O6 binds monodentate to Na3. O32 is hydrogen bonded to O36 on a neighbouring cluster whereas O6 binds monodentate to Na3. One of the three CH₂OH arms of each ligand (O1 and O38) is deprotonated and bridges bidentate between Fe1/Fe2, (O1) and Fe6/Fe7 (O38). The remaining two arms of each ligand are protonated; O3 is hydrogen bonded to the carboxylate O6 of a neighbouring cluster and O2 to water molecule O42 of a neighbouring cluster. O36 is hydrogen bonded to O32 of a neighbouring cluster and O37 remains protonated and unbound. The two butterfly units in the core ([Fe2, Fe3, Fe2a] and [Fe1, Fe5, Fe1a]) share a body iron(III) centre Fe4, through four oxide atoms forming a almost planar central [Fe₇O₄]¹³⁺. Three of the oxides are μ_3 (O12, O12a and O19) and the final is μ_4 due to coordination of the Na1 atom. The only hydroxide ligand, (O7), is bound bidentate between Na1 and Na2.^{11,12}

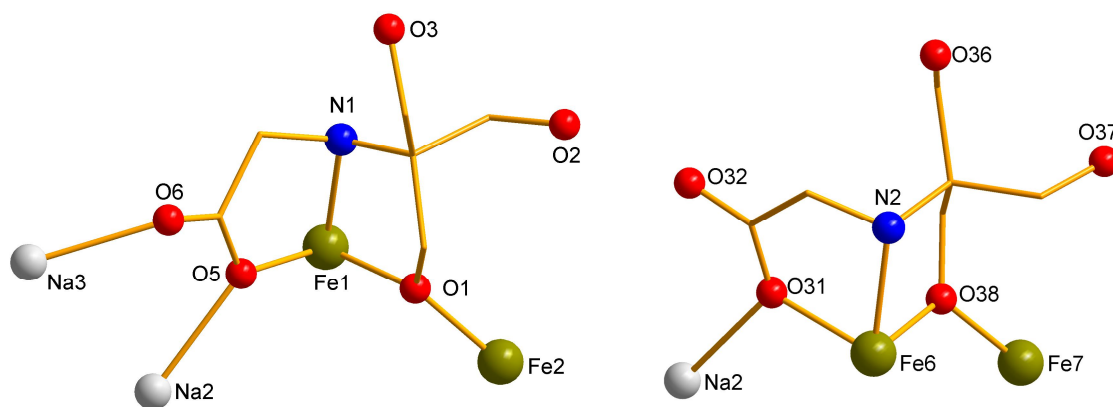


Figure 4.13: The different ligand binding modes observed in **13**.

Five of the eleven phbenz ligands bind η^1, η^1, μ_2 , another ligand η^1, η^1, μ_1 binding only to Fe centres. The final five ligands bind both Fe and Na atoms; two of these ligands bind $\eta^1, \eta^2, \eta^1, \mu_3$ with extra coordination of the Na atom being provided by the phenoxy group of the phbenz ligand. The final three ligands are present in $\eta^2, \eta^2, \mu_3; \eta^2, \eta^2, \mu_3$ and η^1, η^2, μ_2 binding modes (figure 4.14).

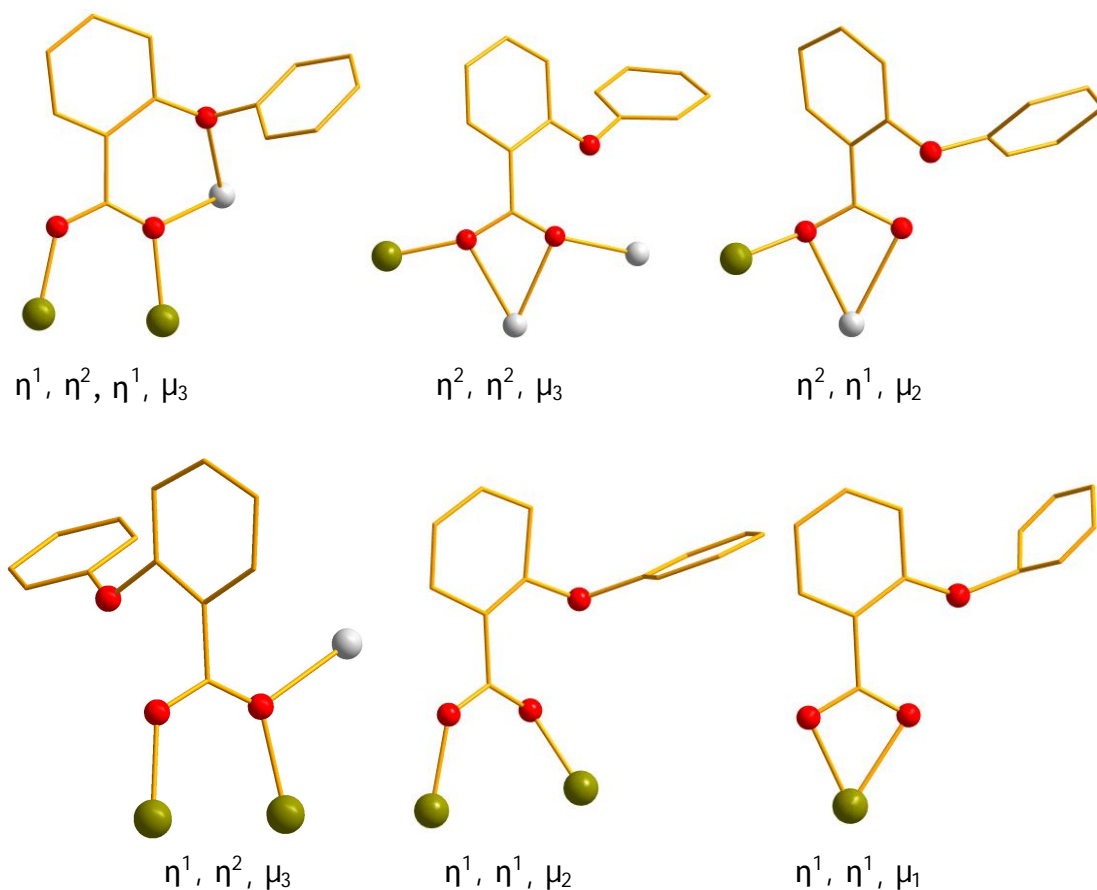


Figure 4.14: the different binding modes of phbenz found in **13**

All iron centres are six-coordinate, displaying distorted octahedral geometries.

The fused butterfly core has been observed in complexes of nuclearity nine, eleven and sixteen,² however for Fe₇ complexes this core is rare. Some do exist but not strictly fused as for **13**; three iso-structural complexes of the general formula $[\text{Fe}^{\text{III}}_7(\mu_3\text{-O})_3(\text{L})_3(\mu\text{-O}_2\text{CCMe}_3)_6(\eta^1\text{-O}_2\text{CCMe}_3)_3(\text{H}_2\text{O})_3]$,¹³ (where L is defined as di- or triethanolamine), two clusters which display a millennium dome topology,¹⁴ and a further two disc-like heptanuclear wheels (figure 4.15).¹⁵

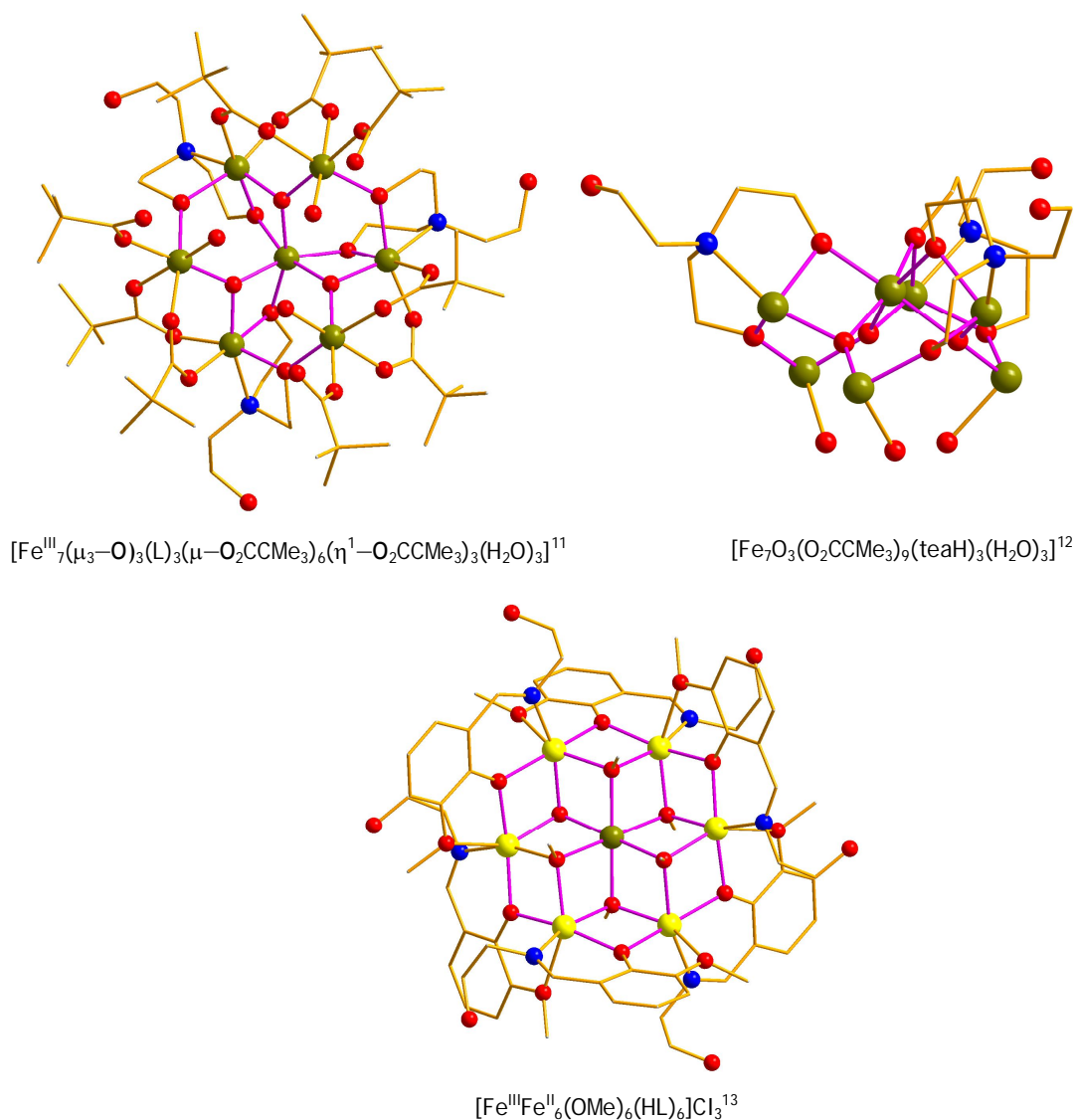


Figure 4.15: structures of different Fe_7 topologies (ball and stick representation with Fe(III) gold; Fe(II), yellow; O, red; N, blue; C, brown; H atoms and Cl atoms are omitted for clarity. Pivalate groups of $[\text{Fe}_7\text{O}_3(\text{O}_2\text{CCMe}_3)_9(\text{teaH})_3(\text{H}_2\text{O})_3]$ have been omitted for clarity).

The difference in the topologies of our cluster and the known Fe^{III}_7 clusters can be attributed to the distorted octahedral geometry of the central Fe atom of the Fe^{III}_7 clusters compared with the octahedral coordination of Fe4 for **13**. Magnetic characterisation and further analysis of **13** was not obtained due to poor yield of sample. The synthesis was not reproducible, therefore, improving the synthesis of

this complex is the first step to determining the magnetic properties of **13**. The Fe₇ clusters mentioned display either $S = 5/2$ or $S = 0$ ground states however this cannot predict what S will be for our cluster.

Table 4.5 Data for the crystal structure determination of **13**

Empirical formula	C ₁₅₅ H ₁₃₄ N ₂ O ₅₅ Fe ₇ Na ₃
fw(gmol ⁻¹)	3364.68
Spacegroup	<i>P</i> -1
<i>a</i> (Å)	19.267(8)
<i>b</i> (Å)	19.675(9)
<i>c</i> (Å)	25.767(12)
α (deg)	80.687(2)
β (deg)	75.269(2)
γ (deg)	76.414(2)
<i>V</i> (Å ³)	9128.49
<i>Z</i>	4
<i>T</i> (K)	100(2)
λ (Å)	0.71073
ρ_{calcd} (Mg/m ³)	1.289
μ (mm ⁻¹)	0.628
<i>R</i> ₁ (%)	15.47
<i>wR</i> ₂ (%)	19.73
Goodness of fit indicator	1.105

[†]Estimated standard deviations in the least significant figure are given in parentheses.

$$^a R_1 = \frac{\sum ||F_o| - |F_c||}{\sum |F_o|}$$

$$^b wR_2 = \left[\frac{\sum [w(F_o^2 - F_c^2)]}{\sum [w(F_o^2)]} \right]^{1/2}$$

where $w = 1/[\sigma^2(F_o^2) + (0.2P)^2]$ and $P = [F_o^2 + 2F_c^2]/3$

Table 4.6 Selected ligand bond distances for **13**

Bonds	Distance (Å) [†]	Bonds	Distance (Å) [†]
-------	---------------------------	-------	---------------------------

Fe1–N1	2.210(11)	Fe6–N2	2.236(12)
Fe1–O1	1.990(9)	Fe6–O31	2.045(9)
Fe1–O5	2.049(9)	Fe6–O38	1.999(11)

[†] Estimated standard deviations in the least significant figure are given in parentheses.

Table 4.7 Selected bond angles for **13**

Atoms	Angle (°) [†]	Atoms	Angle (°) [†]
Fe1–O1–Fe2	120.2(4)	Fe5–O12–Fe4	95.54(4)
Fe1–O5–Na2	118.86(4)	Fe5–O30–Fe4	93.91(4)
Fe4–O19–Fe3	96.21(4)	Fe6–O31–Na2	95.54(4)
Fe4–O29–Fe3	95.3(4)	Fe6–O38–Fe7	120.41(5)

[†] Estimated standard deviations in the least significant figure are given in parentheses.

Table 4.8 Bond valence sums for the inorganic oxygen atoms in **13**

Atom	BVS	Assignment
O12	1.89	O ²⁻
O19	1.91	O ²⁻
O29	2.06	O ²⁻
O30	1.85	O ²⁻

[†] The oxygen atom is an O²⁻ if the BVS is ~2, an OH⁻ if the BVS is ~1, and an H₂O if the BVS is ~0⁹

4.2.3 Discussion of crystal structure of [NaFe₁₁O₆(OH)₆(phbenz)₁₅][OMe] (**14**)

Following from the synthesis of **13**, we explored different routes to improve both the quality of the crystals and the yield of product. Solvothermal synthesis has been shown to improve the yield of [Fe₁₄O₆(bta)₆(OMe)₁₈Cl₆],¹⁶ (bta is benzotriazole). Therefore we tried to employ this strategy in order to improve the yield and quality of **13**, which resulted in the synthesis of **14**, an undecanuclear complex that crystallises in the trigonal space group *P*3₁*c* (figure 4.16).

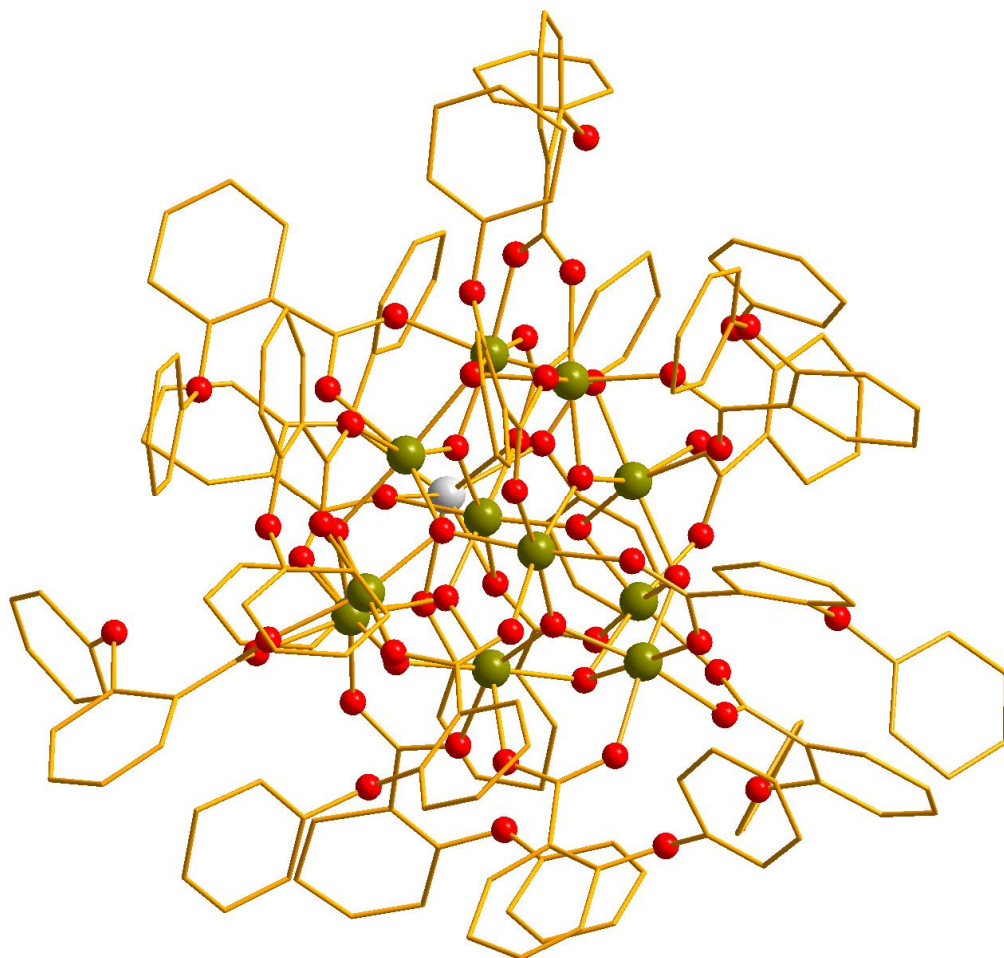


Figure 4.16: Structure of the cation of **14** (ball and stick representation with Fe(III) gold; O, red; N, blue; C, brown; Na, white; H atoms are omitted for clarity)

The core can be described as a twisted trigonal prism (Fe2/Fe4, Fe2a/Fe4a, Fe2b and Fe4b) with two iron atoms capping the triangular faces (Fe1 and Fe5) and a further three iron atoms (Fe3, Fe3a and Fe3b) capping the rectangular faces (figure 4.17 where the atom suffix a, b and c signify symmetry equivalents).

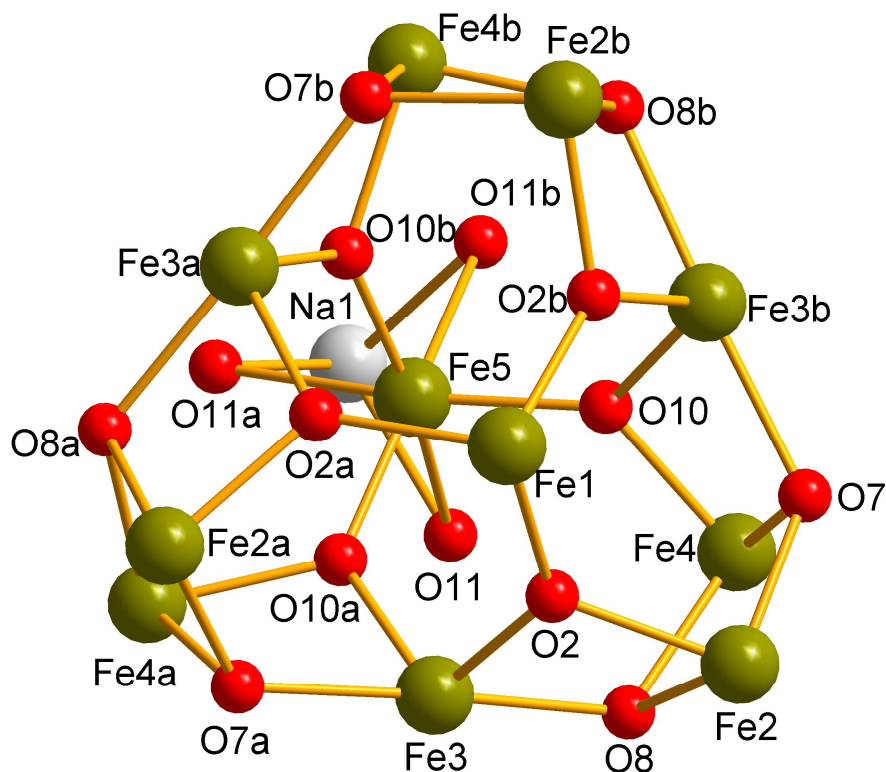


Figure 4.17: The distorted trigonal prism core of **14**.

The iron centres are bound by six μ_3 -oxide ions (O2, O10 and s.e) located within the polyhedron, and a further six μ_3 -hydroxide ions (O7, O8 and s.e) forming the rectangular faces of the cluster. All iron centres display six-coordinate octahedral geometry. The fifteen phbenz ligands complete the coordination sphere of each of Fe(III) centres. Thirteen of the phbenz ligands bind in typical 1,3 bridging, the remaining three ligands are coordinated to Na1 and display the $\eta^1, \eta^2, \eta^1 \mu_3$ binding mode previously seen for **13** (figure 4.14). The remaining charge is balanced by deprotonated methanol solvent in the lattice. This type of charge balance has been observed for $\text{Na}_5[\text{Co}(\text{PhC}(\text{O})=\text{N}(\text{O}))_3]\text{Br} \cdot \text{CH}_3\text{O} \cdot 3\text{CH}_3\text{OH} \cdot 10.5\text{H}_2\text{O}$, where the CH_3O^- ion is hydrogen bonded to three water molecules.¹⁷ The tricline ligand has failed to incorporate into the final structure of **14** indicating solvothermal synthesis is not the correct way to proceed with improving the yield and quality of **13**. Complex **14** is not unusual in iron chemistry, the Fe–O core has been observed for many different carboxylates¹⁸ however none of these contain phbenz as the ligand. These

complexes have been prepared from either high temperature synthesis such as refluxing, or simple bench top reaction of metal salts and carboxylates followed by vapour diffusion. These complexes have been characterised as having small non-zero ground states. None of the known clusters have been synthesised using solvothermal synthesis, phbenz or NaOMe in their reaction. The extra coordination sites provided by the phenoxy groups of the phbenz ligands result in the coordination of the Na ion at O11.

Table 4.9 Data for the crystal structure determination of **14**

Empirical formula	C ₁₄₄ H ₁₀₈ O ₄₆ Fe ₁₁ Na
fw(gmol ⁻¹)	3211.75
Spacegroup	<i>P</i> 3 ₁ <i>C</i>
<i>a</i> (Å)	19.114(7)
<i>c</i> (Å)	31.188(3)
γ (deg)	120
<i>V</i> (Å ³)	9868(9)
<i>Z</i>	2
<i>T</i> (K)	100(2)
λ (Å)	0.71073
ρ_{calcd} (Mg/m ³)	1.365
μ (mm ⁻¹)	0.866
<i>R</i> ₁ (%)	6.55
<i>wR</i> ₂ (%)	17.91
Goodness of fit indicator	0.916

[†]Estimated standard deviations in the least significant figure are given in parentheses.

$${}^a R_1 = \frac{\sum ||F_o| - |F_c||}{\sum |F_o|}$$

$${}^b wR_2 = \left[\frac{\sum [w(F_o^2 - F_c^2)]}{\sum [w(F_o^2)]} \right]^{1/2}$$

$$\text{where } w = 1/[\sigma^2(F_o^2) + (0.2P)^2] \text{ and } P = [F_o^2 + 2F_c^2]/3$$

Table 4.10 Selected bond distance for **14**

Bonds	Distance (Å)	Bonds	Distance (Å)
Fe1–O2	1.934(13)	Fe2–O8	2.165(12)
Fe2–O2	1.905(13)	Fe3–O8	2.036(14)
Fe3–O2	1.914(12)	Fe4–O8	2.109(14)
Fe2–O7	2.110(14)	Fe3b–O10	1.964(12)
Fe3–O7	2.043(15)	Fe4–O10	1.890(14)
Fe4–O7	1.916(14)	Fe5–O10	1.912(12)

Table 4.11 Selected bond angles for **14**

Atoms	Angle (°) [†]	Atoms	Angle (°) [†]
Fe1–O2–Fe2	123.52(6)	Fe2–O8–Fe3	92.40(5)
Fe1–O2–Fe3	130.51(7)	Fe2–O8–Fe4	92.87(5)
Fe2–O2–Fe3	105.78(6)	Fe3–O8–Fe4	126.48(6)
Fe2–O7–Fe3b	98.49(6)	Fe3b–O10–Fe4	101.54(6)
Fe2–O7–Fe4	127.77(7)	Fe3b–O10–Fe5	130.86(7)
Fe3b–O7–Fe4	91.92(6)	Fe4–O10–Fe5	126.29(6)

[†] Estimated standard deviations in the least significant figure are given in parentheses.

Table 4.12 Bond valence sums for the inorganic oxygen atoms in **14**

Atom	BVS	Assignment
O2	1.84	O ²⁻
O7	1.32	OH ⁻
O8	1.11	OH ⁻
O10	1.79	O ²⁻

* The oxygen atom is an O²⁻ if the BVS is ~2, an OH⁻ if the BVS is ~1, and an H₂O if the BVS is ~0⁹

4.3 Conclusions

The use of tricine ligand has been successful in the synthesis of two new polymetallic species. One of these has been characterised as having an $S = 11/2$ ground state. Both clusters show unique Fe–O topologies with the ligand displaying a new binding mode in **12** not seen for any transition metal. From our work we have found that tricine only forms complexes in the presence of the phbenz carboxylate. The fact only two complexes were synthesised by using the same experimental techniques for the previous iron clusters, indicates this ligand is not a good candidate for the synthesis of large polymetallic species. Although the ligand possesses four flexible arms, a maximum of three are found to coordinate to Fe(III). If we compare the tricine ligand to bicine, where all three arms are capable of coordination we can see tricine is more restricted due to the central carbon atom of the tris unit. The binding potential of tricine is restricted further once the carboxylate arm is coordinated to the metal centre.

The ligand was also reacted with manganese salts. Only one reaction crystallised (in 2% yield). Although X-ray diffraction data was poor, we were able to observe the core of the cluster and the ligand binding. This core is similar to a $[\text{Mn}_4^{\text{III}}\text{Mn}_2^{\text{II}}\text{Na}_4\text{O}(\text{L})_4(\text{OAc})_6(\text{MeOH})_2]_n$ (where L is $\text{H}_2\text{N}(\text{CH}_2\text{OH})_3$) which uses tris as the co-ligand (figure 4.18).⁴

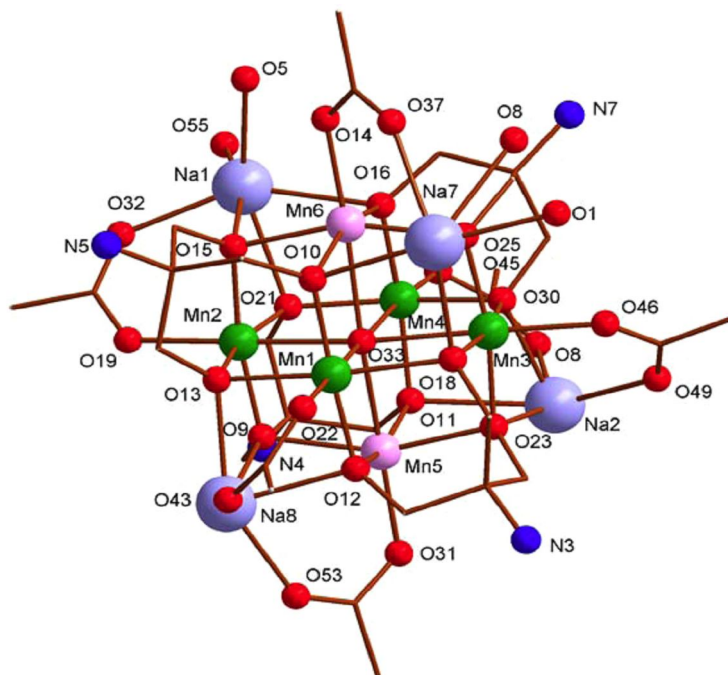


Figure 4.18: structure of $[\text{Mn}_4^{\text{III}}\text{Mn}_2^{\text{II}}\text{Na}_4\text{O}(\text{L})_4(\text{OAc})_6(\text{MeOH})_2]_n$.⁴ Ball and stick representation with Mn(II), Pink; Mn(III), Green; O, Red; N, blue; Na, Purple. H atoms are omitted for clarity.

The tricine ligand binds in the same capping fashion as tris with the carboxylate ligand remaining unbound.

4.4 Future work

The main priority would be to focus on improving the current synthesis of **13**. Solvothermal techniques were used but gave compound **14** however it may be possible to try microwave synthesis¹⁹ which has been used successfully when solvothermal techniques have failed.

We could extend our work with tricine to other metal(III) centres such as Chromium(III) and continue with the solvothermal methods.

More investigation into manganese is warranted. Perhaps manganese, tricine and phbenz could be reacted together in the hope of synthesising new and exciting species.

4.5 References

- ¹ A. Ferguson, J. McGregor, A. Parkin, M. Murrie; *Dalton. Trans.* **2008**, 731.
- ² L. F. Jones, D. M. Low, M. Helliwell, J. Raftery, D. Collison, G. Aromí, J. Cano, T. Mallah, W. Wernsdorfer, E. K. Brechin, E. J.L. McInnes; *Polyhedron.* **2006**, 25, 325.
- ³ E. K. Brechin; *Chem. Commun.* **2005**, 5141.
- ⁴ A. Ferguson, Ph. D. Thesis, University of Glasgow, *Synthesis and Characterisation of SMMs*, **2007**.
- ⁵ L. Menabue, M. Saladini; *J. Crystal. Spectro. Res.* **1992**, 22, 6, 713.
- ⁶ M. R. Silva, J. A. Paixão, A. M. Beja and L. A. da Veiga; *Acta. Cryst.* **2001**, C57, 9.
- ⁷ X. Fang, Q. Luo, X. Zeng, Y. Sui, X. Li; *Acta. Cryst.* **2005**. E61, 2604.
- ⁸ (a) W. Schmitt, C. E. Anson, W. Wernsdorfer, A. K. Powell; *Chem. Commun.* **2005**, 2098; (b) G. Aromí, E. K. Brechin; *Struct. Bonding*, (Berlin, Ger.), **2006**, 122, 1-67 (c) A. K. Boudalis, B. Donnadiou, V. Nastopoulos, J. M. Clemente-Juan, Al. Mari, Y. Sanakis, J. Tuchagues, S. P. Perlepes; *Angew. Chem. Int. Ed.* **2004**, 43, 2266.
- ⁹ W. Liu, H. H. Thorp; *Inorg. Chem.* **1993**, 32, 4102.
- ¹⁰ Dr S. Piligkos, University of Copenhagen.
- ¹¹ H. Lui, Lin. Xu, G. Gao, F. Li, Y. Yang, Z. Li, Y. Sun; *J. Solid. State. Chem.* **2007**, 180, 1664.
- ¹² Y. Diskin-Posner, I. Goldberg; *New. J. Chem.* **2001**, 25, 899.
- ¹³ A. M. Ako, O. Waldmann, V. Mereacre, F. Klöwer, I. J. Hewitt, C. E. Anson, H. U. Güdel, A. K. Powell; *Inorg. Chem.* **2007**. 46, 3, 756.
- ¹⁴ L. F. Jones, P. Jensen, B. Moubaraki, K. J. Berry, J. F. Boas, J. R. Pilbrow, K. S. Murray; *J. Mater. Chem.* **2006**, 16, 2690.
- ¹⁵ (a) H. Oshio, N. Hoshino, T. Ito, M. Nakano, F. Renz, P. Gütllich; *Angew. Chem. Int. Ed.* **2003**, 42, 223; (b) T. Liu, B. Wang, Y. Chen, Z. Wang, S. Gao; *Z. Anorg. Allg. Chem.* **2008**, 634, 778.
- ¹⁶ R. Shaw, R. H. Laye, L. F. Jones, D. M. Low, C. T. Eeckelaers, Q. Wei, C. J. Milios, S. Teat, M. Helliwell, J. Raftery, M. Evangelisti, M. Affronte, D. Collison, E. K. Brechin, E. J. L. McInnes; *Inorg. Chem.* **2007**, 46, 12, 4968.
- ¹⁷ A. Bino; *J. Am. Chem. Soc.* **1987**, 109, 276.
- ¹⁸ (a) A. A. Smith, R. A. Coxall, A. Harrison, M. Helliwell, S. Parsons, R. E.P. Winpenny; *Polyhedron.* **2004**, 23, 1557; (b) M. Frey, S. G. Harris, J. M. Holmes, D. A. Nation, S. Parsons, P. A. Tasker, R. E. P. Winpenny; *Chem. Eur. J.* **2000**, 6, 8, 1047; (c) S. M. Gorun, G. C. Papaefthymiou, R. B. Frankel, S. J. Lippard; *J. Am. Chem. Soc.* **1987**, 109, 3337.
- ¹⁹ (a) D. J. Price, M. Murrie; *Annu. Rep. Prog. Chem.* **2007**, Sec A, 103, 20-38 (b) C. J. Milios, A. Vinslava, A. G. Whittaker, S. Parsons, W. Wernsdorfer, G. Christou, S. P. Perlepes, E. K. Brechin; *Inorg. Chem.* **2006**, 45, 5272.

5. Synthesis of Chromium complexes: Bis-Tris

The kinetic inertness of Chromium(III) ions has resulted in only a small number of polymetallic complexes when compared to iron and manganese.¹ All known complexes result from solvothermal reactions of simple triangular clusters $[\text{Cr}_3\text{O}(\text{O}_2\text{CR})_6(\text{L})_3]^{n+}$ (where R is a carboxylate and L is a solvent) in superheated alcohol. This approach usually results in the formation of cyclic chromium complexes, ranging in nuclearity from eight to twelve chromium centres,² in which both the carboxylate and solvent (RO⁻) are present as bridging ligands. Another technique is the thermal rearrangement of these triangular units under a stream of N₂ at high temperatures which can produce these cyclic clusters³ as well as cage clusters.⁴ These clusters usually result in an $S = 0$ ground state, the exceptions being a Cr₁₂ centred-pentacapped trigonal prism with $S = 6$,⁵ a ferromagnetic Cr₁₀ wheel with $S = 15$,⁶ and a tetrametallic cluster with $S = 6$.⁷ Simple chromium salts have been investigated in particular with tripodal ligands by Talbot-Eeckelaers *et al.*⁸ This approach involves the use of Cr(II) salts, reacted under reflux conditions and solvothermally, producing three novel clusters which incorporate the ligand into the final complex. Talbot-Eeckelaers *et al* have reacted 1, 1, 1, tris(hydroxymethyl)propane, (H₃tmp) together with CrCl₂ and NaOMe under reflux conditions in MeOH to produce $[\text{Cr}_2(\text{H}_2\text{tmp})_2\text{Cl}_4]$. Solvothermally, they have synthesised two analogous clusters $[\text{Cr}_8\text{O}_2(\text{thme})_2(\text{Hthme})_4\text{Cl}_6]$ and $[\text{Cr}_8\text{O}_2(\text{Hpeol})_2(\text{H}_2\text{peol})_2\text{Cl}_6]$ using the ligands 1, 1, 1, tris(hydroxymethyl)ethane, (H₃thme) and pentaerythritol (H₄peol). All ions present in these complexes are Cr(III) due to oxidation during the reaction process. It is worth noting that analogous reactions using Cr(III) salts did not produce any complexes.⁷ Our work with Cr(III) originally attempted to synthesise an analogous cluster of $[\text{Fe}_{12}\text{O}_4(\text{OH})_2(\text{L}^1)_4(\text{OAc})_6][\text{Cl}]_2$ (section 2.4.1) using edte (H₄L¹, section 1.12), however the use of Cr(III) triangle starting materials resulted in the synthesis of the wheel complex $[\text{Cr}_{10}(\text{OAc})_{10}(\text{OMe})_{20}]$ previously synthesised.⁵ Also we investigated the use of Cr(III) salts together with acetate and the edte ligand in an attempt to stop the synthesis of the Cr₁₀ wheel complex. This approach resulted in no complexes being synthesised. We also focussed on the tripodal ligand Bis-Tris (H₅L⁴), (figure 5.1) and its reaction with simple Cr(III) salts.

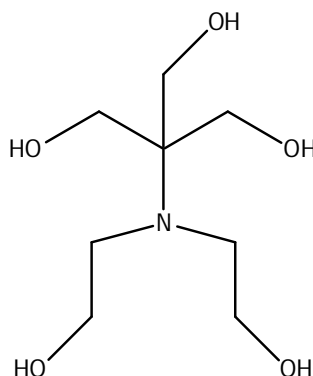


Figure 5.1: bis(2-hydroxyethyl)iminotris(hydroxymethyl)methane, Bis-Tris, H₅L⁴.

Bis-Tris has been well established as not only an excellent bridging ligand, but has been successfully used to synthesise large polymetallic clusters.^{9,10,11} We attempted to react this ligand with Cr(III) ions, in the same way as the other tripodal ligands trying to overcome the inertness of Cr(III) solvothermally in the hope of synthesising new polymetallic species. This approach resulted in the synthesis of two new complexes whose structures and magnetic data are reported below.

5.1 Synthesis of chromium complexes containing Bis-Tris, H₅L⁴

5.1.1 Synthesis of [Cr(H₃L⁴)Cl] (**15**)

To a stirred solution of CrCl₃·6H₂O (0.6 g, 2.4 mmol) in MeOH (10 ml), H₅L⁴ (0.5 g, 2.4 mmol) was added, followed by NaOMe (0.13 g, 2.4 mmol). The solution was stirred for 30 minutes and placed in a sealed Teflon container. The container was placed in an oven and heated to 150°C over 5 minutes. The oven temperature was held at 150°C for 12 h. After 12 h the solution was allowed to cool to room temperature inside the oven. X-ray quality crystals appeared on opening the MeOH solution, in approximately 33% yield. Selected IR data: $\nu = 3269, 2886, 1463, 1306, 1055, 887, 770 \text{ cm}^{-1}$. Crystals analyse as **15** (%) calc. (found) C, 32.72, (32.33); H, 5.49 (5.83); N, 4.77 (4.68).

5.1.2 Synthesis of $[\text{Cr}_4(\text{H}_2\text{L}^4)]\cdot\text{MeOH}$ (**16**·MeOH)

To a stirred solution of $\text{CrCl}_3\cdot 6\text{H}_2\text{O}$ (0.3 g, 1.2 mmol) in MeOH (10 ml), H_5L^4 (0.75 g, 3.6 mmol) was added, followed by NaOMe (0.19 g, 3.6 mmol). The solution was stirred for 30 minutes and placed in a sealed Teflon container. The container was placed in an oven and heated to 150°C over 5 minutes. The oven temperature was held at 150°C for 12 h. After 12h the solution was allowed to cool to room temperature inside the oven. The solution was filtered and stored in a sealed sample vial. X-ray quality crystals appeared in the sealed solution after two months in approximately 11% yield. Selected IR data: $\nu = 3279, 2852, 1064, 1004, 749, 678, 627\text{ cm}^{-1}$. Crystals analyse as **16** (%) calc. (found) C, 37.36, (37.69); H, 6.08 (6.40); N, 5.28 (4.89).

5.2 Complexes containing Bis-Tris

5.2.1 Discussion of crystal structure of $[\text{Cr}(\text{H}_3\text{L}^4)\text{Cl}]$ (**15**)

Complex **15** is a monomeric Cr(III) complex which crystallises in the orthorhombic space group $Pnma$ (figure 5.2 where the atom suffix, a, signifies symmetry equivalent atoms).

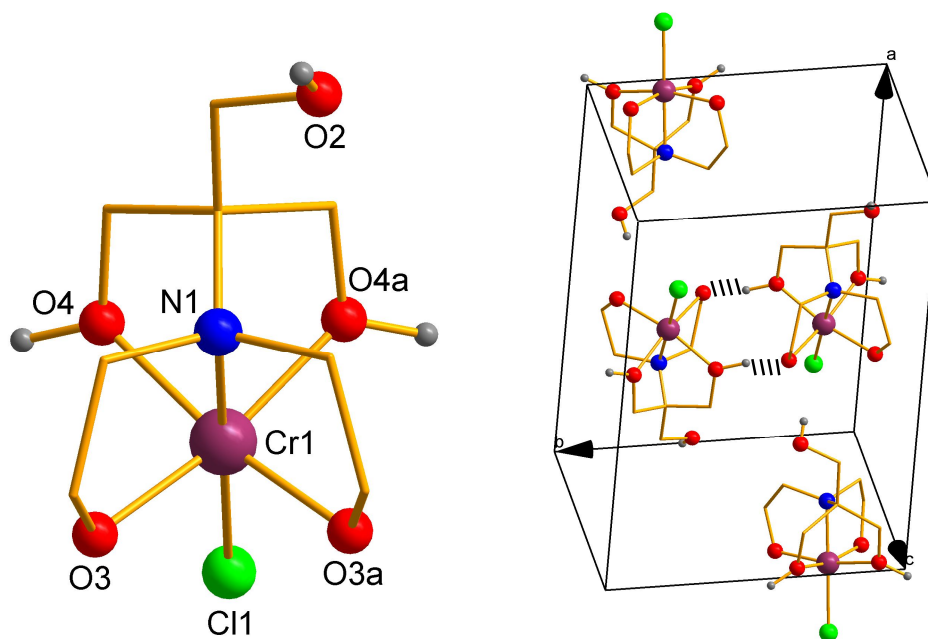


Figure 5.2: Left, structure of **15**. Right, the crystal packing of **15** displaying the hydrogen bonding in the cell between adjacent molecules(O3...O4a, 2.440Å).

The ligand binds in an {NO₄} donor set previously seen for monomeric species of Co(II), Cu(II) and Ni(II),¹² however Bis-Tris is present as a neutral ligand (H₅L⁴) for these monomers and not (H₃L⁴) found in **15**. This binding mode is similar, but different to that seen for the complex [NaFe₁₀O₃(OH)₄(HL⁴)₂(piv)₁₃] (Fe₁₀)⁹ For this complex the level of deprotonation is different and the ligand acts as a linker for smaller clusters maintaining the {NO₄} donor set. The two CH₂CH₂O⁻ arms, (O3 and O3a) are deprotonated and bind monodentate to the Cr(III) centre. Two of the tripodal CH₂OH arms bind monodentate to the Cr(III) centre. The final arm, (O2) is protonated, unbound and lies on a symmetry plane resulting in the arm (O2) being located over two sites in the crystal structure. Although this monomeric species is not of interest magnetically, it is the first example of a Cr(III) complex with this ligand.

Table 5.1 Data for the crystal structure determination of **15**

Empirical formula	C ₈ H ₁₇ N ₁ O ₅ Cr ₁
fw(gmol ⁻¹)	1060.88
Spacegroup	<i>Pnma</i>
a(Å)	14.672(6)
b(Å)	9.751(4)
c(Å)	7.592(3)
V(Å ³)	1086.37(8)
Z	1
T(K)	100(2)
λ(Å)	0.71073
ρ _{calcd} (Mg/m ³)	1.802
μ(mm ⁻¹)	1.304
R ₁ (%)	3.04
wR ₂ (%)	9.49
Goodness of fit indicator	0.735

[†]Estimated standard deviations in the least significant figure are given in parentheses.

$${}^aR_1 = \sum ||F_o| - |F_c|| / \sum |F_o|$$

$${}^bWR_2 = [\sum[w(F_o^2 - F_c^2)_2] / \sum[w(F_o^2)_2]]^{1/2}$$

$$\text{where } w = 1/[\sigma^2(F_o^2) + (0.2P)^2] \text{ and } P = [F_o^2 + 2F_c^2]/3$$

Table 5.2 Selected bond distance for **15**

Bonds	Distance (Å) †
Cr1—N1	2.041(3)
Cr1—O3	1.968(17)
Cr1—O4	1.990(17)
Cr1—Cl1	2.316(11)

† Estimated standard deviations in the least significant figure are given in parentheses.

5.2.2 Discussion of crystal structure of $[\text{Cr}_4(\text{H}_3\text{L}^4)_4] \cdot \text{MeOH}$ (**16**·MeOH)

Complex **16** is a Cr(III) tetramer complex which crystallises in the tetragonal space group $I4_1/a$ (figure 5.3).

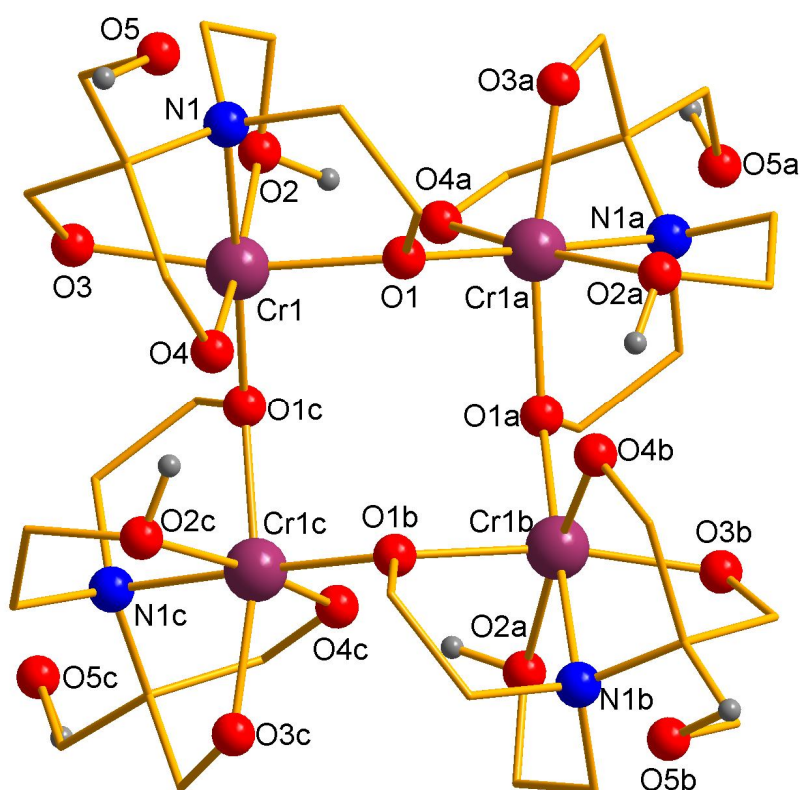


Figure 5.3: Structure of **16**(ball and stick representation with Cr(III) purple; O, red; N, blue; C, brown; H atoms are omitted for clarity)[atom suffix a signifies the symmetry equivalent atom: $a = 1 - x, 1 - y, 1 - z$, b signifies the symmetry equivalent atom: $b = 1 - x, 1 - y, 1 - z$, c signifies the symmetry equivalent atom: $c = 1 - x, 1 - y, 1 - z$].

There are two main differences associated with the ligand for complexes **15** and **16**. The first difference is the deprotonation of the ligand for **16**. The increase of NaOMe has resulted in two of the tripodal arms being deprotonated along with one $\text{CH}_2\text{CH}_2\text{O}^-$ arm (figure 5.4). This de-protonation is entirely different to that seen for the monomeric complexes⁸ and Fe_{10} .⁹ The de-protonation of Bis-Tris in **16** has been seen for one other cluster $[\text{Co}_4\text{Na}_2(\text{HL})_2(\text{H}_2\text{L})_2(\text{MeOH})_4]$, (Co_4), however the ligand displays different binding, the $\text{CH}_2\text{CH}_2\text{OH}$ arms remains protonated and unbound.¹¹ The second difference is that Bis-Tris displays a different binding mode to that seen for the previous monomer, O3 and O4 are monodentate bonding to Cr1 with the remaining arm O5 being protonated, unbound hydrogen bonded to lattice solvent. O2 remains protonated and binds monodentate however the final arm, O1, is

bidentate, bridging neighbouring Cr(III) centres forming the square like core. The bidentate binding of O1, results in a non-planar Cr₄ core (figure 5.4).

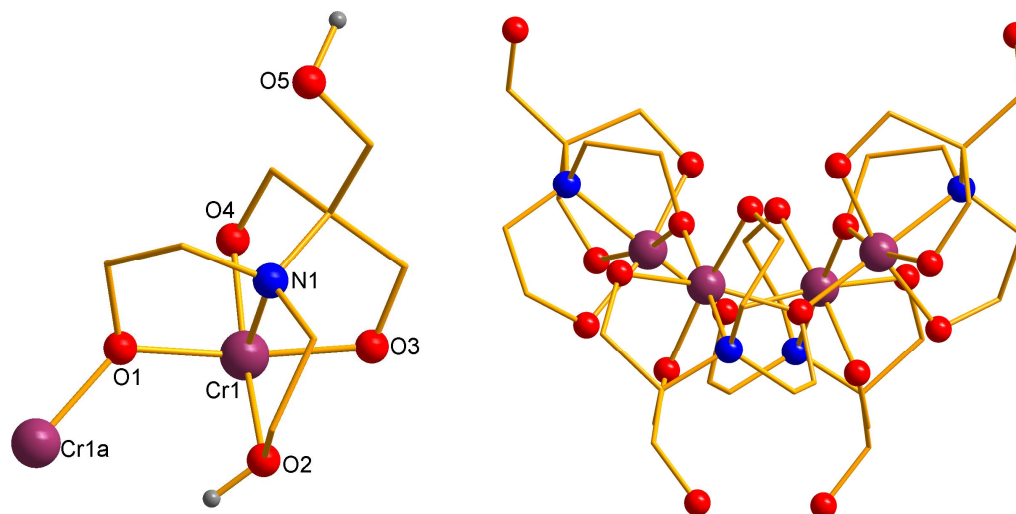


Figure 5.4: left, ligand binding found in **16** showing de-protonated arms
Right, alternate view showing the non-planar core of **16**

This type of core is unprecedented in chromium chemistry. Only a family of three tetranuclear manganese complexes are known with this type of core. They display ferromagnetic intramolecular exchange coupling and crystallise in the tetragonal space group *I*-4.¹³

Table 5.3 Data for the crystal structure determination of **16**

Empirical formula	C ₃₃ H ₆₄ N ₄ O ₂₁ Cr ₄
fw(gmol ⁻¹)	3693.75
Spacegroup	I4 ₁ /a
a(Å)	24.902(11)
c(Å)	8.479(10)
V(Å ³)	5258(7)
Z	1
T(K)	100(2)
λ(Å)	0.71073
ρ _{calcd} (Mg/m ³)	1.467
μ(mm ⁻¹)	0.880
R ₁ (%)	6.63
wR ₂ (%)	12.36
Goodness of fit indicator	0.952

[†]Estimated standard deviations in the least significant figure are given in parentheses.

$${}^a R_1 = \frac{\sum ||F_o| - |F_c||}{\sum |F_o|}$$

$${}^b wR_2 = \left[\frac{\sum [w(F_o^2 - F_c^2)]}{\sum [w(F_o^2)]} \right]^{1/2}$$

$$\text{where } w = 1/[\sigma^2(F_o^2) + (0.2P)^2] \text{ and } P = [F_o^2 + 2F_c^2]/3$$

Table 5.4 Selected bond distance for **16**

Bonds [†]	Distance (Å) [†]
Cr1—N1	2.045(8)
Cr1—O1	1.980(7)
Cr1—O2	2.033(7)
Cr1—O3	1.942(7)
Cr1—O4	1.970(7)
Cr1a—O1	1.949(6)

[†] Estimated standard deviations in the least significant figure are given in parentheses.

Table 5.5 Selected bond angles for **16**

Atoms	Angle ($^{\circ}$) [†]
Cr1–O1–Cr1a	129.56(3)

[†] Estimated standard deviations in the least significant figure are given in parentheses.

5.2.2.1 Magnetic Susceptibility Measurements for **16**

Magnetic susceptibility measurements were carried out on an air-dried sample. For **16** the value of χT at 300K is $5.87 \text{ cm}^3 \text{ mol}^{-1} \text{ K}$, lower than expected for four uncoupled Cr(III) ions ($7.5 \text{ cm}^3 \text{ mol}^{-1} \text{ K}$ for $g=2$), indicating strong antiferromagnetic interactions between the Cr(III) centres (figure 5.5).

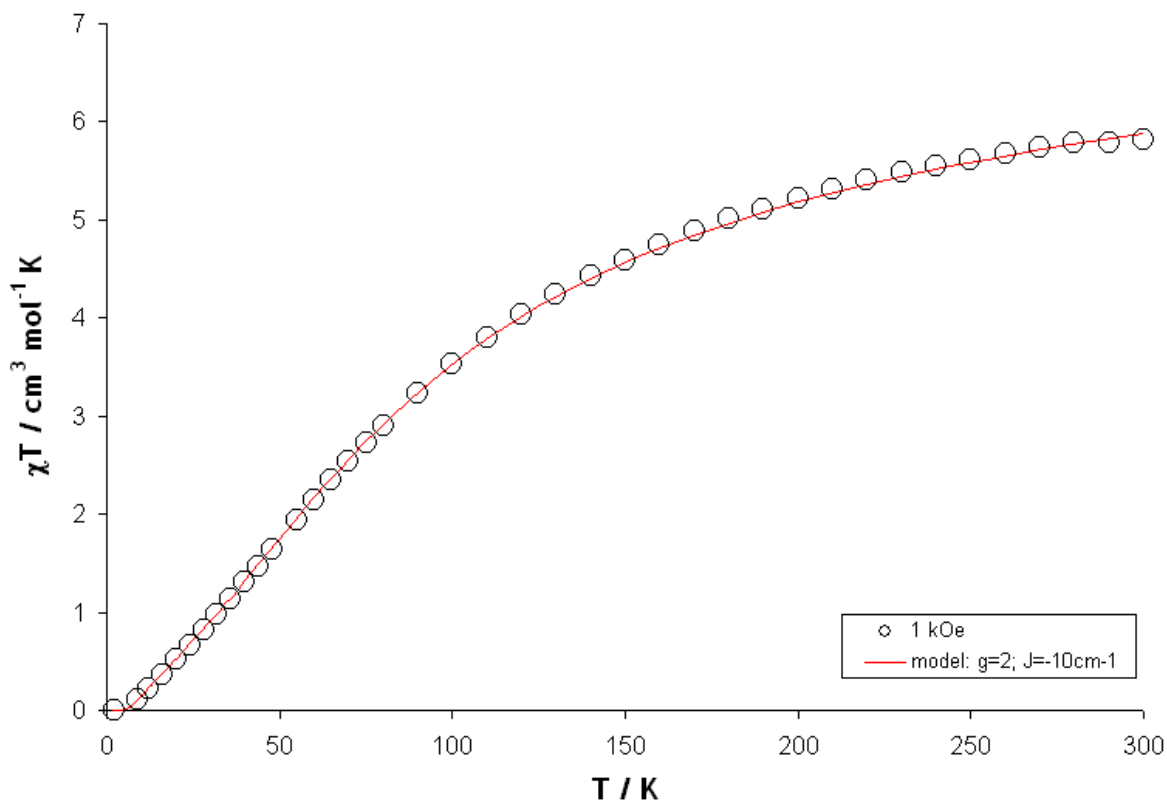
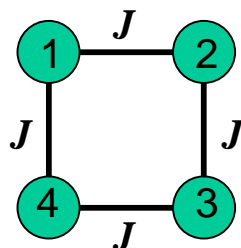


Figure 5.5: Temperature dependence of χT for **16** from 300-1.8 K measured in a field of 1 kOe. Red line indicates model of χT data vs T

χT decreases steadily to a value of $0.004 \text{ cm}^3 \text{ mol}^{-1} \text{ K}$ at 1.8K. The χT data was modelled using MAGPACK down to 1.8 K using a $1J$ model (figure 5.6).¹⁴ $S = 0$, with $g = 2$, $J = -10 \text{ cm}^{-1}$.



$$\hat{H} = -2J(\hat{S}_1\hat{S}_2 + \hat{S}_2\hat{S}_3 + \hat{S}_3\hat{S}_4 + \hat{S}_1\hat{S}_4)$$

Figure 5.6: Representation of $1J$ model for **16**

The temperature dependence of χ is shown in Figure 5.7. The fact that the susceptibility goes through a broad maximum at ca. 70 K is a clear indication of antiferromagnetic exchange interactions within the cluster.¹⁵ The rapid increase of χ below 4 K can be accounted for by the presence of a small amount of a monomeric impurity.

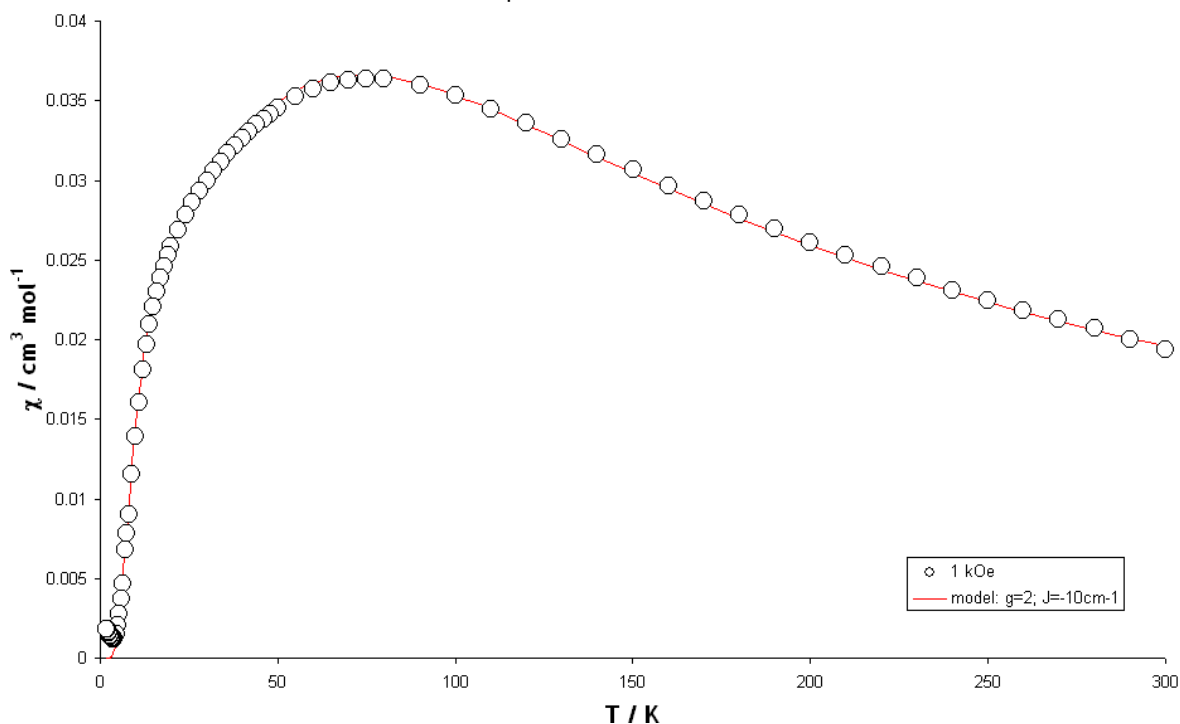


Figure 5.7: Temperature dependence of χ vs T Red line indicates the model.

5.3 Conclusions

Bis-Tris has already been established as an excellent bridging ligand in the synthesis of polynuclear iron complexes. However here we have reported the synthesis of the first two Cr(III) Bis-Tris complexes, both from solvothermal synthesis. An increase in the ratio metal ion:ligand:base from 1:1:1 to 1:3:3 results in the synthesis of the tetramer complex **16**, however antiferromagnetic interactions dominate resulting in an $S = 0$ ground state for the cluster. The Bis-Tris ligand displays a new binding in **16** compared to any previous known clusters.^{9,10}

5.4 Future work

We have seen some success in the use of solvothermal techniques into the synthesis of Cr(III) complexes using Bis-Tris. Therefore there is still the potential to synthesise new polynuclear complexes using Bis-Tris. Alternative synthesis could be the use of Cr(II) starting materials which oxidise to Cr(III): this could provide

alternative products to the two discovered using Bis-Tris and Cr(III). Another process could be the aforementioned microwave synthesis, which should overcome the inertness of Cr(III) as well as providing another synthetic route to new clusters.

5.5 References

- ¹ G. Aromi, E. K. Brechin; *Struct. Bonding*, (Berlin, Ger.), **2006**, 122, 1.
- ² R. H. Laye, E. J. L. McInnes; *Eur. J. Inorg. Chem*, **2004**, 2811.
- ³ I. M. Atkinson, C. Benelli, M. Murrie, S. Parsons, R. E. P. Winpenny; *Chem. Commun.* **1999**, 285.
- ⁴ S. Parsons, A. A. Smith, R. E. P. Winpenny; *Chem. Commun.* **2000**, 579.
- ⁵ F. E. Mabbs, E. J. L. McInnes, M. Murrie, S. Parsons, C. C. Wilson, R. E. P. Winpenny; *Chem. Commun.* **1999**, 643.
- ⁶ E. J. L. McInnes, C. Anson, A. K. Powell, A. J. Thomson, S. Poussereau, R. Sessoli; *Chem. Commun.* **2001**, 89.
- ⁷ A. Bino, D. C. Johnston, D. P. Goshorn, T. R. Halbert, E. I. Stiefel; *Science*. **1988**, 241, 1479.
- ⁸ C. E. Talbot-Eeckelaers, G. Rajaraman, J. Cano, G. Aromí, E. Ruiz, E. K. Brechin; *Eur. J. Inorg. Chem.* **2006**, 3382.
- ⁹ A. Ferguson, J. McGregor, A. Parkin, M. Murrie; *Dalton Trans.* **2008**, 731.
- ¹⁰ A. Ferguson, A. Parkin, M. Murrie; *Dalton Trans.* **2006**, 3627.
- ¹¹ A. Ferguson, Ph. D. Thesis, University of Glasgow, *Synthesis and Characterisation of SMMs*, **2007**.
- ¹² Y. Inomata, Y. Gochou, M. Nogami, F. S. Howell, T. Takeuchi; *J. Mol. Str.* **2004**, 702, 61.
- ¹³ C. Boskovic, R. Bircher, P. L. W. Tregenna-Piggott, H. U. Güdel, C. Paulsen, W. Wernsdorfer, A. L. B, E. Khatsko, A. Neels, H. Stoeckli-Evans; *J. Am. Chem. Soc.* **2003**, 125, 14046.
- ¹⁴ J. J. Borrás-Almenar, J. M. Clemente-Juan, E. Coronado, B. S. Tsukerblat; *J. Comp. Chem*, **2001**, 22, 9, 985.
- ¹⁵ A. K. Powell, S. L. Heath, D. Gatteschi, L. Pardi, R. Sessoli, G. Spina, F. Del Giallo, F. Pieralli; *J. Am. Chem. Soc.* **1995**, 117, 2491.

6.0 Conclusions

6.1 edte (H_4L^1)

The use of the ligand edte, has allowed us to isolate five new complexes. The ligand displays different binding modes and is present in the tetra-deprotonated, tri-deprotonated and doubly-deprotonated forms. These different levels of deprotonation have resulted in new clusters with nuclearity range from two metal centres (complex **5**), to the largest cluster containing twelve metal centres (complex **1**). The ligand binding modes are shown below (figure 6.1).

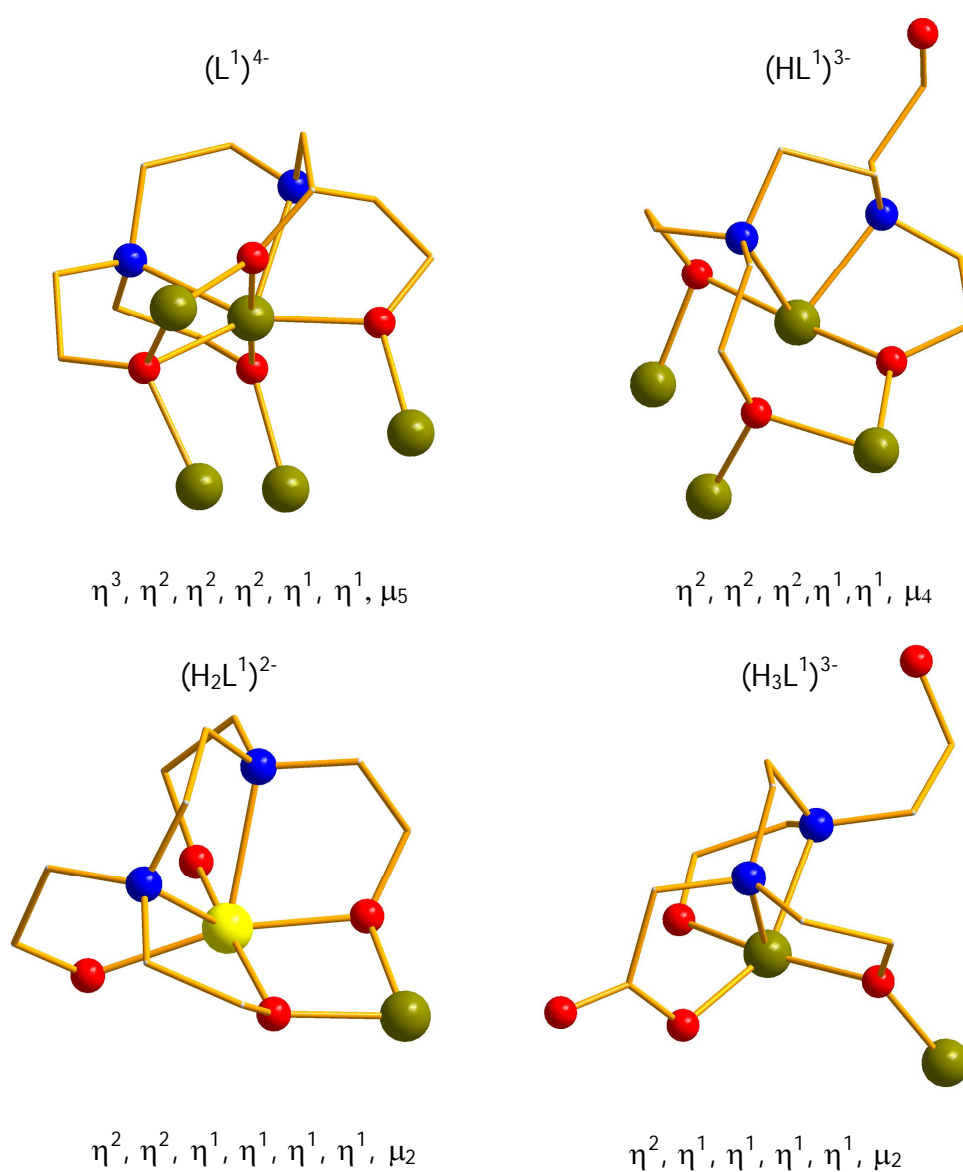


Figure 6.1: different binding modes observed for edte (ball and stick representation with Fe(III), Gold; Fe(II), Yellow; O, Red; N, Blue; C, Brown; H atoms are omitted)

The range of bridging modes observed and the different structures highlights the versatility of the ligand. This ligand has already been investigated in manganese chemistry by Christou *et al*, resulting in other interesting clusters. Therefore the use of different metal centres could lead to new clusters and potentially SMMs.

6.2 bicine (H_3L^2)

Six complexes have been synthesised using bicine, however of these only four incorporate the ligand into the final structure. The ligand is present in three different binding modes in triply and doubly deprotonated forms. One cluster (complex **9**) incorporates all three ligand binding modes (figure 6.2).

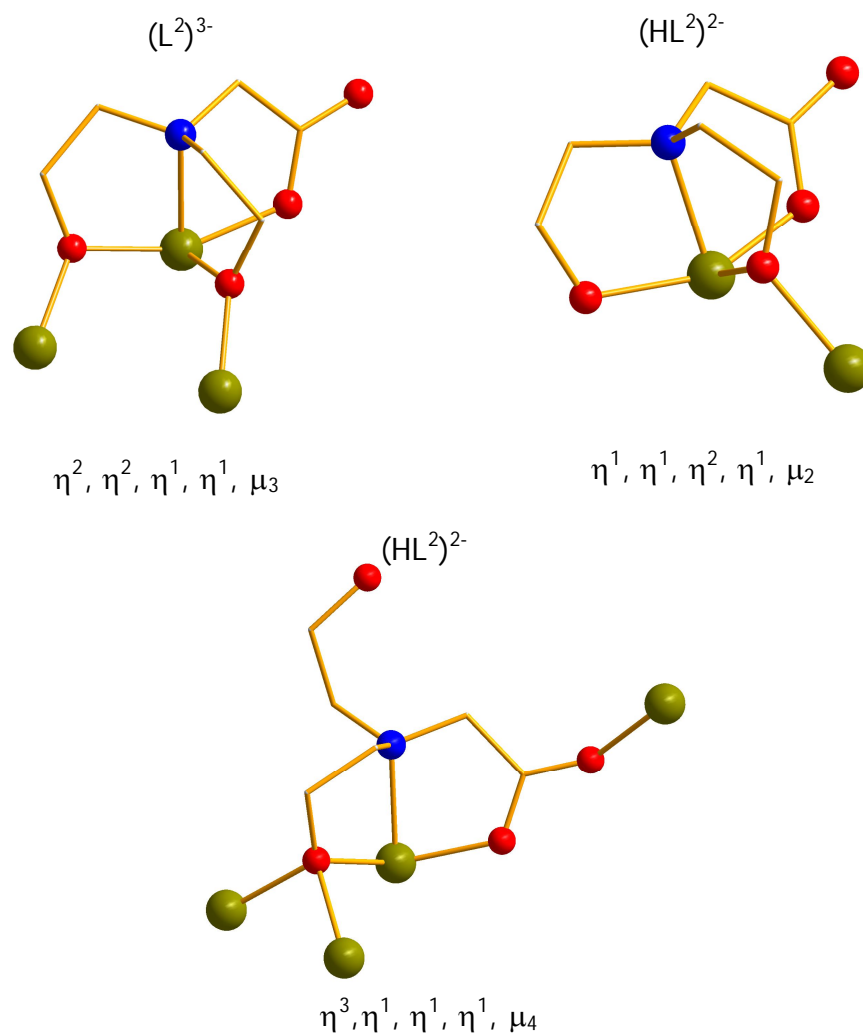


Figure 6.2: different binding modes observed for bicine (ball and stick representation with Fe(III), Gold; O, Red; N, Blue; C, Brown; H atoms are omitted)

Although only four complexes were synthesised, a further two complexes with carboxylate ligands were synthesised from reactions containing bicine. This ligand has illustrated its flexibility with full deprotonation and coordination in the synthesis of Fe(III) complexes. This ligand is still relatively unexplored with other metal centres, therefore further research into this ligand with different metal centres should lead to new clusters.

6.3 Tricine (H_4L^3)

Tricine has not been as successful as edte or bicine in the synthesis of new polymetallic iron complexes resulting in only three new clusters. Only two of these contain the ligand. The ligand is present in the doubly and triply deprotonated forms and displays three different binding modes (figure 6.3).

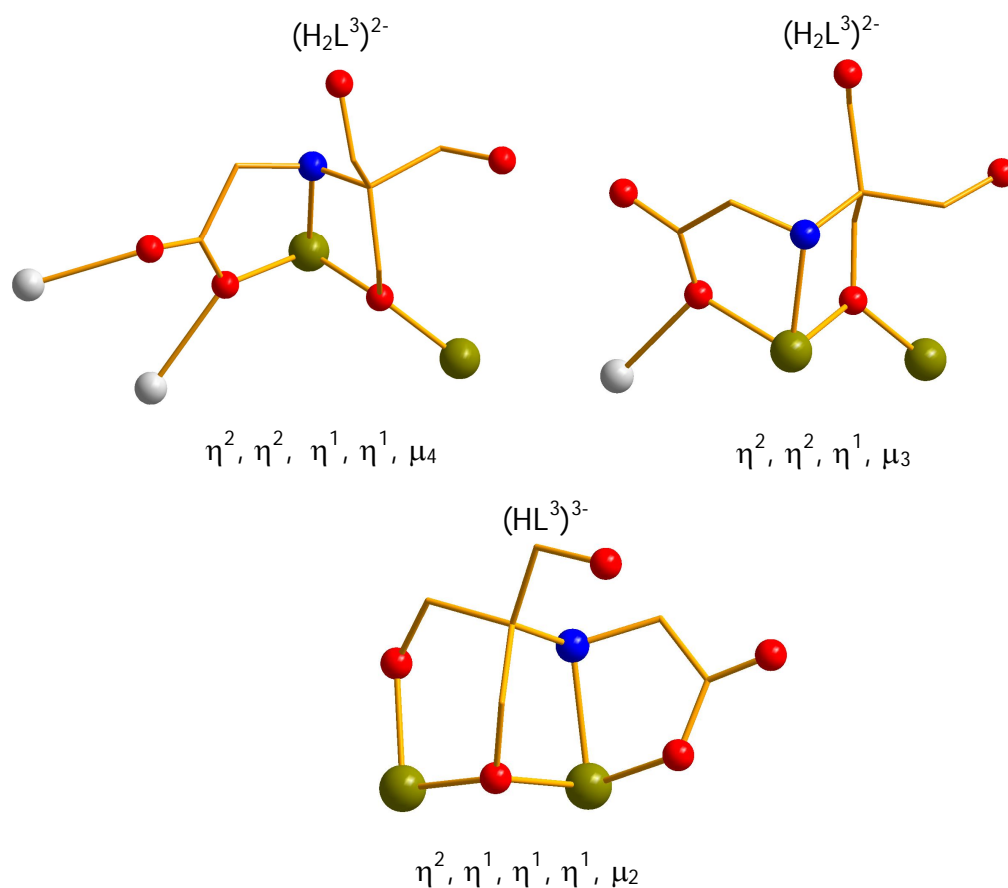


Figure 6.3: different binding modes observed for tricine (ball and stick representation with Fe(III), Gold; O, Red; N, Blue; C, Brown; Na, White; H atoms are omitted)

The ligand has demonstrated its ability to bridge more than one metal centre forming large clusters, however only two iron clusters were synthesised containing this ligand. Further research into reactions with this ligand and other transition

metal centres should lead to more examples of paramagnetic clusters and greater understanding of the ligand.

6.4 Bis-Tris (H_5L^4)

Research into the ligand Bis-Tris with Cr(III) has produced two new complexes. The ligand is present in two different binding modes in doubly and triply deprotonated forms (figure 6.4).

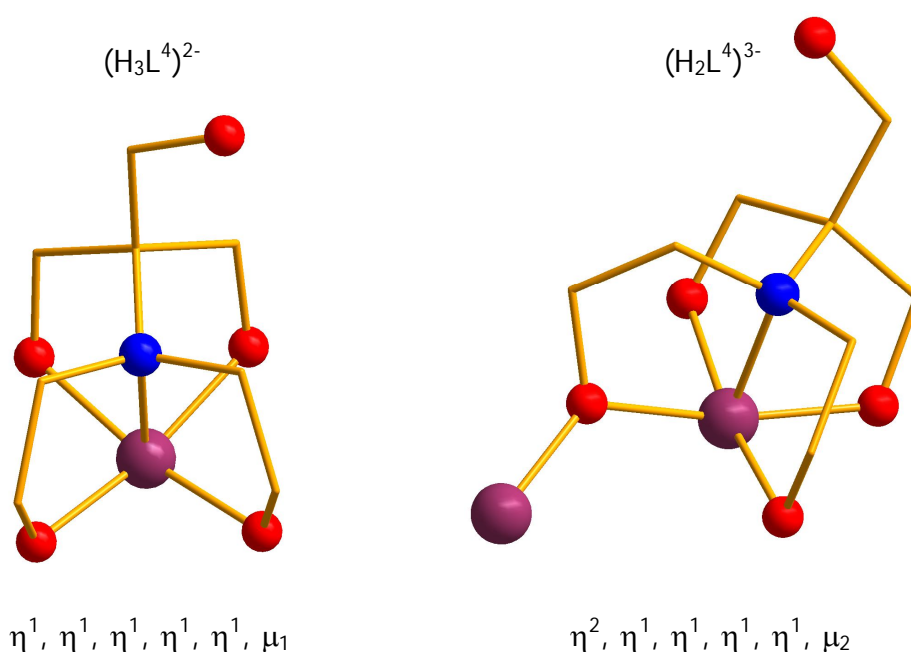


Figure 6.4: different binding modes observed for Tricine (ball and stick representation with Cr(III), Purple; O, Red; N, Blue; C, Brown; H atoms are omitted)

The work with Cr(III) and Bis-Tris is relatively new. We have seen how altering the reaction conditions can have an effect on the complex produced, the binding and deprotonation of the ligand. Therefore further investigation into reactions should allow for more new clusters to be produced not only for Cr(III) but other metal ions with the exception of Fe(III) which has been previously studied by Ferguson *et al.*